Università degli Studi di Udine

DIPARTIMENTO DI SCIENZE MATEMATICHE, INFORMATICHE E FISICHE
Corso di dottorato in Informatica e Scienze Matematiche e Fisiche

Tesi di dottorato

MAGIC telescopes observations at Very Large Zenith angles and the first neutrino-gamma association

Candidato:
Michele Peresano
Matricola 126619

Relatore:
Prof. Barbara De Lotto

Correlatore:
Dr. Ievgen Vovk

Anno Accademico 2017–2018

ABSTRACT

This PhD thesis summarises research activities I carried out as a member of the MAGIC collaboration (https://magic.mpp.mpg.de). My work belongs to the field of cosmic rays, for which lack of knowledge about their origin and nature of their energy spectrum represents one of the major open problems in modern astrophysics. This research deals with both galactic and extragalactic sources.

The thesis opens with an introduction to cosmic rays, and on the importance of using neutrally charged messengers like photons and neutrinos to probe the presence of cosmic rays at the sites of cosmic acceleration. It continues by describing the general structure and performance of the MAGIC telescopes, in particular the subsystems and data analysis steps relevant to the subjects reported in this thesis. It then explains the importance of a novel observational technique pioneered by MAGIC, which constitutes one of the two original activities on which I have contributed. The research conducted on this subject consists in laying down the development and optimisation of the data analysis techniques in order to allow the MAGIC telescopes to operate at Very Large Zenith Angle (VLZA) observations - i.e. towards the horizon. This will possibly allow the first detection of Very High Energies (VHE) sources by an experiment such as MAGIC, not only in the multi TeV (TeV = tera electron Volts $= 10^{12} eV$) range but also at higher energies, up to $\sim 100 TeV$ where the nature of the observed emission can give insights on the possibility of cosmic ray acceleration *in - situ*.

The second part of the thesis describes a major scientific breakthrough for MAGIC and for the whole astrophysical community. In 2017 an alert from the IceCube experiment triggered a response from MAGIC as well as a number of different satellites and ground observatories worldwide. For the first time a VHE photon coincident with a VHE neutrino has been detected. This caused the entire community to focus on a source that was later identified as a *blazar* (an Active Galactic Nucleus whose relativistic jet points at the observer). The fourth chapter illustrates my contribution to the MAGIC data analysis which led to the VHE γ-ray detection of the neutrino source.

The conclusions emphasise the importance of investigations from the point of view of current cosmic ray physics and future research in the field.

ACKNOWLEDGEMENTS

I wish to express my gratitude to my advisor Prof. Barbara De Lotto, for the support received during my PhD. I thank her for her patience and professionality. Her guidance helped me during my research and in writing this thesis.

Besides my advisor, I had the luck to receive extremely precious help and insights by many other people. Dr. Ievgen Vovk has been to me an invaluable scientific mentor, before anything else. Thanks to his patience and scientific solidity, I learned invaluable lessons that I will make sure to apply in the future - whatever it will be. I carried out the core of the work on VLZA while guest of the Max Planck Institute for Physics, under the lead of Dr. Razmik Mirzoyan, whom I thank for the support, together with the MAGIC collegues working there.

I express my gratitude to Prof. Elisa Bernardini and Dr. Konstancja Satalecka for their constant support and advice throughout the work on the neutrino-blazar source. It has been a long work, dense of new knowledge and opportunities. I didn't do it alone, but with the collaboration and friendship of Dr. Luca Foffano, whith whom I share this achievement.

I wish to thank the thesis referees, Prof. Andrea Chiavassa and Dr. Riccardo Rando, for their insightful comments and questions, which incented me to improve my writing, better express my ideas and thinking more deeply about what I thought was simple. This thesis could see the light thanks to a great number of people which makes the MAGIC collaboration possible. I learned very much from all of them.

The person who supported me most, loved me enough to do it for a longer time than a PhD. Agnese Codutti has been my partner during all these years and I wish to thank her in a much simpler, but heartfelted way: thank you for being always besides me, regardless the distance. My entire family has been of continuous support, while never constraining me to pre-defined choices and suggesting me only and always what was the best for me; thank you for your trust and love.

Even as an unofficial figure during my PhD, Dr. Massimo Persic has been an irreplaceable collegue and friend. His experience and ideas have shaped my mindset about science and life. Last but not least, I thank Drs. Anna Driutti, Michele Palatiello, Barbara Biasuzzi and Carlo Stella, of which I have been and I will always feel like the less experienced one: I learned useful lessons from you since the first day I got my foot in the door.

All these years of study and work made me meet many people, in many places. What I think I knew changed constantly in light of what I learned. This is the main reason why I want to continue doing science as much as possible.

I apologise if your name didn't appear in this particular circumstance. Please know that your contribution is in my heart.

CONTENTS

ACRONYMS

AGN	Active Galactic Nuclei
ATEL	The Astronomer's Telegram
CRs	Cosmic Rays
CTA	Cherenkov Telescope Array
DC	Direct Current
FOV	Field of View
GCN	Gamma-ray Coordinates Network
HE	High Energy
IACT	Imaging Cherenkov Atmospheric Technique
IPRC	Individual Pixel Rate Control
LAT	Large Area Telescope
LOS	Line of Sight
MAGIC	Major Atmospheric Gamma Imaging Cherenkov
MC	Monte Carlo
NSB	Night Sky Background
PHE	photoelectrons
PWNe	Pulsar Wind Nebulae
RF	Random Forest
SNR	Supernova Remnant
UHECRs	Ultra High Energy Cosmic Rays
VHE	Very High Energy
VLZA	Very Large Zenith Angle
ZA	Zenith Angle(s)

LIST OF TABLES

LIST OF FIGURES

1 INTRODUCTION

1.1 ON THE ORIGIN AND NATURE OF COSMIC RAYS

At the very beginning of the 20th century, soon after the early developments of the newborn framework of quantum mechanics, a continuous evolution in theoretical and experimental techniques triggered the start of what we now call modern particle physics.

Already during the final years of the 19th century, physicists were focusing on the description of the phenomenon of radioactivity on the basis of the known theories of the time. The basic terminology currently used in the field of CRs and particle physics started to be used around that period.

Each of the fundamental concepts about the nature and type of the different components of radiation acquired a meaning in terms of both classical electrodynamics and of the early concepts of nuclear physics (like the discoveries of α, β and γ radiation types), which got boosted by the developments of the quantum theory of radiation. It is not surprising that all these early achievements were carried out by means of experimental setups on Earth. The main sources of radioactivity known at the time were in fact found mainly in mixed compositions of minerals in the soil. This fact was fundamental to explaining strange phenomena related to experimental setups in which the only effects known to happen were those related to electrodynamics. For example, at the beginning of the 20th century electroscopes were observed to get continually discharged by ionising radiation even when taking into account possible impurities within or from the material making up the instrumentation. This prompted the scientific community to consider that the reasons were possibly to be found in the newly discovered phenomena of natural radiation from the Earth itself [1].

In the early decades of the 20th century, combined studies by Victor Hess [2] and Domenico Pacini [3] clearly proved that assumption to be wrong. Evidence was showing that the mysterious and ever present ionising radiation was in fact coming not from below, but from above the Earth [1].

That marked the beginning of the field of cosmic ray physics. From then on, multiple progressive measurements helped to undercover the nature and composition of radiation at various altitudes in the atmosphere.

Questions relevant to CRs are appreciating how many particle species contribute to them, what is the family - or families - of their celestial objects sources, and how all this relates to their energy spectrum.

It is evident that answering these questions is challenging first of all from the point of view of measurements. A summary picture with the broad energy distribution of CRs is shown in Fig.1.

The energy distribution of CRs covers many decades, overcoming by up to ~ 5 orders of magnitude the energies achieved with particle accelerators on Earth.

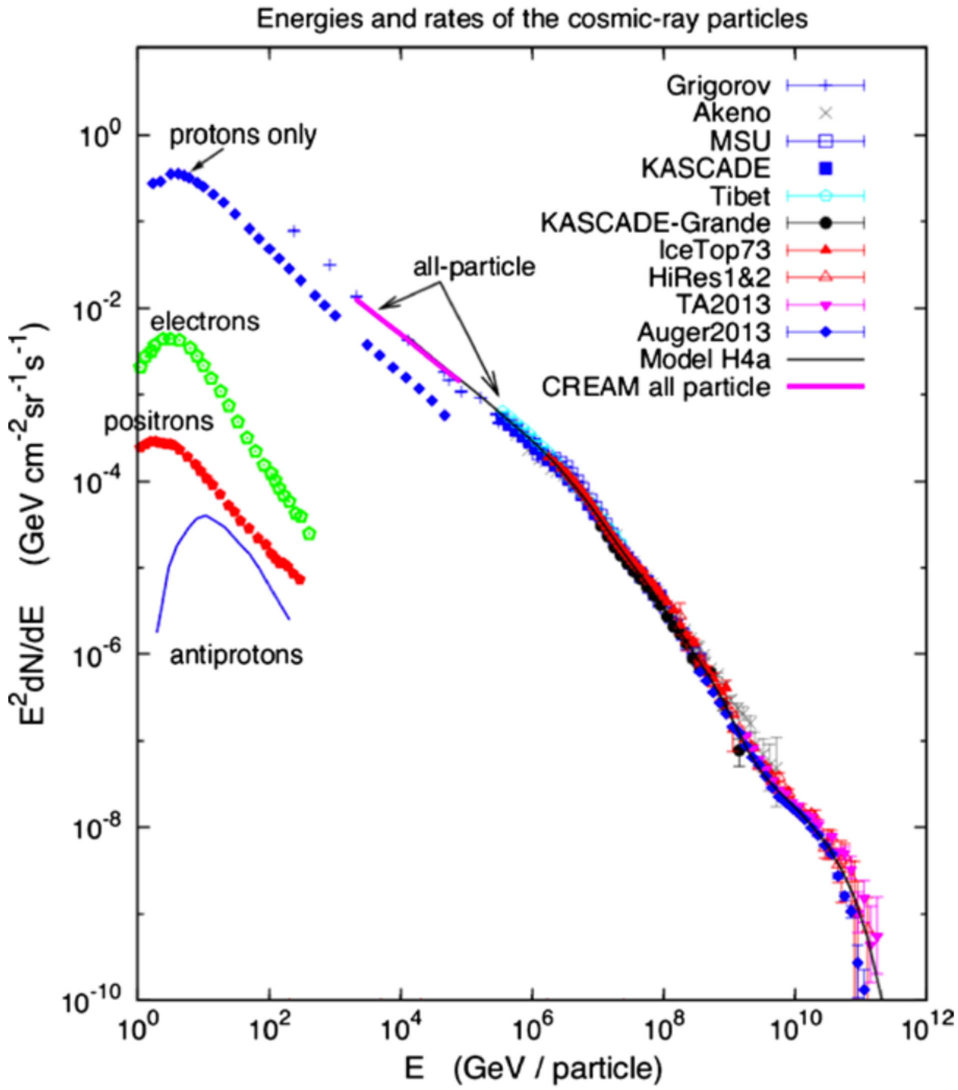

Figure 1: Spectrum of the CRs reaching the Earth adapted from [4]. Both the all-particle spectrum and that of the main subatomic compositions are reported.

Historically, the first component to be understood has been at the Solar System scale, namely the Solar radiation. Given the historical wealth of this data - much easier to measure than at higher energies - this represented a first empirical distinction over the origin of different cosmic particles.

In fact, the Solar activity represents the main discriminant at the low-energy end of the spectrum as it can be seen by the first decade in energy shown in Fig.1. The particles which get generated from the Solar environment, propagate through our planetary system in coincidence with events such as flares and coronal mass ejections [5].

Still, the behaviour shown after few tens of GeV cannot be explained by just Solar activity. In fact, the most common origin of cosmic particles is situated outside our Solar System, with the majority of them having a Galactic origin. The hunt for higher and higher energy cosmic radiation is especially important when considering Galactic sources.

The interaction between Solar-emitted plasma in the outskirts of the Solar system and the cosmic-ray flux results in an anti-correlation between the latter and solar activity events [4]. The screening effect of solar particles over the rest of the CRs can be seen in the first decade of the spectrum in Fig.1.

Excluding the Solar system energetic particles, the term *cosmic rays* usually refers to particles which originate from within - and possibly confined in - our Galaxy. One of the main hypotheses considered by the community is that the main sources of Galactic CRs are Supernova Remnant (SNR)s [4]. Even though this scenario has became the standard of the research in cosmic ray physics, recent ideas in the field propose that the problem could be more complex than this [6]. One of the main alternatives rising over the standard model of galactic CRs are young Pulsar Wind Nebulae (PWNe) [7]. In this sense both approaches agree in proposing that, if SNRs and/or PWNe are indeed Galactic Pevatrons, they must have been able to accelerate hadrons efficiently enough to explain the *knee* feature of the cosmic ray spectrum ($\sim 10^{15}$eV) in at least a short period of their lifetime. Nonetheless, recent results from the HESS collaboration show that these objects are not the only players in explaining the 10^{15}eV energy budget in our Galaxy [8].

Independently of the particular class of objects, a difficulty in investigating Galactic cosmic ray theories relies on the fact that, even though it's easier to recognise hadronic acceleration at the highest energies, this becomes challenging when looking at lower energies ($\gtrsim$ hundreds of GeV).

At very high energies (Very High Energy (VHE)) the contributions from leptonic channels appear to dominate those coming from hadronic ones, mainly the pion photoproduction arising when protons accelerated by the cosmic ray source collide with ambient protons belonging to the surrounding material ([4], [9]).

A first original part of this work deals with the application of novel experimental techniques in VHE γ-ray physics in the framework of Galactic Pevatrons. A critical achievement for the future of Galactic cosmic ray research would be at least to reach the sub-PeV regime, at which the hadronic contribution to the spectrum of Galactic objects could be highlighted.

The MAGIC collaboration has recently participated in the hunt for the so-called Galactic Pevatrons, suggesting that the SNR Cas A does not belong to this class of objects [10].

Still, the cosmic ray spectrum is much broader than just the knee: other features are the *ankle* at $\sim 10^{18}$eV and the *GZK cutoff* at 10^{20}eV [11]. The nature of CRs is in fact investigated further by examining the energy and composition of the cosmic-ray spectrum at energies up to the GZK cutoff.

Given their atomic masses and energies, the gyroradii (or Larmor radii) of such particles are too large with respect to the thickness of our Galaxy when computed using magnetic field strengths typical of Galactic environments (a few μG) [12]. This clearly points to an extragalactic origin. Recent developments in extragalactic cosmic-ray research aim to understand if these highest energy particles registered by experiments such as Pierre Auger [13] have a well-defined origin. In fact, some of these deflected particles can reach energies up to 10^{20}eV [11].

As statistics increase, different studies investigated if there is indeed a spatial and temporal correlation between Ultra High Energy Cosmic Rays (UHECRs) with Active Galactic Nuclei (AGN), which are still considered among the most probable extragalactic sources of CRs, resulting in a missing link. Recently the Pierre Auger collaboration has shared their results on its constant search for possible anisotropies and it seems that there is indeed evidence for anisotropy in the arrival directions of UHECRs [14].

CRs are mostly protons (~90%) and alpha particles (~9%), and heavier nuclei [12], so they mostly represent charged particles. This causes them to be influenced by any - and most of the time complex - magnetic field configurations, both at the galactic and extragalactic scale. Recent developments in cosmic ray propagation within galactic structures like the Milky Way show that the deflection of UHECRs with charge Z and energy E should be $\lesssim 10^\circ Z(40 \text{ EeV } E^{-1})$ (see [15] and references therein). In general, magnetic field effects on CRs limits the possibility of tracing them back to their original acceleration sites, regardless of what energy could be registered on Earth. The only case in which this kind of extrapolation can be done is at the interplanetary level of the Solar system. Examples of this include interplanetary shock waves in relation to the solar wind or high energy radiation from solar flares [5]. As soon as the source of interest lies beyond interplanetary distances, the direct measurement of *in-situ* acceleration of hadronic matter cannot be reliably reproduced anymore.

To account for this difficulty the focus of astronomical investigations had to revert towards neutral particles. Historically this messenger has been always represented by photons. Even though they are not directly interested by magnetic field effects, photon at every wavelength do not travel unscathed towards us: it is possible that they can still interact with matter or other photons, harming observations e.g. at the VHEs [16]. If this doesn't happen, they will propagate straight from the acceleration site, possibly impacting our detectors in orbit or our atmosphere.

An alternative to photons applied especially to extragalactic astronomy has come from the IceCube collaboration in 2013, when it was announced that neutrinos quite possibly of astrophysical origin [17] could be detected up to the PeV energy range. This achievement has been not only the onset of neutrino research in extragalactic astronomy, but started *de-facto* the epoch in which this field could be investigated in a multi-messenger approach.

In addition to photons and neutrinos, the recent major discovery of gravitational waves [18] has paved the way for the use of a third messenger. Such tool can be, and has been, especially helpful to investigate interactions between compact objects and their environments ([19], [20]) and early cosmology studies where the surface of last scattering prevents the use of photons before (or beyond) the Cosmic Microwave Background [21]. Since the simultaneous use of photons, neutrinos and gravitational waves has been consistently applied in astronomy, this approach has by now acquired the name of *multimessenger astronomy*.

This work exploits the first two types of messenger, and it focuses in particular on their impact on VHE astrophysics. Both photons and neutrinos, especially when observed in the TeV and multi-TeV range, can help tracking the origin of CRs at higher energies - possibly up to the *knee*, i.e. 10^{15} eV.

As mentioned before, the knowledge of particle interactions at the site of CRs acceleration is critical in understanding their origin and energy spectrum as measured from Earth. Doing this means that the focus will no longer be on the CRs themselves, but on the secondary particles produced by their interaction with the environment near (or surrounding) the source location. This is the reason why cosmic ray physics can be carried out not only through ground experiments which look directly for hadrons or nuclei as they impact the Earth's atmosphere, but also by experiments which focus on secondary neutral products.

The advantage of this approach is that using other messengers than only the primary products at the acceleration site, we can get a glimpse also to particles that didn't escape the site or its surroundings. This allows us to also check for the composition of the material around the acceleration sites or the medium between them (intergalactic or extragalactic).

An example relevant to this work are extragalactic sources like AGN, especially if radio-loud. Sources belonging to this class of astrophysical objects are already known to emit powerful collimated jets of relativistic material in $\lesssim 10\%$ of the cases [22]. The emission coming from these events is dominated by non-thermal processes usually modelled via Synchrotron Self-Compton mechanisms focused on one or two emission zones: for long time this approach was sufficient to explain the observed spectral energy distributions. AGN are considered to be one of the more favourable sources from the point of view of the extragalactic component of CRs [15]. What is worth pointing out is that usually they are mainly observed through their radiative yields from radio to γ-ray frequencies [23].

A recent feature relevant to the extragalactic HE sky is related to the discovery of a diffuse emission of neutrinos [24]. The lack of any measured anisotropy in the detected PeV neutrinos supports the long-held hypothesis of a mostly extragalactic origin of these particles. Various types of sources have been proposed like Starburst galaxies [25] and hypernovae [26].

The second original part of this work deals with the data analysis of VHE γ-ray emisssion from a *blazar* observed to emit a ~ 290 TeV neutrino [27]. This result is the first of its kind and contributes to support the idea that blazars, and possibly other AGN classes, are one of the players in the production of the extragalactic component of CRs.

1.2 THE AIR SHOWER IACT TECHNIQUE

As mentioned in 1.1, an important effort in modern astrophysics is related to non-thermal physics. With time this meant that the focus of new detectors slid towards super-keV energies, from the hard X-rays to γ-rays.

Looking at the electromagnetic spectrum, upwards of 0.511 MeV (the energy of the electron at rest), the γ-ray band has no clear upper limit. This characteristic of the spectrum caused a gradual evolution in time of the concept of new instruments and facilities aimed at investigating radiation and particles from outer space. The first instruments to be used for this purpose were space-borne detectors. The reasons for their deployment were initially more military than scientific. Still, they were also the first to provide unexpected insights on extraterrestrial radiation phenomena [28]. This type of instruments continue to operate nowadays up to hundreds of GeV and few TeV [29].

As the spectrum of the measured radiation didn't seem to have any sort of unambiguous cut-offs, a need for investigating higher energies started to rise already around the end of the 80's [30]. In fact, for fluxes above $\gtrsim$ 100 GeV the detection rate for a γ-ray telescope becomes very low, e.g. for the Crab Nebula it is about 100 photons$/m^2/year$. This reflects a limitation in the collection area for such instruments (see 2.2.4 for a basic definition).

For space-borne instruments, overcoming this limitation would make the correspondent weight and size unpractical for space missions.

Beyond ~100 GeV two types of techniques are used to extract information on the incoming γ radiation or CRs: air Cherenkov and extended air shower (EAS) experiments. This work will not deal with the latter type, whose operating energies lie generally above the *knee* ($E \gtrsim 10^{15}$eV).

Many studies on EAS relevant to such energies are focused in particular on UHECRs [11].

Such facilities consist of arrays of fixed detectors on the ground. They aim to measure directly the secondary particles produced by EASs [31]: mainly muons, electrons or even neutrinos for some type of underground facilities.

Taking advantage of huge collection areas of the order of $\sim 1km^2$, at energies $\gtrsim$ 100 TeV the number of particles available at ground level is great enough to retrieve an image of the shower by fitting the particle densities throughout the entire array [12]. Examples of such facilities are the Pierre Auger Observatory [13] and the HAWK array [32].

At lower energies, between tens of GeV to tens of TeV, the shower development is not sufficient for enough secondary particles to be detected (due to absorption in the atmosphere). The best performances are carried out by the *air Cherenkov* experiments, exploiting what has been know as IACT.

As the name suggests, this approach consists in exploiting the Cherenkov light produced by extended air showers (EASs). The collected light is properly treated in form of projected images of the showers as seen from the ground. Compared to the previously mentioned case for GeV γ-ray space observatory, the typical effective collection area of a single Cherenkov telescope is $\sim 10^5 m^2$ [33].

1.2.1 Cascade showers

The first approximated theoretical model describing the development of showers, albeit of a purely leptonic nature, was proposed by Heitler [34]. This model is useful to understand the basic properties of cascade showers - the Monte Carlo (MC) simulations used in IACT experiments are based on the Heitler model.

The most basic version of the model focused on electromagnetic showers, describing the evolution of the chain reaction by means of the two main radiative phenomena involving only leptons:

- bremsstrahlung,
- pair creation of electrons and positrons,

both well described in the early paper from Bethe and Heitler [35].

In the case of the bremsstrahlung, the main discriminant is the amount of energy loss suffered from each electron, and in particular its comparison to the loss of energy caused by ionisation when interacting with atomic and molecular species in the atmosphere. For a typical cascade traveling in air, for which the correspondent radiation length is $37 g/cm^2$, this energy value peaks at about 80 MeV. This is referred to as *critical* energy, since below this threshold ionisation energy losses prevail over those caused by bremsstrahlung, effectively damping the development of the shower.

The model emphasises also the relation between the shower's geometrical size and content as a function of the primary particle's energy E_0:

- the maximum number of particles produced within the shower is proportional to E_0,
- the depth of the shower at which the production of particles is greatest is proportional to $ln(E_0)$.

It is worth mentioning that one strong point of the Heitler model is that the shower's length development is a function of the mean free path λ of the interaction (either of the two previously mentioned), and E_0 is described in terms of the critical energy.

This parametrisation in terms of λ and E_0 allows to apply the shower model to different media, not only air. This is of course important e.g to air-shower experiments, which exploit ground containers filled with water, instead of using the atmosphere as a tracking calorimeter device. Of course such showers, even if explained there in a first approximation, do not reflect the total amount of possibilities in which any shower could manifest itself in the atmosphere. Whereas a shower initiated by a γ-ray or by electrons and positrons will be almost only interested by the two leptonic process previously mentioned, any other particle such as protons and atomic nuclei of elements heavier than hydrogen will be interested more by hadronic processes.

In the case of showers of hadronic origin the dominant interactions are triggered by *spallation* processes in which the high energy proton or nucleus interact with the gaseous species at the top of the atmosphere (mainly nitrogen and oxygen).

This first process develops through pion production channels like,

$$\mathrm{CR} + \mathrm{N}_1 \rightarrow \mathrm{CR} + \mathrm{N}_1^* + \pi^0, \tag{1}$$

$$\mathrm{CR} + \mathrm{N}_2 \rightarrow \pi^\pm + \mathrm{N}_2^*, \tag{2}$$

where CR could represent both protons or higher atomic mass nuclei, N an atmospheric atomic nucleus at rest and N^* the possibly excited child nucleus which could also belong to a different atomic species due to nucleosynthesis. In this case the critical energy is greater than for purely leptonic showers, because the energy threshold for pion production is 1 GeV.

These processes give rise to a wealth of spallation fragments which will interact and decay with more production of pions and their decay products,

$$\pi^\pm \rightarrow \mu^\pm + \nu, \tag{3}$$

$$\pi^0 \rightarrow \gamma\gamma. \tag{4}$$

Such products will be mainly muons and neutrinos, which will be able to reach the ground more often than other secondary particles thanks to their half-life and weak matter coupling respectively. An important point is made by the second reaction in (4): the neutral pion decays preferentially into a pair of photons, giving rise to a sub-electromagnetic shower which if isolated would look exactly like any other.

The difference between γ (or e^+ e^-) initiated showers and these secondary showers of hadronic origin is mainly that, due to the neutral pion decay, the latter type will tend to develop off-axis with respect to the main shower axis.

This effect reflects on the entire hadronic shower since the quantity of possible interactions and secondary products is higher than in the pure electromagnetic case: showers of hadronic nature will be wider and more delocalised at the ground than showers initiated by e.g. γ-rays.

A critical aspect of atmospheric-based VHE experiments is the amount of complexity contained in the detailed MC simulations which are required to model properly these processes.

1.2.2 Single shower treatment by IACTs

Exploiting the production of Cherenkov photons by the charged secondary particles developed within the shower, the final measurable quantity in which IACTs are interested is - ideally - the total amount of such photons at the site in which the shower base will be stopped.

The Cherenkov photons produced by an electromagnetic shower at the front [33] will reflect more the geometrical development of the shower resulting in a more uniform and contained amount of Cherenkov photons.

For each shower, an IACT aims to retrieve the main geometrical parameters describing the cascade of particles, through which to implement backwards the previously described processes via a statistical treatment through MC simulations.

The main parameters relevant for the study of the Cherenkov cascade shower are:

- altitude of the observational site,
- surface density of the Cherenkov photons at such altitude,
- angular distribution

A shower will reach the maximum production of Cherenkov photons at an atmospheric depth correspondent to an altitude of ~ 10 km a.s.l. at TeV energies. Under such conditions, the opening angle of Cherenkov light in the air is $\lesssim 0.7^{\circ}$, resulting in a shower base radius of about 100 to 150 meters. These key values set the minimum size limits of the reflective surfaces of an IACT, given the reflectivity power of the mirrors and the quantum efficiency of photo-sensors [33].

The correspondent Cherenkov photons contained in the light pool are then collected by a set of mirrors and focused onto a camera. The photosensors, i.e. photomultipliers, which compose the camera transform the photo-counts (that correspond to the set of collected Cherenkov photons) in electrical impulses, from which a first timing information is retrieved.

The flash corresponding to the sequential projection of the photons contained in the shower base light pool lasts a few nanoseconds. So an additional limitation of any IACT is given by the performance timescales of the photomultipliers and the electronics which carries the converted signal.

The next fundamental step in the treatment of a shower image is done offline, when each event (at this stage each recorded image) is processed separately focusing on two main steps:

- cleaning of the image from noise and Night Sky Background (NSB) influence,
- parametrisation of each image with the method developed by Hillas [36].

The former step is required in order to eliminate from the images effects related to artificial sources of noise related to the electronics setup, noise created by shower tracks too far from the telescopes and with a Cherenkov light density too low to be reconstructed, and fluctuations given by NSB sources (stars, the Moon, ecc...).

The latter step, i.e. the parametrisation of the image, is critical in order to produce the required information later needed by an analysis pipeline, so that events which arose from γ-rays can be discriminated over the background given by hadronic showers or any event related to noise or NSB which survived the initial cleaning process. Time arrival information is used at this point to identify correlated Cherenkov counts reaching different photosensors.

The image parameters characterise each projected shower image recorded by the PMTs of the camera. Fig.2 shows an example of an image fit procedure and the some relevant image parameters associated with it.

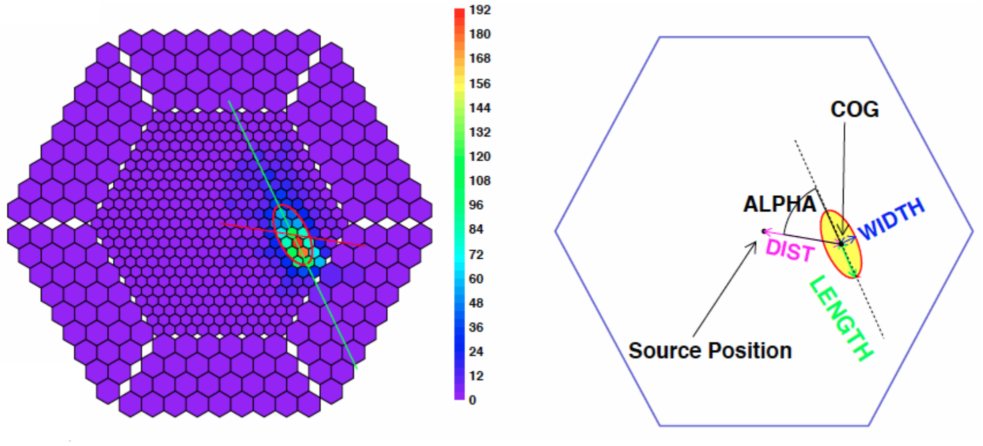

Figure 2: Left: Example showing the fit of a single event recorded by one of the MAGIC cameras, where the colour scale represents the amount of photoelectrons per pixel; Right: some of the main image parameters associated with the fitting procedure. Credits: Dr. Saverio Lombardi

Some of the main image parameters most relevant for this work are e.g.:

- *size*, number of photoelectrons in the image; approximately proportional to the energy of primary particle for a given shower impact parameter and zenith angle,
- *width*, half width of the minor axis of the shower fitted ellipse; helpful in discriminating between primary γ rays and hadrons, being related to the transversal development of the shower,
- *length*, half length of the major axis of the shower fitted ellipse; correlated instead with the longitudinal development, which is generally larger for hadronic showers and those with larger impact parameters,
- *leakage1/2*, fraction of total image size distributed in the one and two outermost camera rings respectively; this parameter is higher for too large impact parameters, resulting in signal loss and incorrect reconstruction.

The combination between image parameters and timing information allows us to identify more of the elliptically-shaped images arising from electromagnetic showers against the more scattered and less homogeneous hadronic counterparts. An example is shown in Fig. 3.

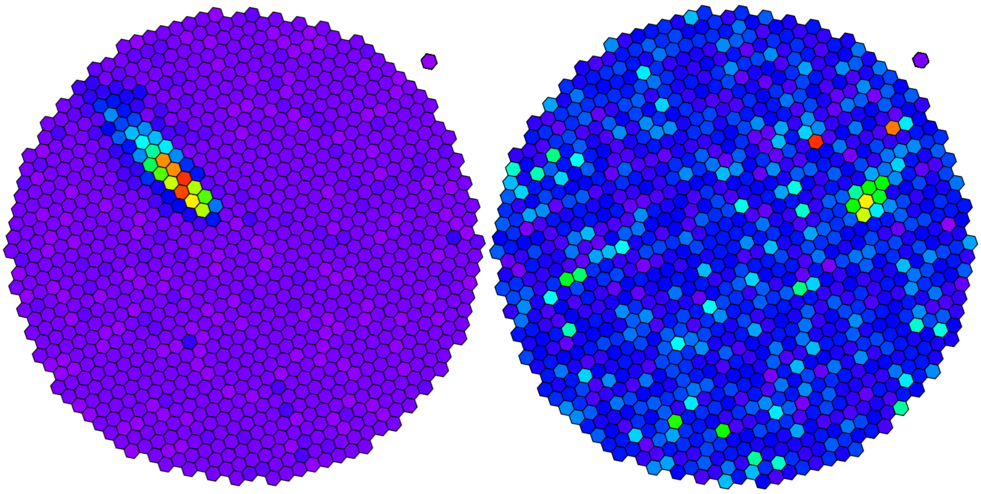

Figure 3: Comparison between simulated events. Left: gamma-like, Right: background-like. It is evident how the first is more easily recognisable than the second, when submitted to the procedure of image fitting.

1.2.3 Reconstruction of stereoscopic events and their position in the sky

A fundamental improvement in the IACT operation has been the implementation of multiple telescopes. A limitation of using a single telescope to observe air-showers is that if only one image is projected on the camera, it is subject to a degeneracy: the real direction of the shower could in principle be either of the two along the maximum axis of the projected image. In short, the IACT is inherently stereoscopic.

In the case of single Cherenkov recording instrument, the method implemented to solve the degeneracy was already available, even though with limited performance.

Introducing one (or more) identical instruments solves this degeneracy as I will outline in the following.

It is a two-step process starting with the estimation of the "Distance between the Image centroid and the Source Position" or DISP, where the centroid represents the pixel equivalent point of maximum concentration of Cherenkov counts within the fitted ellipse. The images themselves, except for the relatively rare case of perfectly perpendicular direction with respect to the telescopes dish, are never perfectly symmetric. This real-case scenario asymmetry allows us to consider a set of parameters which describe it sufficiently well to identify a preferred direction; one of such parameters can be the gradient of arrival time of the Cherenkov counts along the main axis of the projected image.

The current standard method implemented by MAGIC uses the Random forest method in order to estimate the DISP parameter (see also 2.2.2).

The combination of both the DISP parameter and one (or more) asymmetry-related ones can help in estimating the most likely arrival direction (see Fig.4.

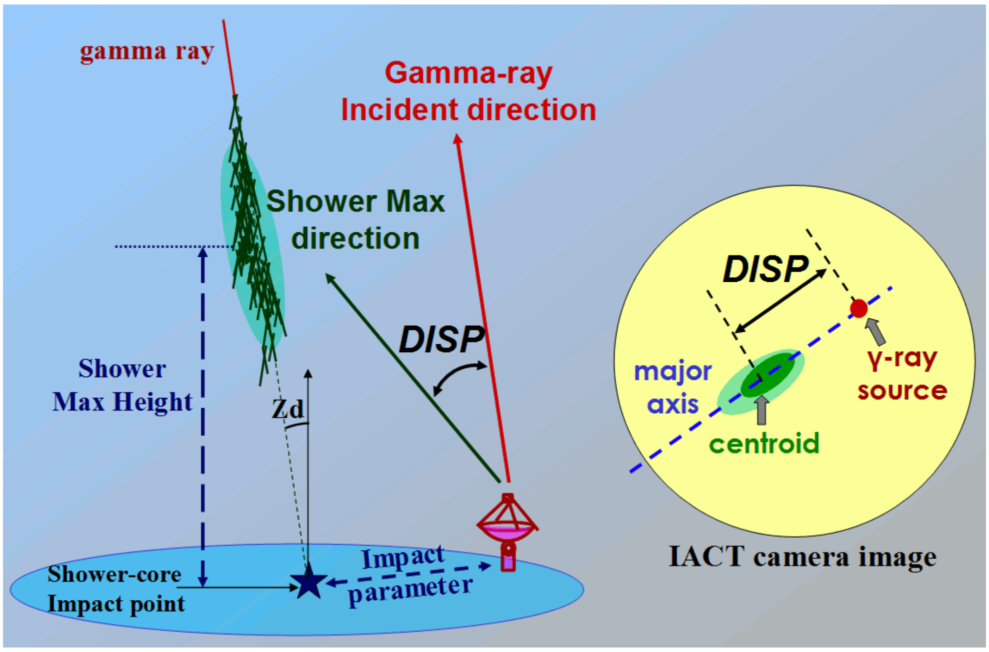

Figure 4: Description of the DISP method for the case of a single telescope. Credits: Dr. Pierre Colin, MAGIC collaboration.

After fitting each projected image in the cameras through the method illustrated by Hillas [36], a major axis is defined through the resulting ellipses.

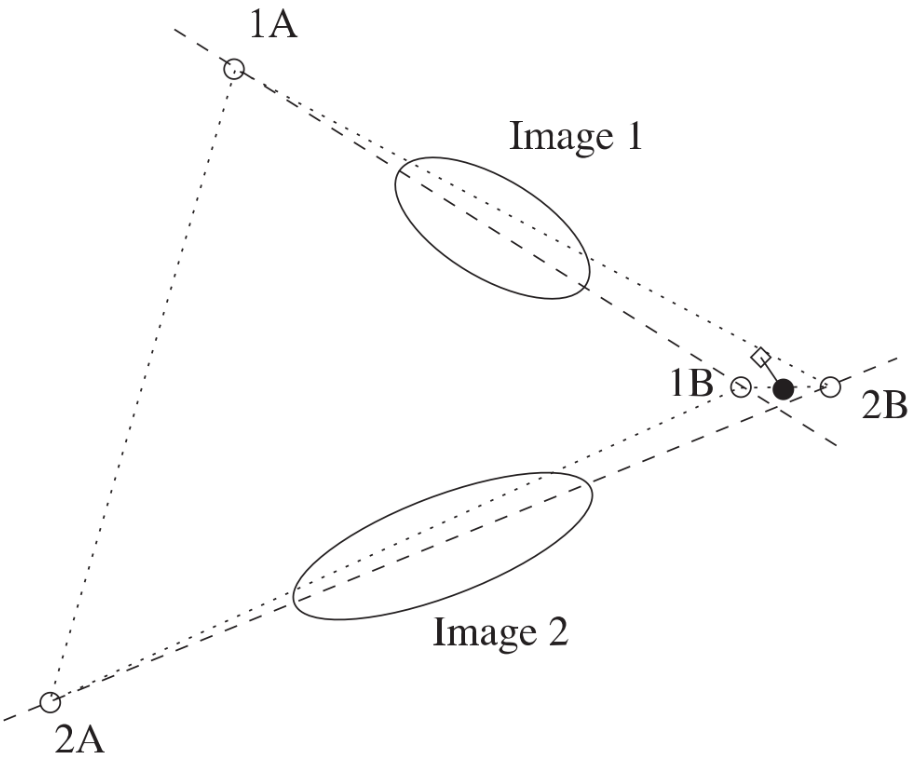

Figure 5: Description of the Stereo DISP method as reported in [37]. Dashed lines represent the major axis of the projected images. Empty circles show the reconstructed positions using the DISP RF method. Dotted lines show the 4 distances which connect the pairs of reconstructed positions for each telecope. The filled circle shows the final reconstructed position, while the true position of the source - in arbitrary camera coordinates - is marked with a diamond.

1.3 THE CASE FOR VERY LARGE ZENITH ANGLE OBSERVATIONS

As understood from 1.1, in order to thoroughly investigate CRs, experimental and observational techniques needed to adjust to each other in order to provide energy and flux measurements over many orders of magnitude. IACTs are self-standing in this respect, since they also access energies through about 3 decades in energy, from tens of GeV to tens of TeV.

In the last few decades the access to energies ranging from hundreds of GeV to few TeV have shown that the gamma-ray sky is filled with different populations of sources (see e.g. Fermi-LAT 3FGL catalog). The extrapolation of their spectra to energies above tens of TeV shows that current gamma-ray observatories start to be not sufficient to appreciate the lower flux at such higher energies.

In the general case of the overall cosmic ray spectrum, the flux of particles with energies above orders of TeV is $10^{-5}\text{cm}^{-2}\text{sr}^{-1}\text{s}^{-1}$, meaning that 10^{5}m^{2} are already needed to detect about 10 showers per second. Given the constraining nature of the flux, shown in Fig.1, this means that increasing the energy requires either a greater amount of integrating time, or a greater area to appreciate the same amount of showers in the same observational time. This aspect is especially interesting since, unless we dedicate huge amounts of time to single sources with currently available observational facilities, in order to reach the required sensitivity it seems necessary to wait for new-generation instruments, such as the Cherenkov Telescope Array [38].

A possible solution is to extend the observation of an IACT to higher zenith angles, or lower elevations. In this work I will describe my contribution to the observations and data analysis techniques optimisation for MAGIC at VLZA. The reason for this is directly related to the properties of the shower propagation in the atmosphere. At higher zenith angles the propagation distance of the cascades increases dramatically due to the atmospheric profile as seen from a ground reference point.

As described by the toy model summarised in 1.2.1, the geometry of a cascade shower mainly depends on the energy of the impacting primary particle. In a first approximation, the geometry of the same shower will remain the same even at higher zenith angles with the only difference that the developing distance will be much longer - up to ~ 100 km at zenith angles ~ 75°. This means that in principle an observer on the ground would be illuminated by a larger Cherenkov light pool when focusing on showers at lower elevations.

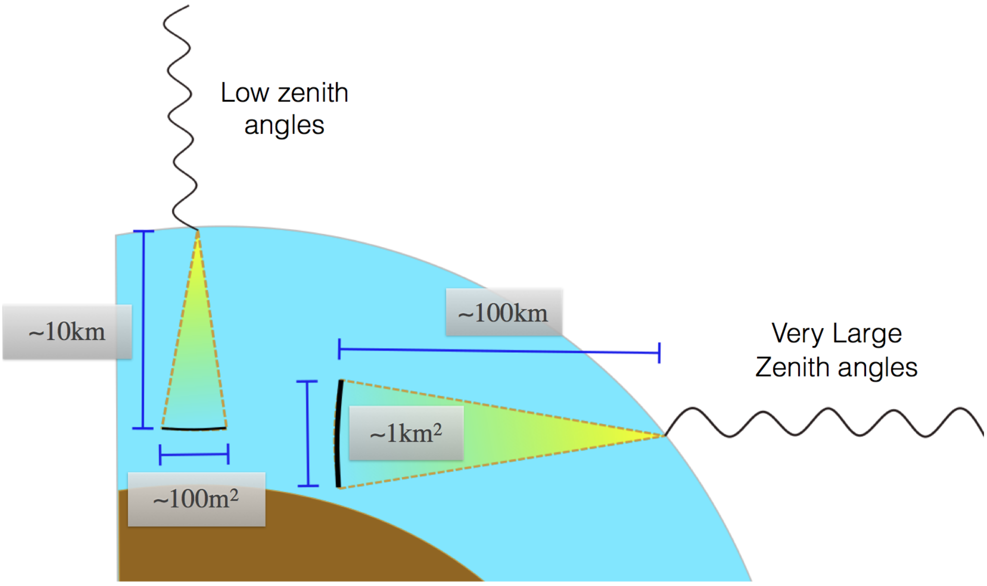

Figure 6: Sketch showing the working principle of VLZA observations: pointing to lower elevations the Cherenkov light pool increases and so the accessible collection area.

This effect, which up to this point is purely geometrical, will then combine with all the remaining information that each shower carries, which in first approximation is enclosed in the number of photons contained in the light pool.

For primaries of lower energy, the longer cascades will suffer increased absorption for same propagation distance with respect to primaries at high energy. The reason is mainly because there is more material along the LOS at lower elevations. This translates in a greater suppression of low energy events, which in turn increases the energy threshold, allowing us to access the highest energies - possibly up to 100 TeV.

Not only would the average energy of the measured events be higher, but, thanks to the higher energy of the primary, the associated lateral distribution of each Cherenkov shower will be wider, resulting in an increase of collection area at such energies. Estimates carried out at regimes of high zenith ranges suggest that for a 10 TeV event the collection area increases of about 3.5 times just lowering the telescopes from 30° to 60° in terms of zenith angle [39].

However, there is a number of limitations which prevent a clear and direct assessment of the technique. As any other IACT facility, the MAGIC telescopes exploit the atmosphere as the calorimeter of a physics experiment. This means that prior knowledge of its composition and condition in real time during the observations is critical to its use. A certain level of precision on this is clearly needed, since, from the point of MC simulations, we can never benefit from a perfect real-case scenario at all times.

The atmospheric profile doesn't scale linearly with the zenith angle: its thickness varies rather quickly while the telescopes follow a source to lower elevations.

Also, since the intrinsic physics of the showers doesn't change, the initiating point of the chain reaction if far away from the telescopes with respect to the usual distances associated to smaller zenith angles.

In addition to the general concepts commonly applied to any shower, those at VLZAs can be especially influenced by sudden changes in transparency caused by dynamical variations of the atmosphere even on the scale of hours.

Even if much more difficult to handle, VLZA observations represent today a good alternative for the investigation of multi-TeV and possibly sub-PeV gamma-ray cosmic radiation. The current main target for VLZA angle observations are galactic sources for which flux measurements at higher energies would place them in the class of Galactic Pevatrons. This could likely be a set of sources and not a single type of objects.

Along with the very important points made by the boosted collection area and energy threshold, another main advantage of VLZA observations is the increase in the accessible area of the sky for any given observatory - if, of course, the given facility permits such pointings, which could be limited by both structural weaknesses or natural obstacles (such as the Roque De Los Muchachos mountain in the case of MAGIC).

2 THE MAGIC TELESCOPES

As one of the three currently operating IACT facilities (the others being H.E.S.S. [40] and VERITAS [41]), the MAGIC collaboration operates a pair of air-Cherenkov telescopes working in stereo mode from 2009 and further upgraded in 2012 ([42], [37]). The observation site is located on the island of La Palma (Canary Islands, Spain) at an altitude of about 2200 m above sea level.

Table 1 reports some operating parameter values related to the current camera, valid for each of the two telescopes after the 2012 upgrade [42].

Table 1: Main hardware characteristics of the MAGIC telescopes

Sampling	2.05 GS/s
Dead time	27 μ s
Total pixels	1039
Trigger pixels	547
Trigger area	4.3°
Field of view	$\sim$ 3.5°

Figure 7: The MAGIC telescopes system with MAGIC-II in the front [42].

The MAGIC telescopes have a diameter of $\sim$ 17m covered by 964 square all-aluminum mirrors with a side of ~0.5 m, resulting in a reflective area of

$236\mathrm{m}^2$ [43]. They are provided with an event recording frequency of ~10^9 Hz and a 1039-pixel camera each, allowing them to detect fast Cherenkov light from EAS within a field of view of 3.5°.

The nominal energy range MAGIC can investigate goes from few tens of GeV [44] to tens of TeV [45]. Part of this thesis investigates the possibility to optimise the data acquisition and analysis in order to reach energies up to 100 TeV.

During nominal observation nights, operations are monitored against natural and artificial dangers which could damage the telescopes. Some important limits related to the local weather conditions to operate the telescopes are:

- Mean wind speed below 50 km/h,
- Wind gusts speed below 40 km/h (a lower value, due to the such impulsive forces acting on the camera),
- Humidity must be $< 90\%$, with an absolute limit of 98% to operate hardware at high voltage,
- no rain - nor, even worse because of the mirrors' sandwich structure of the [46], snow and ice.

If any of these conditions is not met, depending on the particular situation an automated or manual response is triggered, aimed at parking the telescopes in a safe configuration. This also prevents successive observations for at least 20 minutes.

2.1 RELEVANT PARAMETERS AND SUBSYSTEMS

2.1.1 Direct current

The MAGIC collaboration has established important results regarding the analysis of data in non-optimal conditions, which led to notable accomplishments like [47]. As explained in 1.2, the Night Sky Background (NSB) is strongly affected by moonlight at different levels. The average DC of the cameras, measured through the photomultipliers in the camera, increases proportionally to the NSB, associated with a higher photoelectrons (phe) rate. Thanks to a proper treatment of the discrimination thresholds at hardware level, the amount of accidental photoelectrons accumulated by the photomultipliers is kept stable during operations. This is not sufficient to completely eliminate the noise per pixel, because too high values can create islands that do not correspond to real event images. This in turn affects image parametrisation by spoiling the fit to the projected images, resulting in wrong Hillas parameters.

Given such possibility, during any analysis the analyser can judge the power of the image cleaning - depending on whether or not the used data is already at the stereoscopic level - using the percentage of pedestal events that survive the process. Taking into account the energy threshold of the analysis and the required systematics, the actual limit could in principle change between different analyses, but a standard reference value is usually 10%.

2.1.2 The MAGIC Elastic LIDAR

One of the main sources of systematic uncertainties in IACT instruments is the limited control over the atmospheric influence.

In particular each measurement depends on the assumed atmospheric profile and on possible variations within each time window in which data is collected. Main sources of disturbance within the atmosphere are represented by water vapour from clouds or wind-borne dust.

The reason why IACT measurements are so sensitive to these factors is because they directly modify the main observable of such instruments, i.e the final number of Cherenkov photons reaching the mirrors.

Such quantity is modified by at least:

- the refractive index in the (mainly) gaseous medium, modified by the instantaneous atmospheric profile along the vertical direction,
- the scattering and absorption of Cherenkov photons caused by atomic or molecular targets and bigger particles like dust or aerosol.

Since the shower maximum is normally occurs at an altitude of ~10 km [12], it makes sense to worry about these estimates from such altitude downwards.

The main instrument devoted to evaluate atmospheric transmission for the MAGIC telescopes is the MAGIC Elastic 'micro'-LIDAR [48]. The MAGIC LIDAR, acronym which stands for "light detection and ranging", is a moderate laser system operated at a single wavelength, whose purpose is to monitor atmospheric transmission as a function of time and distance via backscattering to a light detector. The MAGIC LIDAR system is placed in a dedicate dome, on top of the counting house where the shifters operate the MAGIC telescopes as shown in Fig.8. The reader is referred to [48] for hardware and operational details.

In a first approximation, the raw estimated energy after stereo reconstruction (see 1.2.3 for a general description, and 2.2.3 for application to VLZA data) linearly depends on the Cherenkov light pool content. Since the material scanned by the backscattering laser is directly responsible for the absorption of such photons, the atmospheric attenuation too is related to energy damping in a proportional way [48].

Figure 8: The MAGIC 'micro' LIDAR system in its dedicated dome on top of the MAGIC counting house [48].

After evaluating the dependence of atmospheric extinction on distance from the telescopes, the derived correction values are applied to the reconstructed data event-wise scaling the estimated energy by the inverse of the optical depth resulting from the LIDAR measurement. The corrected events become more similar to lower-energy ones, thus reducing the effective collection area. The corrections will then have to be re-applied bin-wise to the calculation of the effective collection area, which is necessary to retrieve the estimated flux and, along with it, the higher-level analysis products (see 2.2.4).

Standard reference values for LIDAR-measured transmission T adopted by the MAGIC collaboration are here qualitatively classified on the basis of the official studies [49] (all values refer to a distance of 9 km):

- very good: $T > 0.85$,
- good, but should be corrected: $0.7 < T < 0.85$,
- bad, but can be corrected with caution: $0.55 < T < 0.7$
- very bad, correction is not possible nor advised: $T < 0.55$.

An alternative method is simulating specific atmospheric conditions by means of dedicated MC simulations; this is not usually done, since LIDAR corrections are sufficient for most of cases, but has proved useful in obtaining important results such as the one reported in this work (chapter 4).

2.1.3 Pyrometer

Among the instruments that aid the MAGIC telescopes during observations, a secondary one is the pyrometer. Generally, the pyrometer is a device which aims to measure a temperature through thermal radiation. While on the market the choice is basically divided between contact and remote-measurement instruments, in astronomy the latter class is of routinely used: in this case we talk of radiation pyrometers.

The MAGIC telescopes are equipped with a single pyrometer, mounted on the MAGIC-1 dish. Moving together with the structure of the telescopes, as shown in Fig.9, it points constantly to the same region of the sky having a field of view of 2°. It operates in a mid-infrared subrange, from 8 to 14 µm, accessing a nominal temperature range between -100 and 3000 °C with a resolution of 0.01 °C.

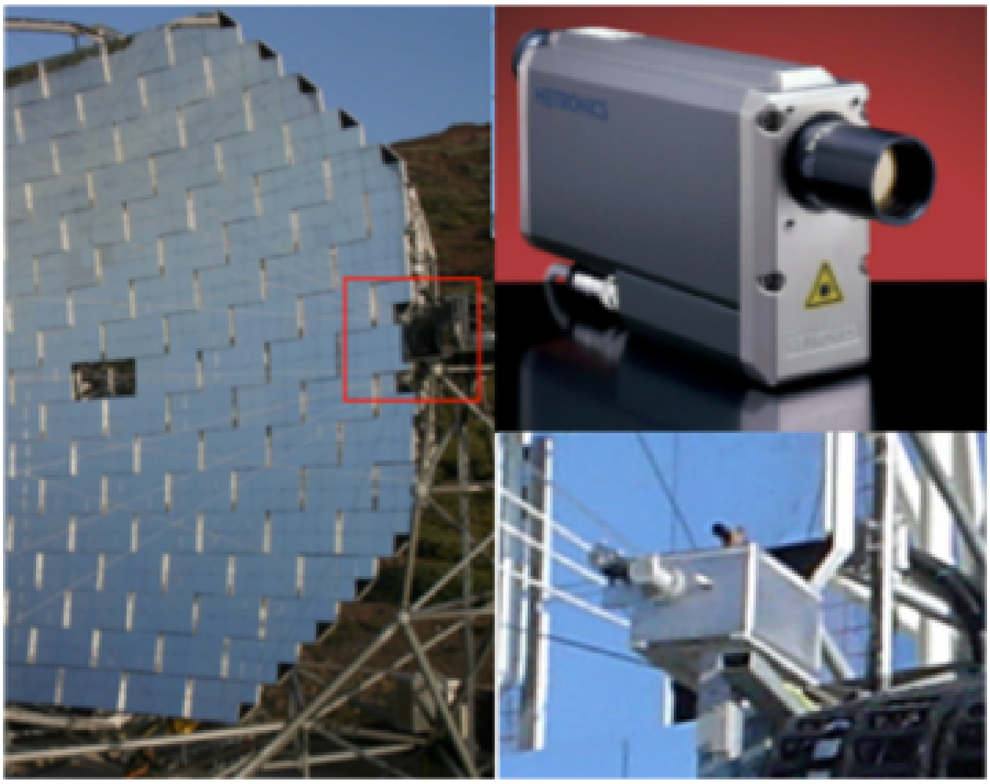

Figure 9: The MAGIC pyrometer as currently mounted on the structure of MAGIC-1. Credits: MAGIC collaboration.

In the case of radiation pyrometers, the surface to which the measure is directed is the sky itself. The temperature measurement is the surface integral of the flux of thermal radiation within a fixed solid angle given by the field of view of the instrument. The radiation received by the instrument is focused on a thermoelectric sensor by means of an optical system.

The observable effectively measured by this instrument is the sky's temperature. However, in order to convert this quantity in a more similar one to what the LIDAR estimates differentially, a *cloudiness* parameter converts empirically sky temperature into the amount of absorbing material which in terms of mid-infrared radiation should appear to be warmer as more material is clustered together. This empirical estimate is made by means of both local and remote quantities, such as temperature of the air and humidity.

Unfortunately, there has not been a proper study of the pyrometer: some tentative calibration has been done with the aid of the LIDAR even if with wide parameter dispersions. As a result, the MAGIC pyrometer is only used when the LIDAR is not available and mostly at low zenith angles.

2.1.4 Starguider

Both MAGIC telescopes are equipped with a *Starguider* CCD camera, placed in a dedicated environment at the centre of their dishes. The main use of each of them is to aid the corresponding drive system of the telescope to monitor, and eventually correct, the nominal pointing position during the data taking operations. The correction is done online while pointing the telescopes to any scheduled source, but is also applied event-wise by default in the standard analysis chain.

This subsystem returns two similar quantities which is possible to use later in the analysis chain. Both of them represent a nominal number of objects as recognised by the cameras: number of *identified* stars and *correlated* stars.

An important difference is that while the first can refer to any feature bright enough to appear in the field of view and to be recorded, only using the second can the analyser be sure to deal with actual stars. This is because the software, which also takes care of the pointing accuracy given the bending models for the telescopes, after registering the digital information from the camera's pixels superimposes a table of known stars on the observed sky's field. Using this second variable, only the features coincident with real stars in the field of view for the current coordinates pointed by the telescopes will be registered and counted.

This measurement gives an indirect measure of the atmospheric attenuation in the FoV of the Starguider cameras, which is approximately the same as the real cameras ($4.6\ \mathrm{deg}^2$). The number of *correlated* stars (i.e., *real* stars) can then be used as a viable observable in absence of more reliable instruments such as the LIDAR (2.1.2), since the number of visible stars, even at naked-eye gives a measure of the amount of absorbing material in the atmosphere - in particular clouds. However, it has to be treated carefully, especially at high zenith angles (3.2.3).

2.2 STANDARD STEREO ANALYSIS PIPELINE

The analysis techniques employed by the MAGIC collaboration are implemented numerically in the *MARS* software [37], a set of routines based on the ROOT framework. Classes within MARS map the telescopes subsystems and encapsulate different steps of the analysis in executables.

Here I will describe the parts relevant to the understanding of the next technical chapters.

2.2.1 Data quality

Since the MAGIC telescopes are constantly aided by auxiliary instruments, the data quality process is parallel to the analysis of each air shower event and can be applied at any step. This is valid until the point of flux estimation, since there data is usually supposed to be corrected for LIDAR transmission measurements - 2.1.2).

To this aim the first operation to be carried out usually consists in checking the quality of the operations carried out by the human operators on-site.

Hardware failures, human errors and damage of the instruments due to natural causes can occur at any time during the data taking, so a first look into the *runbooks* helps eliminating those runs or even nights in which no proper handling of the data could be carried out.

The standard data quality software within the MARS framework operates directly on the data runs at various levels. Each of the subsystems will register its own measurements in dedicated ROOT containers, from which the software will read them afterwards.

The program allows the analysers to choose different cuts and apply them to the data in a single call. Two main modes can be used: run-wise or through time slices of user-defined length. Each execution will operate on the files in the same way, regardless of the operation mode.

For each enabled cut on a single parameter, the software will create a distribution of the cut values within the chosen time interval. A median is then extracted from the distribution and is used as a discriminator for the data slice at hand, depending on whether its value falls inside the interval defined by the user's cut. It is clear that the time slice mode is more precise since the interval on which the distribution is done can be much smaller than an entire run, which usually takes $\sim$ 20 min. In the latter case, if the median of even one parameter distribution lies just outside the defined interval, the risk is that the software will label the entire run as *bad*, thus loosing almost half of the data, corresponding to the events whose parameter values were instead within the cut's interval.

An important operation carried out when executing the data quality software is the proper handling of transmission data from the LIDAR (cfr 2.1.2). The raw measurement from the dedicated computer which controls the LIDAR system does not include corrections for e.g. temperature and time degradation. These operations are only applied offline by this software which calibrates and corrects the first measurement "on the go". In this sense, the transmissions calculated within the step of data quality are more accurate that the ones that on-site operators can see online during data taking. The resulting value is the one that will end up being used by the event reconstruction and flux estimation softwares.

2.2.2 Gamma hadron separation

As explained in 1.2, the main purpose of an IACT experiment is that of tracing the astrophysical information about γ rays impacting the atmosphere. Given the overall flux of particles interacting with the Earth, the count rate of γ radiation is in fact negligible, being dominated many orders of magnitude by that of CRs. Because of this, CRs usually constitute a background to the signal, its bulk being given by protons and light nuclei, which make up for almost the entirety of the CRs counts (1.1).

The projected images on the cameras are critical for discriminating between γ-ray signal and diffuse background, as shown in Fig.3. The parameters involved in the process of background rejection are related to the shape of the events as seen in the camera, to their arrival times, but also to the reconstructed direction (see 1.2.3).

The standard approach followed by the MAGIC collaboration is outlined by the algorithm called Random Forest [50]. In this method the parameters chosen for background rejection are randomly selected in subsets; then they are used as discriminators at the nodes in a number of decisional trees. Each node acts like a filter for each event inserted in the tree, resulting in a final judgment by the algorithm which classifies each event between two possible choices: γ-ray or something different. At the end of the tree the event will have its own label, and inserting the same event in all the trees (hence the name *forest*), the average value corresponding to the set of tree-wise decisions (each of which can be thought to be 1 or 0) is a decimal value which takes the name of *hadronness*. For a hadronness value of 0 the event is recognised by the Random Forest to be a γ ray, whereas 1 means a background event.

Both the numbers of nodes and of trees can be chosen at will, depending on the particular case at hand and on the available computational power. At higher energies, the gamma-ray projected events have a more definite shape with respect to the background images because of a greater number of photo-counts in the ellipse. As a consequence this gamma-hadron separation method generally performs better.

An important point, particularly effective in case of non-standard analyses, is that also the set of parameters to be exploited by the Random Forest is not fixed. This can prove useful in order to find an increased number of discriminating properties, but could also prove time consuming.

2.2.3 Energy estimation

Following the process of image cleaning and parametrisation, a method of energy estimation is applied to each event. Currently, two possibilities are used in the MAGIC data analysis. Both methods rely on simulated MC data and on a set of common cuts aimed at ensuring the use of registered events which are physically correct and comparable between the two telescopes (e.g. recognised stereo reconstruction).

Look-up tables

The first method, which is the standard in MAGIC, is done via look-up tables (LUT) and is performed in two steps. First the measured Cherenkov light density and impact parameter (1.2) values are linked against the estimated energy of a simulated primary particle, by means of an ideal air-shower emission model.

Since such a model is far from being a real-case scenario, a number of approximations have to be taken into account:

- atmospheric absorption (which is zenith dependent, see also 3.4.1),

- azimuth dependence (see e.g. 3.3.1),
- images which, when projected, are not fully contained in the camera (especially at high energies, where the image area increases due to the higher number of photoelectrons in the cascade light pool at ground level).

After these corrections are applied to each telescope separately, from the resulting pair of estimated values the final average value is weighted by the inverse of their uncertainty [37]. This value is later considered as the one to be used at higher-analysis levels.

From the set of image parameters and the retrieved value of estimated energy, a reference table for each telescope is built. Such table will be subsequently implemented telescope-wise, when other quantities such as the *Hadronness* (2.2.2) will have to be assigned to the stereo reconstructed events.

Stereo Random Forest energy estimation

An alternative method to estimate the incoming event's energy uses the same concept described in 2.2.2 for gamma-hadron separation.

The algorithm of Random Forest is used applied in this case as a regression method to estimate the energy from a set of parameters, previously defined for each event as described in 1.2.2. This procedure relies on stereoscopic data and has been recently approved for use within the collaboration.

One limitation of this procedure is that, since the training is done also by means of the MC data, the maximum energy strongly depends on the maximum simulated value. Therefore, in cases such as described in 3.4, the production of higher-energy simulations is necessary. This constitutes an additional limitation in terms of time and computational efforts.

Performance studies have demonstrated that the stereo RF energy estimation method behaves better than its LUT counterpart, in terms of both energy resolution power and bias, with respect to the true energy simulated in the MC data (see Fig.10).

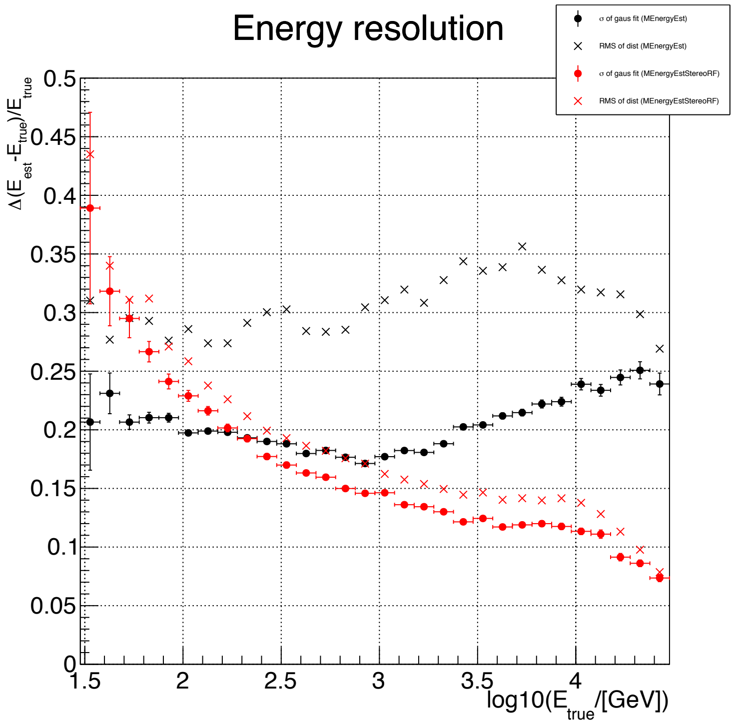

Figure 10: Comparison between the performance of stereoRF (red) and LUTs energy estimation method (black). Point and crosses show the standard deviations and the root mean squares associated to each energy bin of the migration matrix. Courtesy of Kazuma Ishio.

In particular this is especially true at medium energies, were statistics are higher, and at high energies, because the RF forest method is more robust for images whose projection occurs at the edge of the camera.

Partially contained images would be estimated to be less energetic by the LUT (with respect to wholly contained images), since the number of registered photoelectrons is lower. This is particularly important for VLZA showers which have broader light pools (1.3).

2.2.4 High level analysis concepts

Effective time

During data taking operations, the instrument will not work continuously throughout all the scheduled time for observations. Reasons for this are related to both hardware failures and intrinsic properties of the data acquisition system.

Leaving aside casual interruptions due to malfunctions or weather-induced stops, the most important systematic aspect that defines the effective time of the final analysed data is the *dead time* of the instrument.

The dead time represents the set of all time intervals within an observation in which the detector part of the MAGIC system was unable to record any new event. This happens to any digital system since, after receiving the input signal, the data acquisition channels are busy transferring the newly registered data, so for some time they cannot process any later incoming events.

This of course reflects in a reduction of the recordable rate of events, even though the last MAGIC performances fix this dead time at only 27 μs (see Table 1 for a summary of the main performance parameters).

Consequently, after the stereo events have been fully analysed, the final scientific results, such as detection significances and flux related quantities, have to take into account not only possible time losses due to external causes and analysis cuts, but also the time losses due to the intrinsic hardware limitations (i.e., the dead time).

Pointing method and signal estimation

The standard approach the MAGIC telescopes implement while pointing to a source makes use of the so-called *wobble method* [51].

This method relies upon taking data from a position of the sky which is slightly offset from the position of the source of interest (ON position). The reason for this choice is to be found in the comparison with older methods, e.g. the apparently obvious choice to look directly at the source position. If this were to be the chosen pointing method, in order to be able to properly estimate the background and calculate the resulting θ^2 angular squared distribution of the events, additional observations would need to be carried out while pointing at a background-like region of the sky, different from the previous one (OFF position). Such technique would take advantage of the camera centre being associated with the FoV for both the source and the background, resulting in better acceptance. However, doing so would effectively double the observational time for a single source, resulting in obvious limitations when scheduling multiple sources in a given night.

Alternatively, *wobble* observations allow the source to be kept in the camera at all times, rotating around the centre (provided that the telescopes operate in an alt-azimuthal mount configuration) while at the same time allowing for data taking to continue from other sky positions (see Fig. 11).

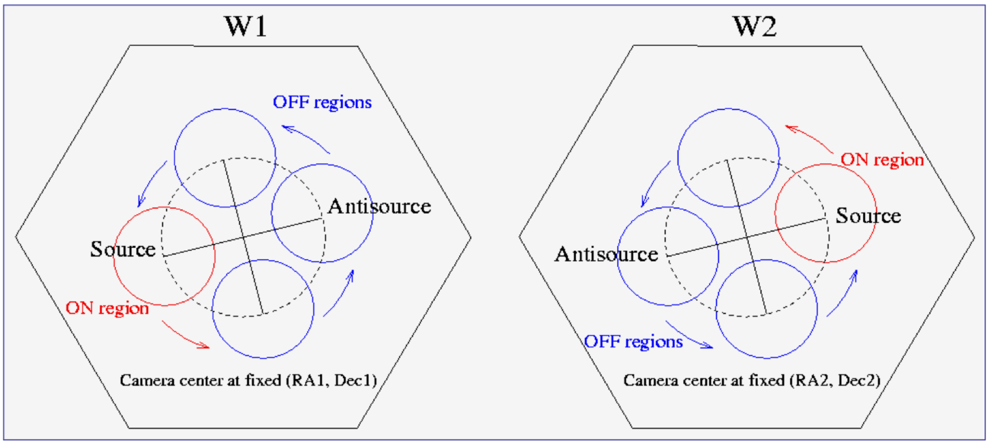

Figure 11: The wobble method shown in the particular case of two wobble positions W1 and W2, each using 3 simultaneous OFF regions. While the source's position rotates on the camera due to the alt-azimuthal telescope mount, the pointing is offset from the source in symmetrical positions (here with 2 wobbles only left and right). Credits: MAGIC collaboration.

The associated acceptance choice will then be the same, even though not as optimal as in the centre-field case, because of the slight offset; nonetheless, this method provides two positive aspects.

The background region is directly accessible within the same FoV, e.g., anti-symmetric with respect to the centre of the camera in the simplest case. It is also possible to define multiple background regions in the same observation, a process that takes the name of *simultaneous background* approach.

Independently of the number regions used to estimate the background, the procedure of background subtraction consists in counting the events recorded in the OFF regions and subtracting them (after normalisation) from those simultaneously recorded in the ON region.

Flux estimation

A key parameter which dictates the efficiency of a general particle detector is the so called *collection area*. This area, which in the case of MAGIC is usually referred to gamma rays, corresponds to the area of an ideal device. Such a device would detect all the gamma-rays impacting its surface with a total background rejection, in which the only real input would be the rate of events registered by the real experiment (which is not an ideal case).

In the case of an IACT the reference surface would be the one corresponding to the maximum impact parameter simulated in the MC data A_{MC}, so that the collection area - at the trigger level - can be written as

$$A_{eff} = \frac{N_{trig}}{N_{sim}} A_{MC}, \tag{5}$$

where N_{sim} and N_{trig} refer to the number of events which have been simulated and have survived the simulation respectively.

Given that MC data is available from the beginning, this estimation can be carried out at different levels in the analysis: in the case of higher-level results the correspondent quantity will take into account also the higher level cuts (hadronness, θ^2, energy to name the most important ones). In such a case we talk about *effective* collection area.

Upper limits on the measured flux are calculated making use of the Rolke method [52], with a standard confidence interval of 95%.

Unfolding procedures

After the energy reconstruction process provided each event with an *estimated* energy E_{est}, an experiment is still limited by the fact that all the quantities derived from the final excess counts and their flux are affected by a limited resolution. This spread in energy is caused by both systematical uncertainties, which originate by the finite resolution and efficiency of the experiment's various components, and by the statistical uncertainties arising from the analysis.

Some of the most revealing information about astrophysical sources comes from their spectra: a binned histogram showing the distribution of events as a function of some observable quantity, usually energy. Such spectra will be smeared and distorted especially by those effects which are related to the instrument response to the input data.

An important weakness of experiments aimed at measuring particle energies is the distinction between *true* energy and *estimated* energy. Whereas the former is defined by the - assumed - "ground truth" from MC simulations, the latter is derived in ways that depend on each particular analysis: it is not obvious that both of them will distribute the same events in the same differential intervals - the bins. In particular this clash emerges directly when computing the differential collection area in terms of *estimated* energy counts in *true* energy bins.

This is the reason for implementing some sort of unfolding procedure to the data after estimating the flux corresponding to the distribution of the excess counts in estimated energy.

The MAGIC collaboration adopts various regularisation methods applied to the unfolding procedure, with the aim of crosschecking results. This is done also because some methods could be statistically better suited to this purpose than others. In particular, following a standard MAGIC procedure, this will use of Tikhonov [53], Bertero [54] and Schmelling [55] methods for the calculation of spectral points. The standard analysis pipeline allows us to also crosscheck the spectra - in particular the spectral parameters with their uncertainties, through the method of forward-folding Poissonian Likelihood maximisation. While the previously mentioned unfolding procedures assume that the excess events (measured in estimated energies) belong to a Gaussian distribution, the forward-folding method exploits the counts from the ON and OFF regions maximising the poissonian likelyhood in each estimated-energy bin. This allows one to estimate the spectral parameters also in case of low counts ($\lesssim 10$) - or higher energies.

3

ANALYSIS OF MAGIC DATA AT VERY HIGH ZENITH ANGLES

This chapter deals with the ongoing study and data analysis optimisation of Very Large Zenith Angles (VLZA) MAGIC observations. This work has been carried out over test data whose stability and nature are still under investigation - but current estimates are promising. In the following I will describe the main steps of the VLZA data analysis which have been implemented so far and that are currently part of what will likely become a dedicated analysis pipeline for VLZA observations with the MAGIC telescopes.

The main long-term objective of these observations is to monitor telescopes performance under these conditions and to estimate the relevant systematics. As for any other data analysis process involving novel experimental techniques, the specific goals of this work are mainly to understand how to treat data taken under such conditions and to optimise the standard analysis process commonly used for IACTs like MAGIC - specifically what are the optimising cuts.

From the early level of data quality, different types of observables (hence of cuts) are available, thus implying a non-linear approach to data reduction. The clearest and most useful quantity to understand this point is perhaps the arrival rate of stereo events registered by the standard stereo trigger [42]. In Fig.12 such quantity is shown for a test source as a function of zenith angle. From this picture it can be seen how the overall count rate decreases - in general non-linearly - as the telescopes approach the horizon. The underlying reason is easily understandable.

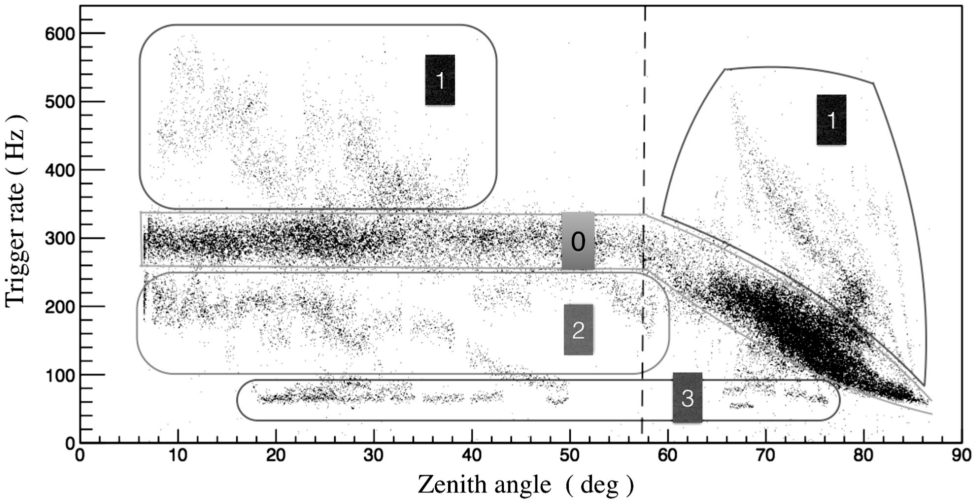

Figure 12: Example describing the behaviour of the events' stereo rate with respect to increasing values of the zenith angle. This data spans multiple days of the same source, and allows to appreciate some sub-populations of data at lower zenith angles: (0) usually regarded as good and stable, or data affected by (1) diffusion, (2) absorption or (3) different levels of NSB light.

As explained in the introduction given in 1.3, regardless of the nature of the primary particle, the side effect of the VLZA regime is to increase the absorption of the Cherenkov photons, induced especially by low-energy showers. This reflects directly in a decrease of the count rates since, as we also reported in 1.1, independently of their composition the incoming events impacting the atmosphere have a steeply decreasing energy flux. Indeed, the dominant majority of Cherenkov counts reflects low-energy events.

As the figure shows, this effect introduces a fundamental complication, which is probably the main limitation in reducing VLZA data. The constancy in both low and mid zenith observations (up to ~ 60 °) and the subsequent constant decline at VLZA is given by the action of the (Individual Pixel Rate Control (IPRC)) [42] which tries continuously to keep the rates stable in order to counter the effect given by the NSB. From ~ 60 ° on the count rate decreases faster than the system can attempt to keep it constant. As a result, at VLZA the constancy imposed by the IPRC gets modulated by the steeply declining rate, resulting in the almost constant decline shown in Fig.12. This ends up mixing, at VLZA, all the data that, at lower zenith angles, could have been separated among different observing conditions.

The following sections discuss this and other (related) issues that have arisen during the early phases of the study of VLZA effects applied to the MAGIC standard data analysis.

3.1 DATA USED FOR THIS STUDY

The data sample used in this work spans a time interval of almost two years, i.e. ~ 87 hours before quality cuts. This time refers to data spanning $70° \leqslant ZA \leqslant 80°$, even though some data were taken closer to the horizon.

As shown in Figs.13 and 14 all data are first divided into two time windows in which the telescopes hardware configurations were different, hence reflecting in different MC productions (period 1 and 2 in the following).

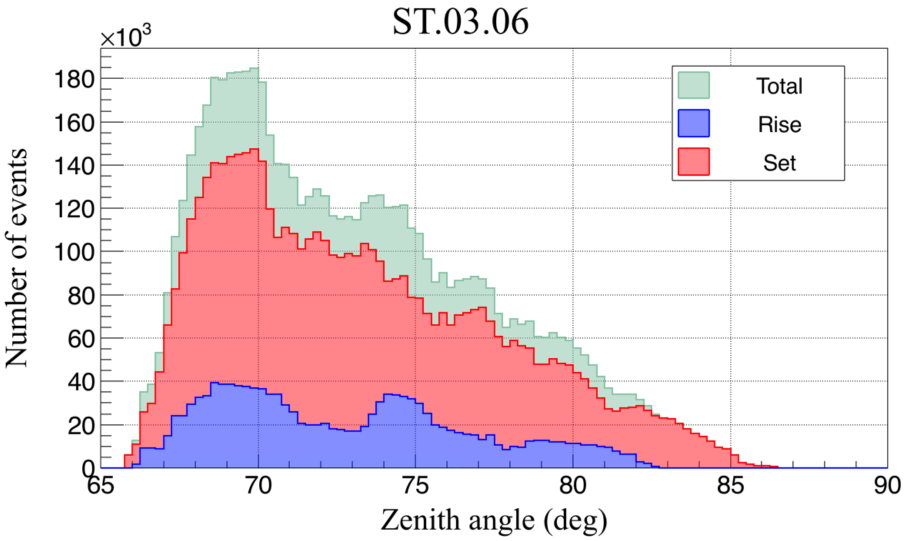

Figure 13: Distribution of zenith angle measurements for test observations at VLZA in period 1.

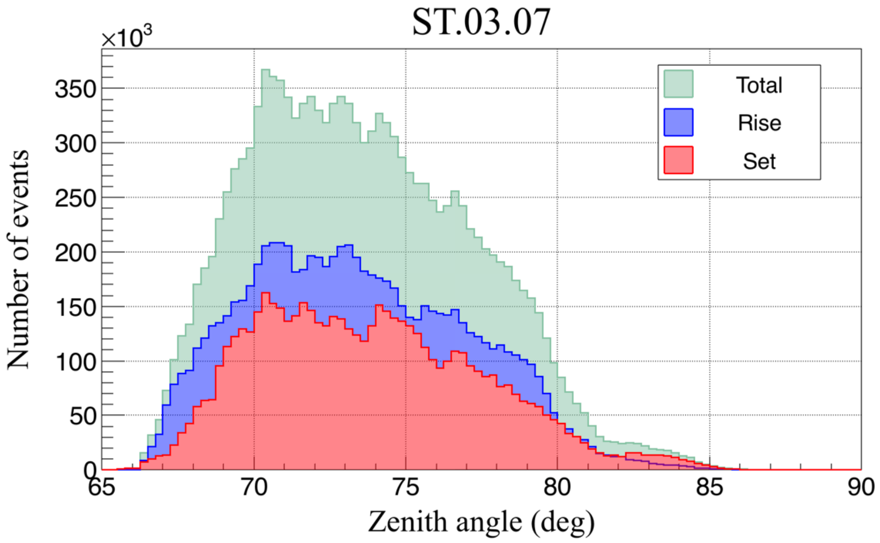

Figure 14: Distribution of zenith angle measurements for test observations at VLZA in period 2.

An important technical aspect about VLZA observations is that at very low elevations, pointing directions are constrained by the telescopes' positions at the site - which for ground-based facilities are of course fixed. Depending on the direction along the azimuth angle, some sources could have sky positions which constrain telescopes to operate in a non-optimal configuration with respect to the stereo reconstruction of the measured events (see

2): some observations may occur with both telescopes parallel to the shower direction (minimum stereo performance), some others with the telescopes perpendicular to it (maximum stereo performance). For this reason, as figures 13 and 14 show, the observations described here have been performed in two separate regimes: one in which the source was rising from the horizon with an azimuth range of ($68° \leqslant \phi \leqslant 78°$), one on which the source was setting ($282° \leqslant \phi \leqslant 293°$). These azimuth ranges represent basically extreme cases of the telescope parallel/perpendicular orientation with respect to the source, so the two datasets are to be treated separately.

This of course highlight the need that multiple MC productions are realized for each combination of time window and azimuth range - depending on individual scheduled sources, as is the case for ongoing MAGIC studies.

3.2 DATA QUALITY AT VLZA

As introduced in 1.3 and shown indirectly in Fig. 12, given the monitoring limitations of VLZA data, the standard process of data quality selection cannot be applied in straightforward way.

Depending on the sample, some considerations can be made from combining different cuts, in order to ease the difficulties from the point of view of the rates. This can help one to judge if rate cuts are really necessary after all, since generally they are not used for offline data-quality assessments related to atmospheric effects. This is because at lower ZA, more reliable and - most importantly - independent measurements are available during both observations and later treatment of data.

3.2.1 LIDAR

At lower ZA the main instrument at hand is the LIDAR (2.1.2), which in principle is available also for VLZA observations. The information coming from such instrument, coupled with other observables registered by the main subsystems, is usually sufficient to estimate the quality of the data. The LIDAR can also provide an estimate of the transmission value for the correction that will be later applied to the data (2.2.1).

Its action is however limited by its current scale and power, which translates into a maximum shooting distance - currently adopted in the analysis up to 12 km. This makes VLZA measurements not reliable enough, because the actual maximum shower distance is $\sim$ 10 times larger (see 1.3).

In particular, in absence of absorbing material within the quoted range, possible high measured transmission values are unable to estimate the *integral* absorption of the shower. In fact, the obtained measurement would account for an only $\lesssim$10% correction of the estimated energy of the events in that time interval.

Being VLZA observations uncharted territory for IACTs, the transmission estimates described in 2.1.2 cannot be done precisely in this case. So I chose a more conservative solution. The LIDAR transmission-quality reference values used in this work refer to the minimum "safe" transmission level used for lower zenith analyses, i.e. 70%, but measured at a distance of 12km (the current official maximum distance for such measurements within the MAGIC collaboration) instead of 9km (corresponding to the height scale in a typical molecular density profile of the sky above the MAGIC telescopes). Even though 12 km are not enough for properly correcting the estimated energy of the showers at VLZA, this conservative cut allows to eliminate at an early stage those showers which have been absorbed (at least) near the telescopes (and possibly even before).

A sufficiently powerful LIDAR would be optimal for VLZA observations, but may be difficult to accomodate with the regulations at La Palma (e.g. because of maximum power and a shooting pointing close to the horizon).

3.2.2 Pyrometer

As explained in 2.1.3, the MAGIC Pyrometer is an alternative instrument which can be used to assess the amount of material along the line of sight (LOS) by means of mid-infrared thermal photons. Since this radiation is emitted by the material itself, the contribution to the effective temperature is at least directly dependent on the amount of matter.

In the real case scenario, any theoretical or semi-empirical model of the atmosphere cannot pretend to give a consistent picture of it without considering its chemical composition. The main components which contribute to this measurement are water vapour, dust, and a mixture of gaseous species. Within the latter, ozone, methane, and basic molecular species (mainly carbon dioxide, oxygen, and nitrogen), contribute at different wavelengths and with different spectral intensities.

What makes this kind of measurements definitively more complex for IACTs, is that in order to estimate atmospheric absorption along the shower development, this measurement is mostly useful if it is differential [56]. Some tentative studies have been already carried out within the MAGIC collaboration [57], mainly aimed at understanding the systematics associated with the measurement itself.

What seems to a limit to this approach is that, in order to transform an integral measurement into a differential one, a detailed model of the medium needs to be assumed which maps the different emissions along the line of sight.

Without such needed detail, the overall observable effect at VLZAs causes the thermal radiation towards the ground to increase as in Fig.15, because of both the increasing thickness of the material along the line of sight and the proximity of the ground in the Field of View (FOV) of the pyrometer.

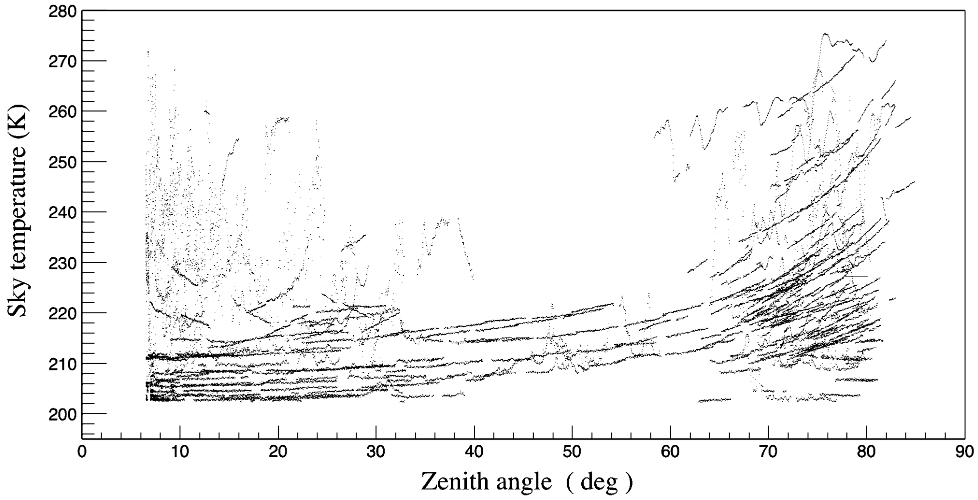

55

Figure 15: Relation between the mid-infrared sky temperature measured with the MAGIC Pyrometer and zenith angle. Observing towards the ground the material in front of the telescopes gets systematically warmer. Temporary modulations by obstacles along the LOS are visible in many observations. Each continuous line represents a single data run.

In fact, even at lower zenith angles, usual current cuts on Pyrometer-related quantites are rather phenomenological. Up to now, especially while taking VLZA data, it is not clear if there is a sufficiently precise way to decide accurate cut values from this instrument during the analysis. Also, as reported in 2.1.3, the measurements provided by the pyrometer are affected by a non-neglibile, non-trivial miscalibration.

For these reasons, after a first phase during which I realised the extent of such limitations, I decided not to use this instrument in the data quality at VLZA angles.

3.2.3 Starguider

Given the limited power of the LIDAR system and the decision not to make use of the MAGIC pyrometer, the next best candidate for data-quality selection for VLZA data was the *Starguider* system (2.1.4). In principle, this cut consists in selecting the data which features the higher number of stars, thus reflecting integrally a clearer sky.

Since the distribution of stars is not uniform in the sky, I considered each wobble position (2.2.4) of each subsample separately. I then recombined the filtered events for each wobble, each telescope, and each subsample, merging sequentially the excluded time slices.

An important point is that since these studies have been carried out on stereo data, each cut from data quality (2.2.1) is applied over both telescopes event-wise. In the case of the cut from the *Starguider* instruments this is especially important.

In principle, the distribution of the number of correlated (i.e., *recognised*, cfr 2.1.4) stars could be different for the two cameras. This can happen due to temporary hardware differences (like dead pixels in one of the *Starguider* cameras) or because an absorber within the atmosphere (a cloud or a dust front) is sliding towards the site, appearing initially along the line of sight of just one of the two telescopes. At the same time, though, being the atmosphere the same for the two instruments, the recorded data are correlated between the paired distributions.

Taking these informations into account, I decided to apply the *Starguider* cut in a conservative way, choosing it from the leftmost distribution (i.e. featuring the lower number of recognised stars), regardless of the telescope (see Fig.16). This is particularly important in case the two distributions present a bias. This conservative choice allows always to select the main bulk of data correspondent to the highest number of stars recognised by each camera. At the same time, since the atmosphere is unique and the events are stereoscopic, the two distributions (in particular their shape) are correlated. This means that any event in the tail of the worst distribution is an event that gets already cut from the best distribution (see 17).

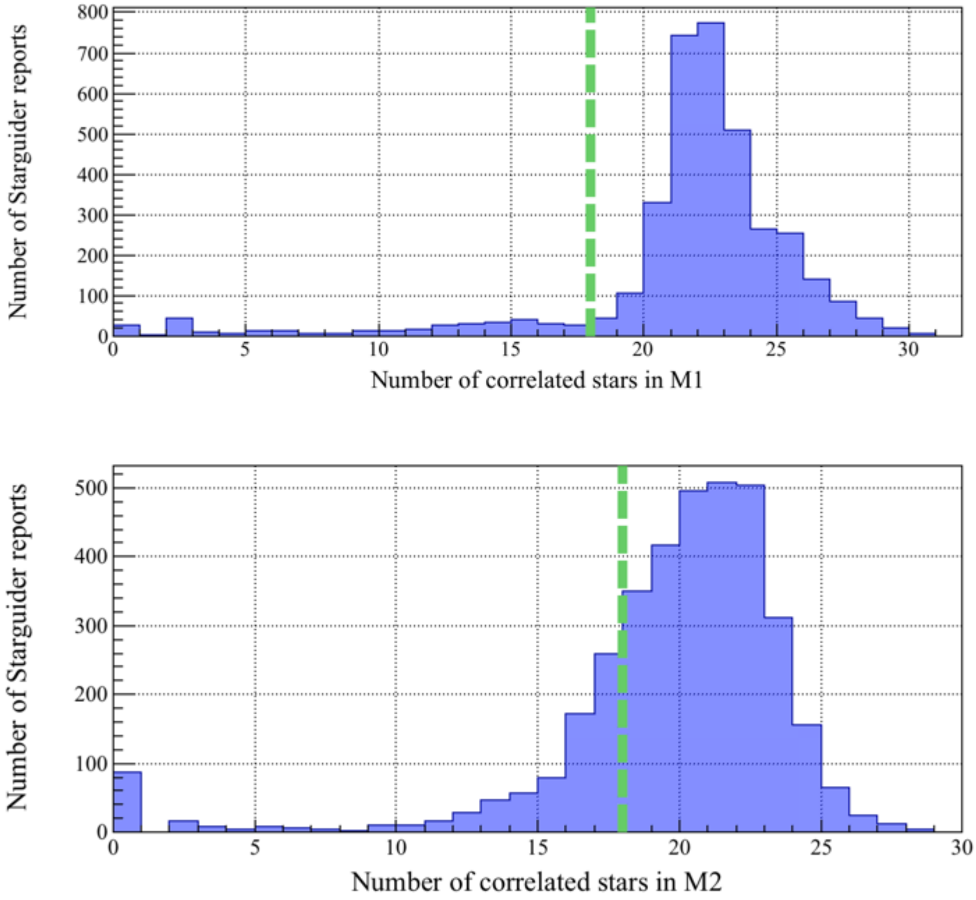

Figure 16: Example showing the distributions of the number of recognised stars from each *Starguider* camera in a given wobble. In this case the distributions are similar, the cut is easy to decide.

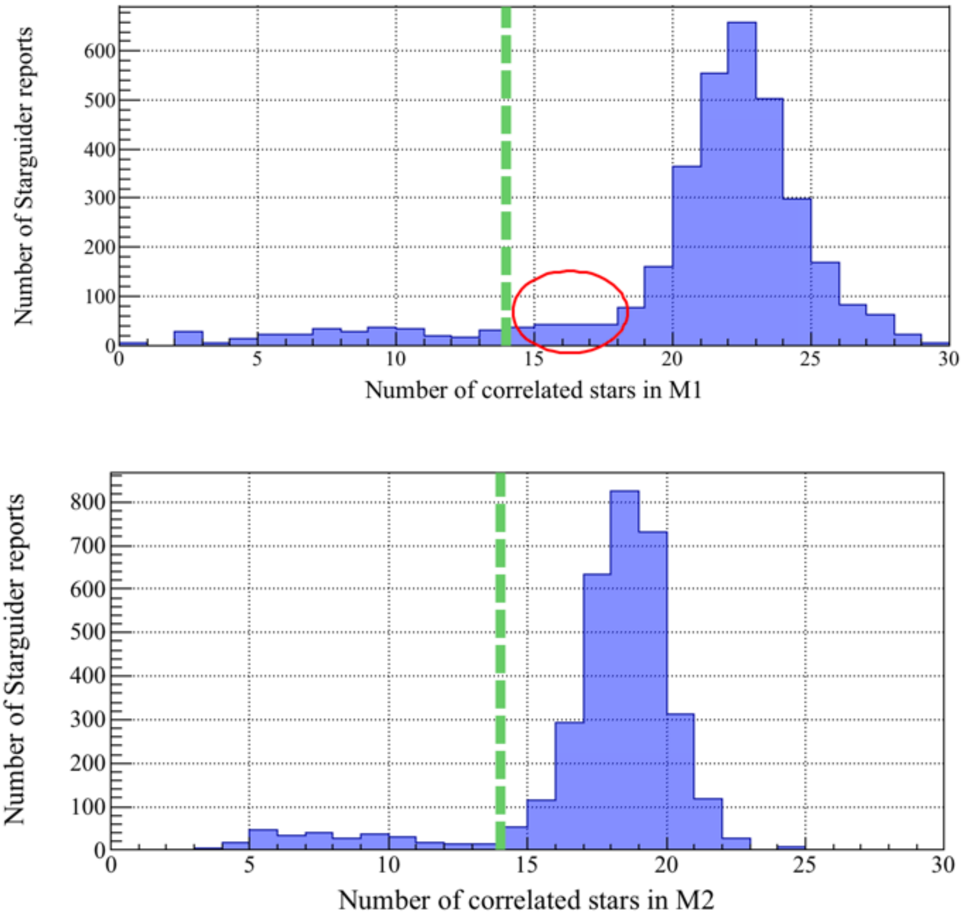

Figure 17: Example showing the distributions of number of recognised stars from each *Starguider* camera in a fixed wobble. In this case the distributions have a similar peak but different tails: the cut is chosen in a conservative way from the leftmost distribution. The red circle shows the data excluded because of correlation, together with all data lying at the left of the green dashed line.

A better way to look at the correlation between the telescope-wise number of correlated stars is presented in Fig.18, which refers to the same data used to produce Fig.17

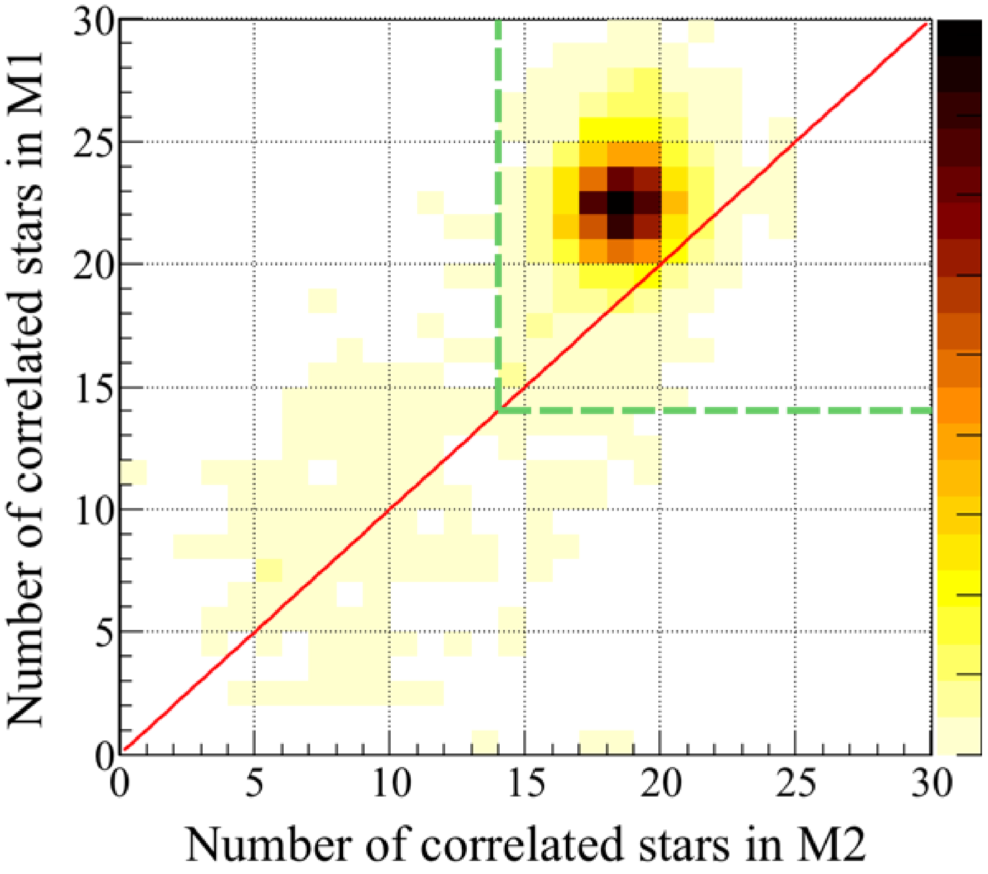

Figure 18: Example showing the correlation between the number of stars recognised by the two telescopes. The green dashed line represents the event-wise stereo cut above which clear-sky data is kept. The red continuous line represents the case of perfect correlation between the two cameras.

After deciding a *Starguider* cut, it can be useful to see how this cut affects the distribution of stereo rates as a function of zenith angle. Remember that this is the quantity that better represents VLZA data, especially from the on-site operators point of view (see Fig.12).

As an example I show this point as applied to one of the (apparently) less stable subsamples, in order to magnify the effect for clarity sake.

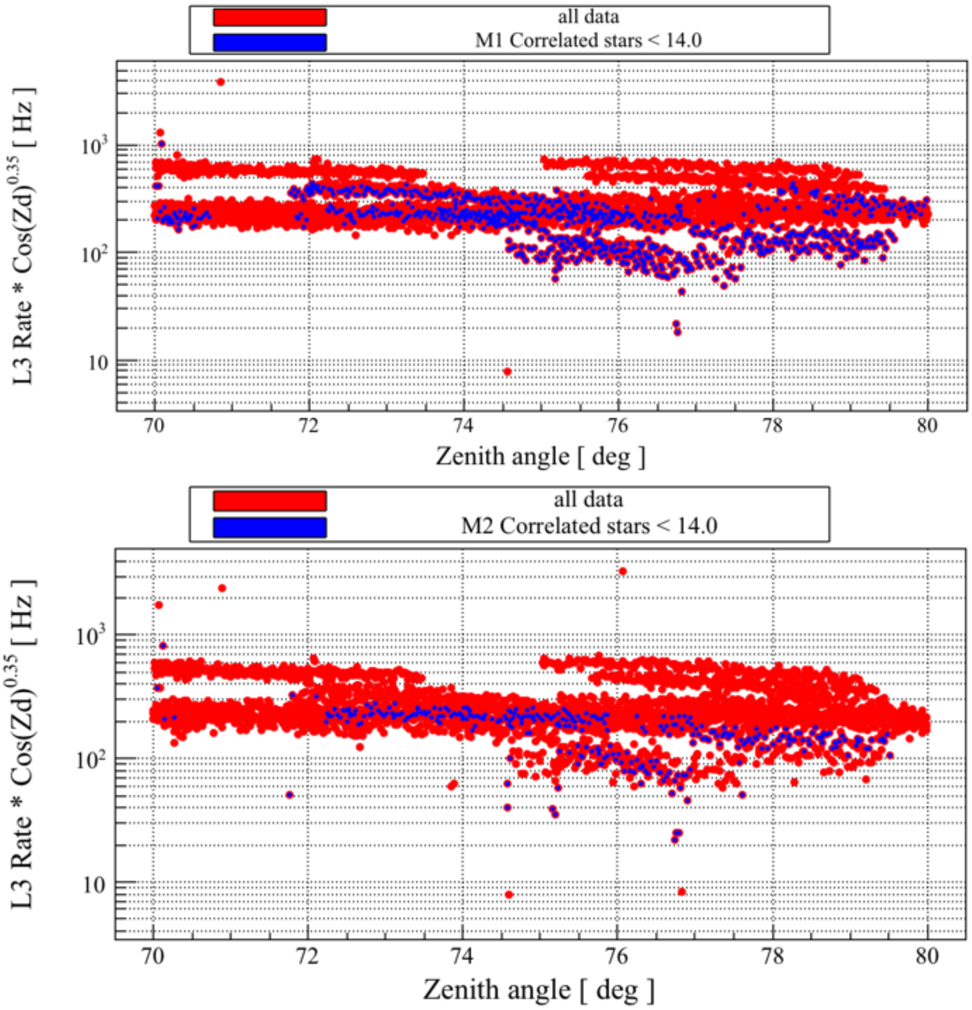

Figure 19: Example showing the effect of the stereo cut on the number of recognised stars over the zenith-angle evolution of the rate of stereo events, which reported as a function of cos(Zd) in order to flatten it for better handling. Each quantity in the plots is telescope-wise.

As it can be seen from Fig.19, in principle the effect can be rather different depending on which telescope data is used. As it is usual in science, when an operation shows an effect bigger than predicted it usually brings more information along with the unexpected result. This shows that the more likely outcome of the resulting cut is better described by the upper plot, which refers to MAGIC-I data, that indeed lost more events due to the correlated data contained in the low-end tail of the distribution of recognised stars in the *Starguider-1* instrument (Fig.17).

We can realise how the data taken at $74° \lesssim \mathrm{ZA} \lesssim 78°$ is actually almost completely cut by the chosen cut in the M1 sample (upper panel of Fig.19). As a result, the stereo cut will eliminate the same events seen by M2, even if in for the *Starguider-2* instrument those events had more stars than M1. That group of points illustrates the example particularly well, because their lower rate with respect to the whole bulk of observations reflects a degradation in the quality of data. At this point we don't know yet what could be the reason for this degradation, but we can trust the cut as highlighting the stereo data that are, most likely, reflecting some sort of absorption.

Note that Fig.19 has some features which at first sight could appear worrying:

- some groups of data have a *higher* rate than the bulk,
- some spurious points lie out of the main population because of too high or too low rates.

These points are treated consistently in the procedure I will be describing in this section, which may become a standard procedure in VLZA data analysis.

3.2.4 DC levels

Since VLZA observations are a novel subject for MAGIC (and for IACTs in general), at the time of the first VLZA observational proposals and of this work there has not been a dedicated study on possible Moon analysis optimisations.

The performance of the MAGIC telescopes have been studied under moonlight conditions and published in [58]. As shown in Fig.9 of such reference, data for ZA$\lesssim$50° can be analysed with standard cleaning and standard MC simulations. The obtained spectrum is consistent (within 10%) with the one obtained in dark conditions, whereas for higher NSBs the difference naturally increases.

This makes it clear that whether or not the standard analysis can be used at VLZAs depends on the final systematic errors that future investigators will be willing to accept for such analysis. The corresponding scatter in the non-dark spectrum at VLZA will have to be combined with the remaining systematics inherent to VLZA observations (pointing accuracy, energy resolution and bias, to name a few) which are currently under investigation.

For all these reasons the approach I decided to use for this work is a conservative DC cut, based on the standard dark analysis at lower zenith angles. For MAGIC, the current adimensional unit of NSB corresponds to a DC level of $\sim 1.1\mu A$.

Taking the direct current measured by MAGIC-1 [58] as a reference value, the DC distributions for the data used in this work are displayed in Figs.20-23. The figures reflect the 4 subsamples in which the data have been divided (two periods by two configurations of the source's position in the sky).

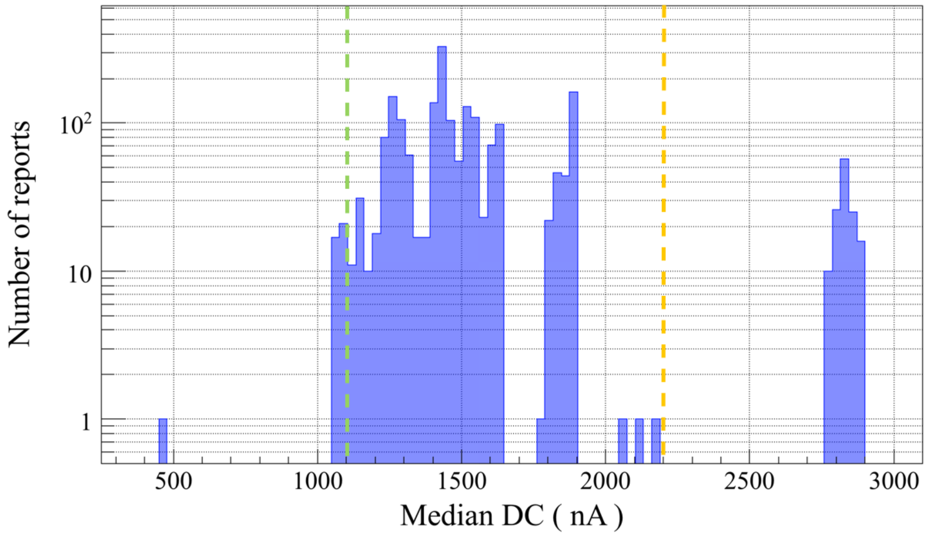

Figure 20: Direct current distribution as measured by MAGIC-I of ST0306 Rise data between 70 and 80 degrees zenith. Green and orange dashed lines represent the NSB level 1 and 2 respectively.

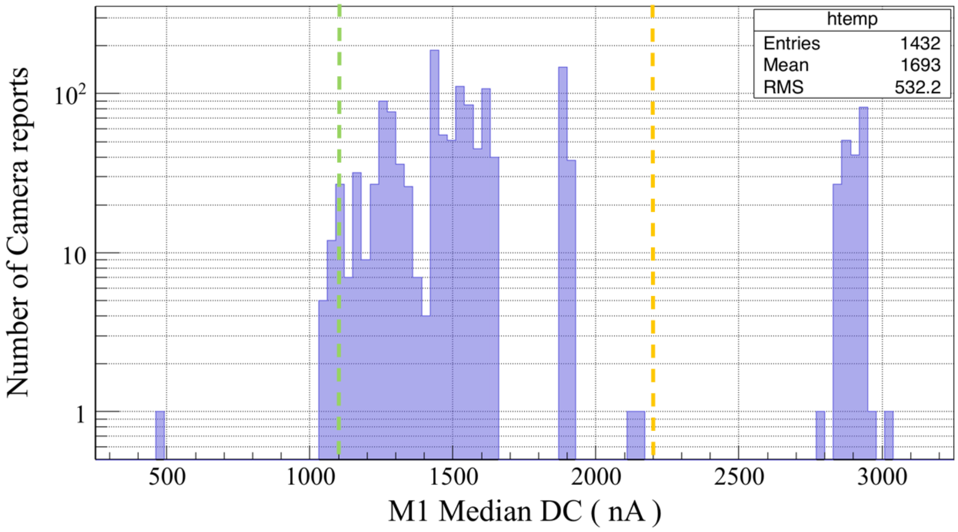

Figure 21: Direct current distribution as measured by MAGIC-I of ST0306 Set data between 70 and 80 degrees zenith. Green and orange dashed lines represent the NSB level 1 and 2 respectively.

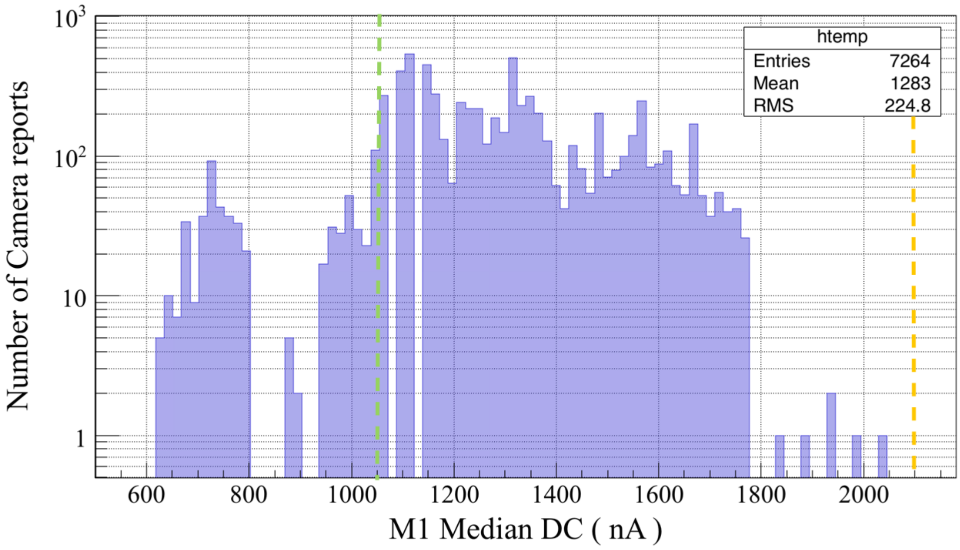

Figure 22: Direct current distribution as measured by MAGIC-I of ST0307 Rise data between 70 and 80 degrees zenith. Green and orange dashed lines represent the NSB level 1 and 2 respectively.

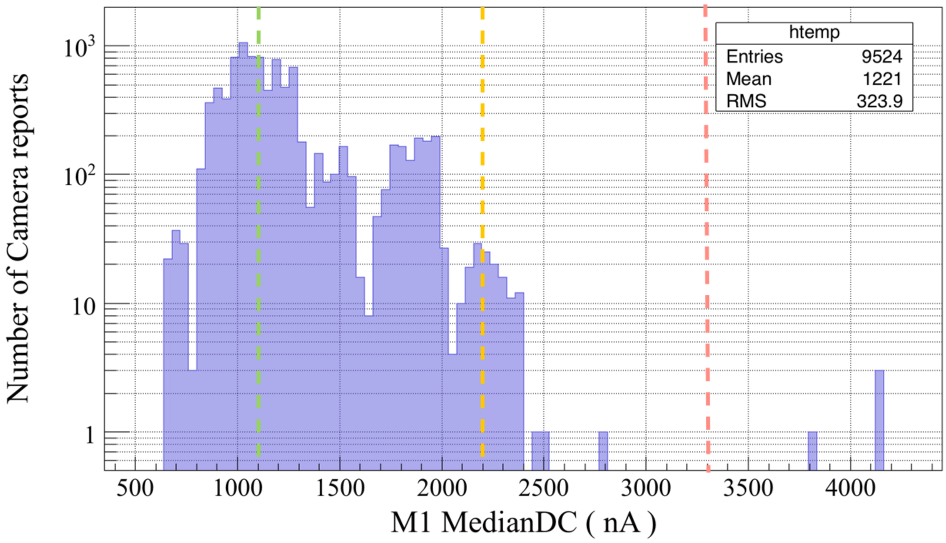

Figure 23: Direct current distribution as measured by MAGIC-I of ST0307 Set data between 70 and 80 degrees zenith. Green, orange, and red dashed lines represent the NSB level 1, 2, and 3 respectively.

As it can be seen, most of the data have NSB~2, with a minor fraction over this level that represents a dataset a-priori incompatible with dark analyses.

Even if the amount of such data was negligible, I decided to apply a limiting cut of $\lesssim$10% surviving pedestals after image cleaning applied on-line to the data before stereo reconstruction [37]. As a result, no data with NSB~3 was excluded from this analysis.

Instead, all data with NSB>3 was excluded *a priori*, given the need in such cases of tuned MC data which were not available at the time of this work and which would likely require a totally different dedicated analysis.

The 1D distribution of the events' DC values is useful in classifying and discriminating bulks of data which will be selected for the analysis - e.g., following the prescriptions defined in [58].

For a VLZA analysis this is not sufficient, though. Given the difficulty in disentangling the different populations in the VLZA data as shown in Fig.12, in this data quality procedure I use the DC levels *together* with the *Starguider* input (from section 3.2.3).

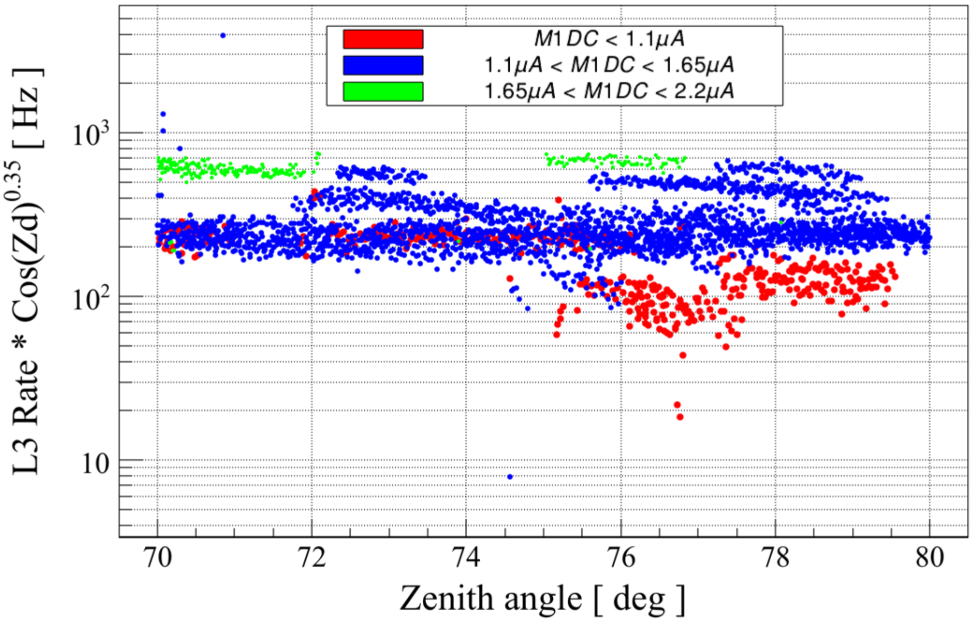

Figure 24: Example showing the disentanglement of VLZA data population depending on the registered DC levels.

Fig.24 shows an important point.

Even if compatible with a dark-level analysis when taken in its entirety, the data contained in this subsample was taken under slightly different NSB conditions, which I divided as shown in the legend: the red population represents perfect darkness (NSB$\lesssim$1), while blue and green divide the *dim* level of light (1$\lesssim$NSB$\lesssim$2) in two equally spaced intervals.

In some subsamples the range spanned by the data could be bigger: therefore, in order to apply this procedure, more divisions are required in order to appreciate any differences among different populations of data. We can now appreciate that the group of data with 74°ZA78° and with a rate 50Hz $\sim$ 200Hz belongs to the same population (coloured red in the figure) clustered between 200 and 300 Hz, but its rate is clearly damped.

A comparison with Fig.19 can help solving the doubt: the reason why this dataset has a lower rate than expected is, most likely, because of absorption from a material in the FoV - e.g., clouds - that is also responsible for the lower number of recognised stars for the same dataset.

Even more important, we can say something about the rest of data, i.e., the data that appeared worrying because of the (sometimes big) rate differences.

By the same reasons fthat led us to question the lower-rate data (because, in the case of LIDAR monitoring the latter usually reflects a weather-related lower transmission), the higher-rate dataset could trigger the same questions when looking at it for the first time. This is because Cherenkov photons can not only be absorbed by, e.g., clouds, but they can also be *diffused* by the same material - especially for higher NSB levels (not necessarily only in Moon time).

In the example shown by the data of Fig.24, we can see that even if the higher level of dim DC makes the green data look different from the rest, in reality not only are they still compatible with the dark analysis, but the Starguider cut clearly shows that there is no absorption affecting those data.

The interpretation of the effects of these applied cuts is that for such data the shower content present in those time intervals does not get lost to absorption, but there is just more noise (mostly so at low energies) because of the higher NSB.

At last, we are left clearly unphysical readings characterized by jumps and falls in rate that are definitely outside the usual registered ranges even at lower ZA.

3.2.5 Stereo rate of events

From the combination of the observables described in the previous paragraphs, if a cut in stereo-event rate has to be done, it can be finally decided at this point. This is important in order to account for all the purely artificial sources of noise - such as car flashes and discriminator threshold changes. These events represent impulsive variations during data taking and are not common or continuous enough to cause complete removal of a run from the analysis (cfr 2.2.1).

Generally, every major sharp or sudden change in the rates during the decreasing behaviour with respect to the ZA evolution (see Fig.12) has been selected for cut.

An example is given in Fig.25 which uses the same data as in Fig.19. Note how the lower cut (green dashed lines in the figure) seems especially strict, as it apparently discards good data: in reality, from the upper panel of Fig.19 we can see that the cluster of points in the second half of the zenith range is already eliminated because MAGIC-I doesn't see enough stars. Cases such as this show how rate cuts can be effectively used to eliminate bad data at VLZA quite close to the central population, were the mixing is higher - provided that a study of secondary clusters was previously made with the help of *Starguider* data and DC levels.

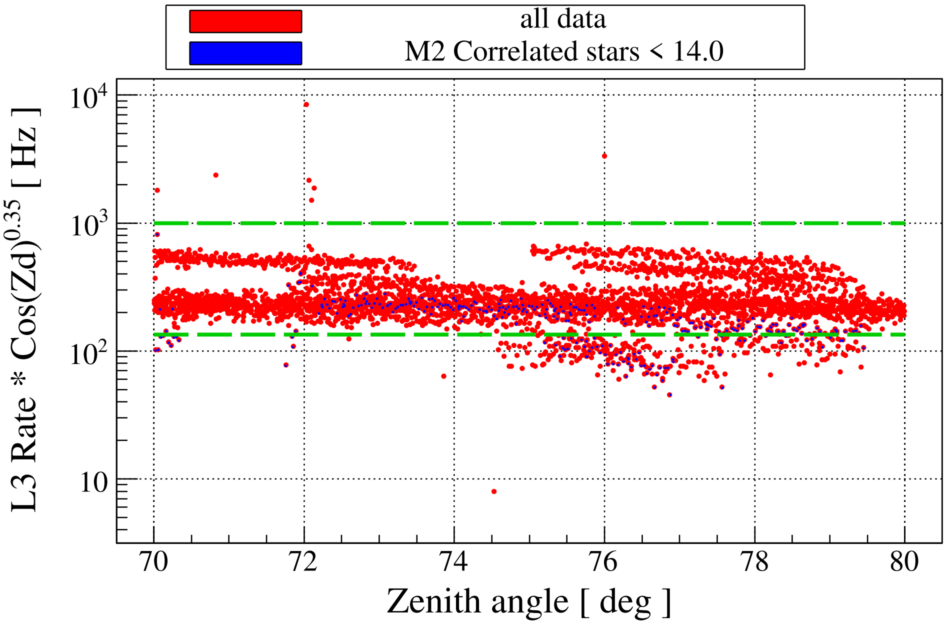

Figure 25: Example showing the cut on stereo rate applied to VLZA data.

3.2.6 Summary of data quality

Taking into account all the above described cuts, in Fig.26 I show a summary of the VLZA data quality procedure applied to data which belong to a single wobble position. As mentioned at the beginning I apply this procedure to each wobble separately, each subsample and each MC period for a total of 8 data quality applications. The corresponding amount of data loss in term of observation time oscillates between 50% and 65% of the total initial amount, i.e. ~ 50 hours. Naturally these values are only indicative and highly dependent on a specific source and observational conditions, given the low expected flux for VLZA data.

3.3 OPTIMISATION OF THE STANDARD RANDOM FOREST

3.3.1 Trigger efficiency at VLZA

As the ZA increases, the performance dependence on the azimuth progressively becomes non-negligible. This is mainly due to the varying stereo power and geomagnetic field orientation.

The approach followed here is similar to what is usually carried out in analyses where data are taken at ZA $\gtrsim 35°$. The method relies on using a quantity related to the collection area (2.2.4, equation (5)), to estimate the efficiency of γ-ray detection depending of MAGIC's current azimuth direction.

At VLZA this concept is critical, because of the properties of the showers at such low elevations (1.3). It is fundamental to study how the MC data

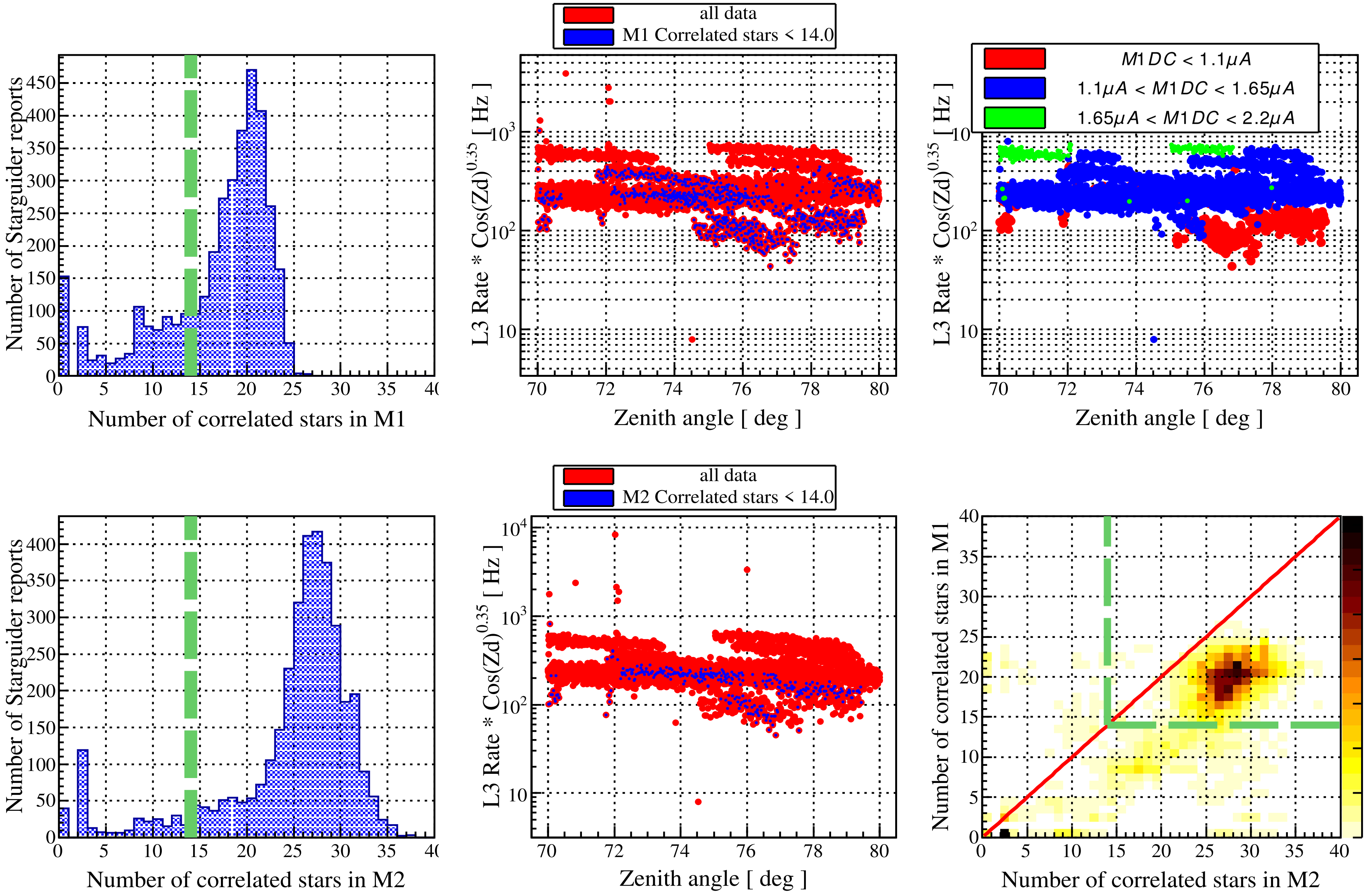

Figure 26: Summary of the observables and their treatment as applied to the data quality of MAGIC data at VLZA.

behaves at VLZA, because of the novel physical conditions that we aim to investigate.

The collection area in this case does not contain high-level cuts, but just the combination between the external conditions of the simulations (i.e. the atmospheric model, the properties of the observatory, ecc...) and the properties of the instrument (reflective surface, performance of the electronics, ecc...). In this case the main parameter is the trigger efficiency, which can be described by (5) before the high-level analysis.

In principle this operation can be repeated at different levels of the analysis in order to ensure stability or to crosscheck the random forest.

Being dependent on the instrumental conditions, MC data has to be produced for each period in which the hardware conditions are considered to be stable (taking into account electronics, as well as the status of the mirrors and the structure of the telescopes).

Figures 27-30 show the detection efficiency for each of the two periods in which data have been taken, each in turn split into two equal ZA ranges (5 ° each) in order to minimise any fluctuation in that direction. The magnitude of fluctuations increases from the first to the second ZA slice because the number of events is systematically lower in the second case, see Fig.13 and 14.

Three different energy scales (1, 10 and 80 TeV) have been chosen in order to investigate the smeared effect over a bigger range than the one interesting for just Galactic Pevatron studies (> 100 TeV), in particular over 3 decades in energy. This is important when comparing, for a given source, VLZA SEDs with other SEDs measured at lower energies and lower ZA.

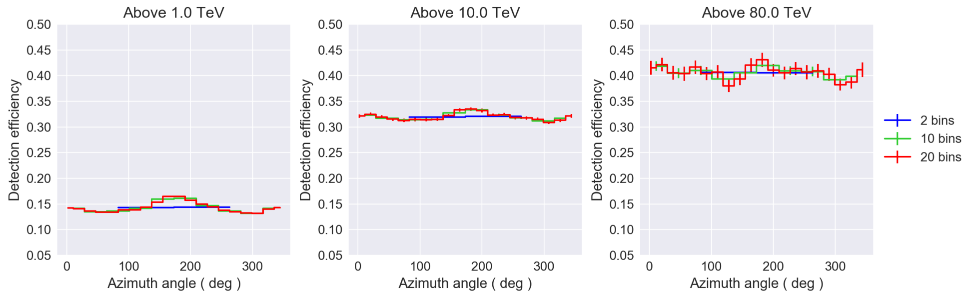

Figure 27: Azimuth dependence for period 1: $70° \leqslant \text{ZA} \leqslant 75°$.

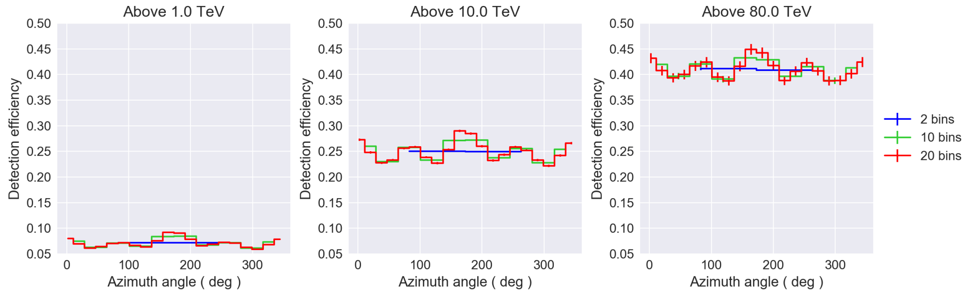

Figure 28: Azimuth dependence for period 1: $75° \leqslant \text{ZA} \leqslant 80°$.

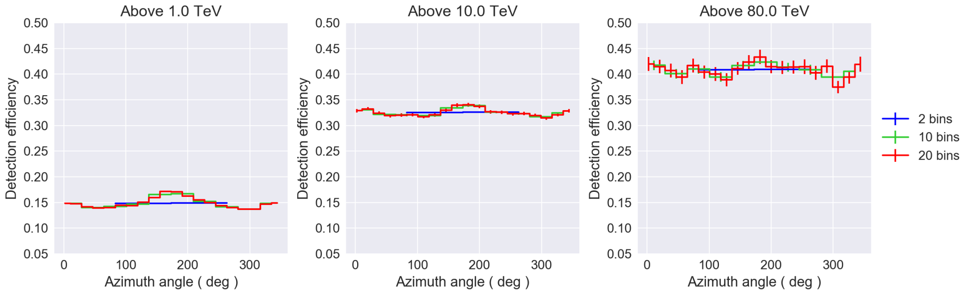

Figure 29: Azimuth dependence for period 2: 70° ⩽ ZA ⩽ 75°.

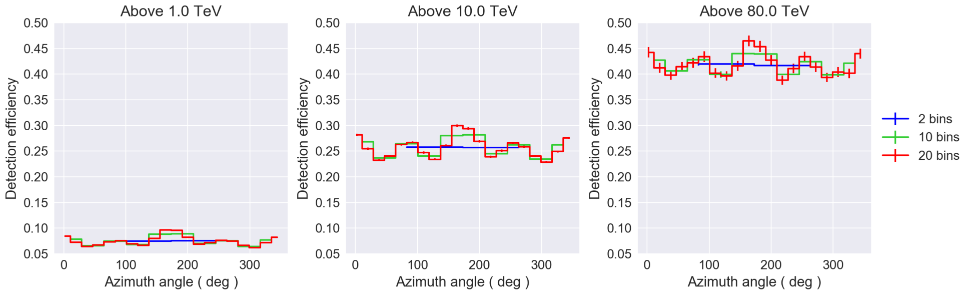

Figure 30: Azimuth dependence for period 2: 75° ⩽ ZA ⩽ 80°.

Error bars rely on the binomial approximation valid for correlated quantities (i.e., number of simulated events and number of events surviving the simulation).

The results reported here show that the azimuth dependence of the detection efficiency for 70° ⩽ ZA ⩽ 80° seems to remain the same over different periods and narrow ZA ranges. In particular fluctuations stay confined to $\lesssim$5% in all the binnings considered (however, the case of 2 bins the binning is not sufficient to appreciate such fluctuations within the error bars).

Due to the fixed number of events per simulation, it is usually not good to use too higher binning in order not to lower the statistics, especially when applying successive cuts. That's why binning values > 10, for which fluctuations show no sudden changes, can be ignored in favour of lower values which still show some kind of variation of the fluctuations along the range.

The final number of azimuthal bins, with particular reference to the energies > 80 TeV, is set to 7 for all the subsamples, in order to ensure an angular variability within $\sim 10\%$ (Fig.31).

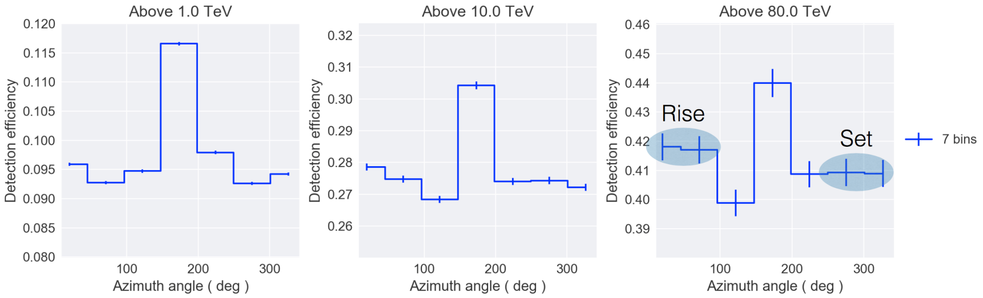

Figure 31: Choice of azimuth binning for VLZA data used in this study. Azimuth ranges correspondent to "Rise" and "Set" direction of the source are highlighted with shadowed areas.

It is worth noticing that, with this choice, at the highest energies the azimuth variability is negligible, but at lower energies, owing to the higher statistics, the error bars are smaller and we can appreciate an effect over the entire angular range.

3.3.2 Learning curves

Due to the reasons explained in 3.3.1, the entire data sample had to be divided in 4 smaller sets. A limitation of this study is that 3 of such data periods did not have dedicated OFF observations scheduled at such high ZA. This implied that, for those 3 subsamples, part of the Crab data had to be used as OFF training data (see 2.2.2).

In normal cases using Crab data as OFF training data is considered bad practice, because of the risk of biasing the results. However, for this analysis this was deemed acceptable because the rate of the observed data at VLZA (see Fig.32 and 33) allows one to say that the number of γ rays from a general source is negligible with respect to the known rate of cosmic rays at the relevant energies ($>$ 100 TeV), i.e., $\sim 1\gamma$ ray every 10^3 cosmic ray counts.

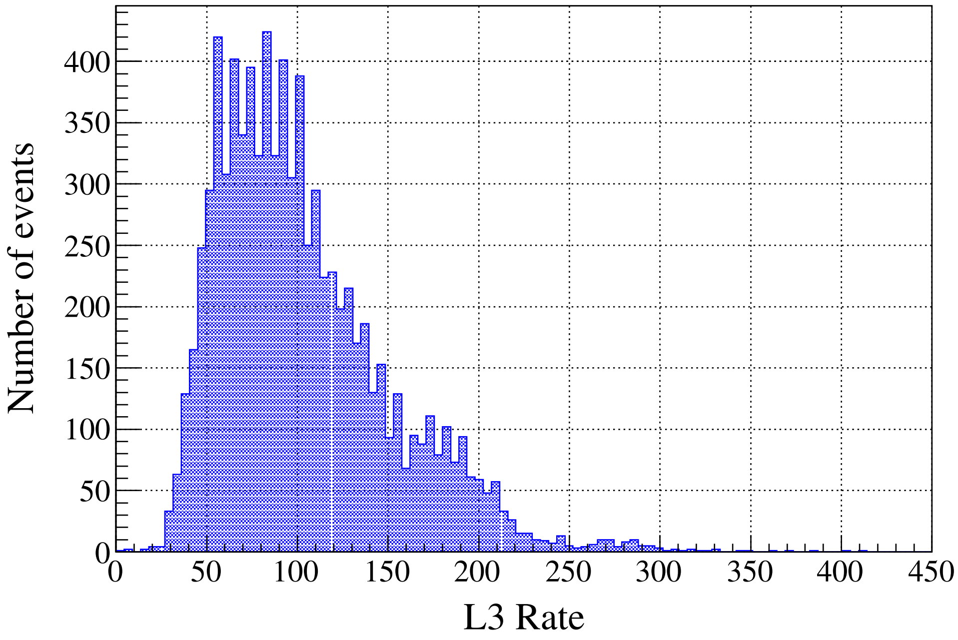

Figure 32: Distribution of stereo level rate of data belonging to period 1.

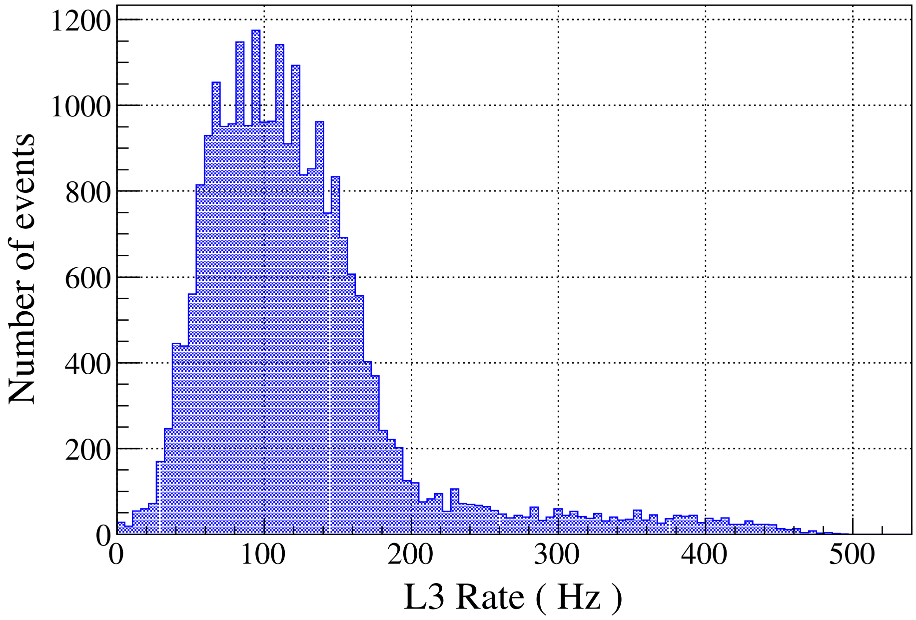

Figure 33: Distribution of stereo level rate of data belonging to period 2.

However, even if using Crab data as OFF training data is acceptable in this case, a drawback is that using part of the ON data to train the Random Forest (2.2.2) means that less data will be available for the final scientific results (2.2.4). This is especially true if, given the observational constraints at VLZA along the azimuth direction, some sources are observed for short times, resulting in less data, that have to be treated separately. For this reason I studied how to optimise the observational time by learning how much OFF data was really needed.

One way to solve this problem is to assess the efficiency of the RF given the MC data and the source's data, in order to use as few training events as possible without harming the RF's power to recognise gammas.

The method chosen for this work is based on the machine learning concept of *learning curve*, which aims at evaluating the ability of any general machine learning algorithm to recognise both the training and the test events. The parameter which quantifies this concept is called *score*: being an efficiency parameter its values are comprised between 0 and 1. In principle there can be different definitions of a score: in this work I apply the definition,

$$\mathrm{score} = \frac{\sum_{i=1}^{N}(\text{is }\gamma) + \sum_{j=1}^{K}(\text{is background})}{N+K}, \tag{6}$$

i.e., the ratio between the number of times the RF correctly identified a γ out of N MC events and a hadron out of K OFF events over the total number of events between the correspondent test samples. In practice it is a form of RF efficiency.

The process is applied to *both* training data and test data: that is, the RF trained with the OFF and MC data is not only applied to the remaining test sample data, but also to the very training data. In this way, for every amount of training data, we will always have a reference value represented by the training learning curve, against which we compare the same curve applied to the test sample, which the RF doesn't know about.

In an ideal case, the score over the training ratio should always be 1: the RF has been trained with those data, so it should recognise every event correctly. Instead, in the test case the RF is applied to unknown data, and the score should increase with the amount of training data used - i.e., the RF becomes more powerful - and then it should asymptotically reach the training sample efficiency. The test sample will never reach the training one in an ideal case (Fig.34).

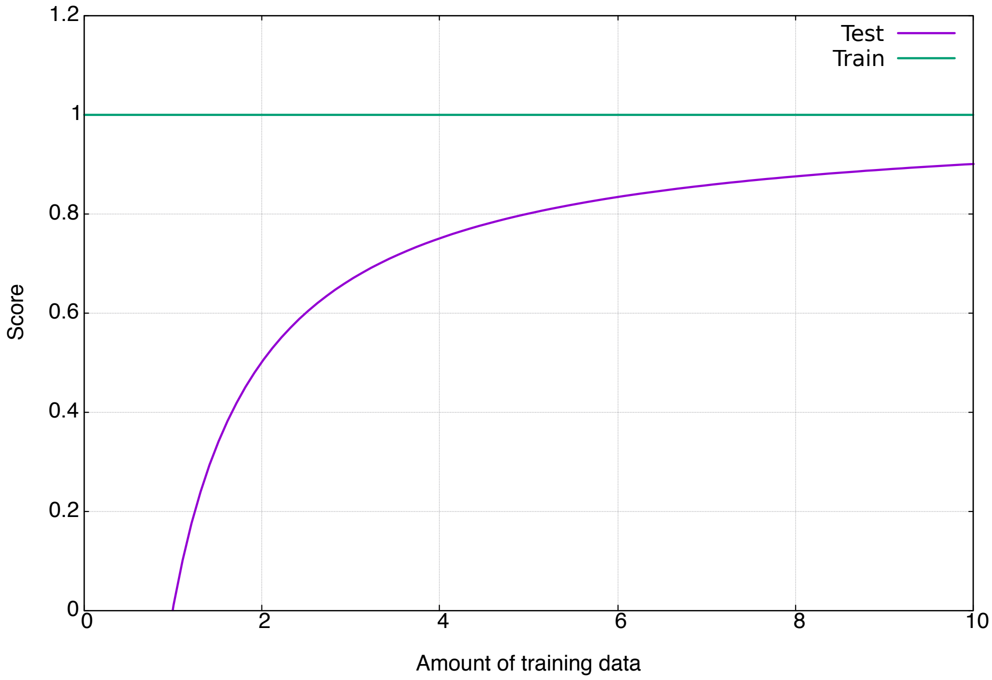

Figure 34: Ideal case of a learning curve evaluation.

The chosen discriminator for the computation of the score is a *hadronness* (see 2.2.2) value of 0.5. This is a somewhat loose value and in principle it can be modified checking what is the effective value at which the final analysis products are produced (either detection studies or flux estimation). Then, a possible - albeit time expensive - procedure could be to update the discrimination parameter with values which prove to boost the analysis' performance for the true energy events in the MC data.

The process applied here for a single such iteration is the following:

- from the N runs generating the i^{th} subsample, select M runs randomly to be used for training; the remaining $N - M$ runs will be used for testing;
- create the RF;
- apply the RF first to the same training sample from which it was created: in the ideal case this would correspond to the green line in Fig.34;
- apply the RF to the test sample just as it would be normally done for any analysis;
- calculate both scores, given (e.g.) by Equation (6);
- increase N and repeat the process until $M = N - 1$ (at least 1 run is needed in the test sample).

If parallelised on j simulations, each random choice of M data runs would have different scores, allowing mean and standard deviation to be calculated for each step. Even without knowing the result, it is clear that as more data are used for training, the RF should become more and more powerful in dealing with the test sample, until the corresponding learning curve will eventually reach the training curve.

As more data are being supplied, the RF becomes overpowered and the process doesn’t show any obvious improvement: this is the point when the chosen M runs represent an optimal choice between creating a weak RF and wasting data on its training. Figures 35 and 36 show an example over the 2 smallest subsamples.

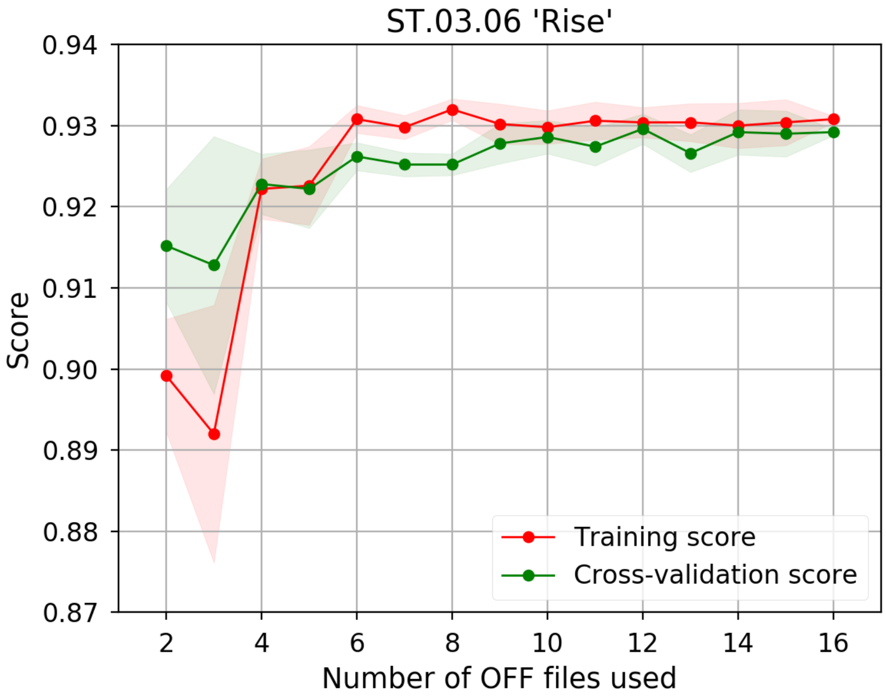

Figure 35: Learning curve for period 1 sample "Rise".

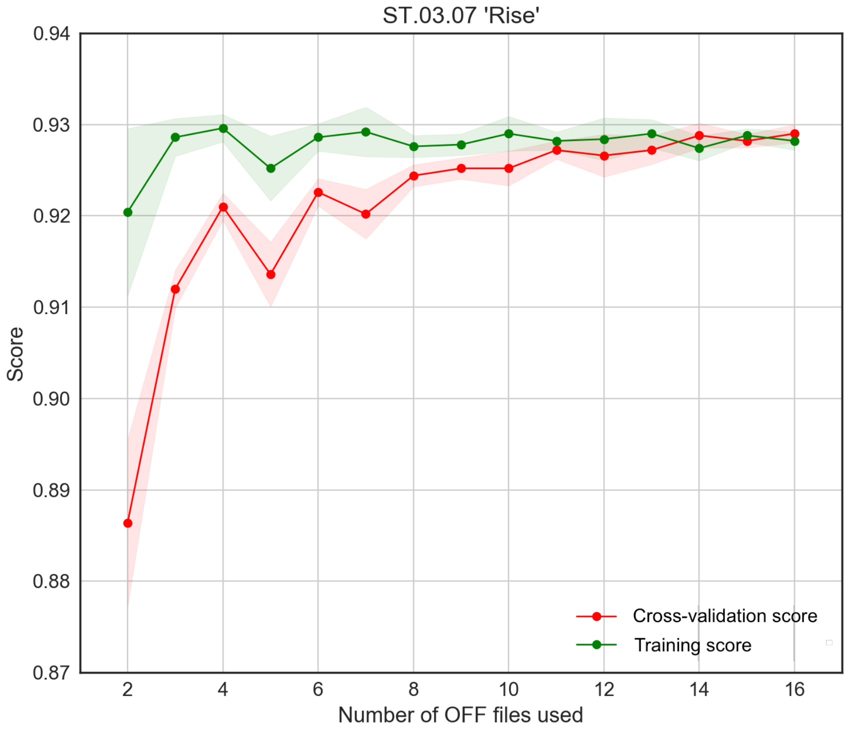

Figure 36: Learning curve for period 2 sample "Rise".

This method is especially useful for samples with low statistics and no dedicated background observations available. If the sample is big enough, the learning curves can still be created, but in the case of the MAGIC data analysis pipeline it is possible to train data with a $1:1$ training ratio between MC and OFF data. In that case, the RF would not use more hadron-like events than the number of MC events, so if there are enough observation hours a safe choice is to randomly select the minimum amount of data which covers the zenith and azimuth distributions of MC events in each bin of the range specific to the analysis.

3.3.3 Monte Carlo to data differences

The underlying assumption when producing MC data is that the information it encapsulates does represent the basic truth. This is somewhat naïve thinking, since reality can be more complex.

One part of the analysis is concerned with checking whether or not such MC data reflects the gamma-like signal, which we suppose is at the centre of the source skymap. This has a twofold advantage. On one side we can test our simulations and assess whether they need to be modified, in order for them to be more realistic depending on the properties of the putative signal we observe. Additionally, since we use the MC data to build a RF, we can improve the check by using such data to compare directly the source's data with the simulated gamma-ray signal. A possible way to do this, is to use the same parameters exploited by the RF with which the fully analysed events were produced.

The procedure proposed for VLZA data analysis considers the distributions of - at least - each parameter used by the RF (6 specific to each telescope in the standards version). For each one of the parameters, 3 samples of data are considered: MC data, data from the source, and data from a region consistent with the background. The OFF region could be chosen in an arbitrary position within the FoV (provided it doesn't overlap with the source's region), e.g. - as in this case - symmetric with respect to the centre of the camera, being the observations in wobble mode (2.2.4).

Each of the three distributions are produced considering a looser baseline cut than those usually considered for signal studies. This is especially needed in case of analyses for which only a few events are expected. I used the two-sample Kolmogorov–Smirnov (KS) test [59] to compare each distribution between the simulated γ-rays and the excess, which is estimated from the number of counts resulting from the subtraction of the background ones from those arriving from the source's direction in the sky. If strict cuts were used, the resulting number of counts from the excess sample wouldn't be statistically sufficient for the Kolmogorov-Smirnov test to produce an unambiguous result.

The chosen cut has been the following (but different ones can still be used, provided they are loose),

- hadronness < 0.9,
- (stereo) SIZE > 50 phe,
- energy > 1 TeV,
- $70^\circ <$ zenith angle $< 80^\circ$

In particular the chosen energy could in principle be the bare estimated one or the one already corrected for both atmospheric attenuation (see 3.4.1), and for the bias between the energy estimation algorithm used and the true energy simulated in the MC data see 3.4.2. In Fig.37 I show the distribution of MC events and excess events for the set of parameters used in the MAGIC collaboration for standard RF analyses.

For each parameter the supremum of the absolute difference between the two distributions is calculated as,

$$KS_{i,j} > c(\alpha)\sqrt{\frac{i+j}{ij}}, \tag{7}$$

where i and j represent the sizes of the two samples, and the sign sets the condition for which the null-hypothesis (H_0) is rejected at the confidence level α. In particular H_0 corresponds to the assumption that the two samples come from the same parent distribution.

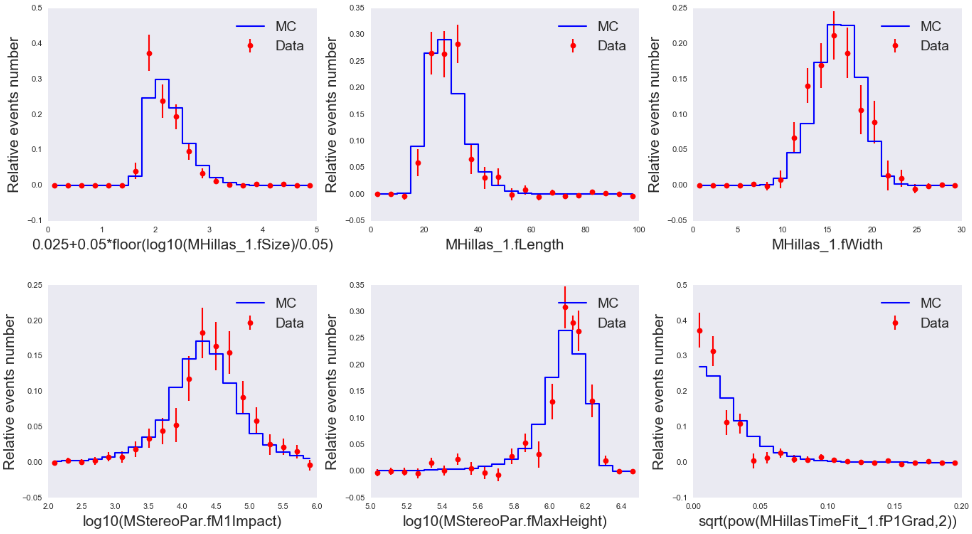

Figure 37: Comparison between the distribution of MC events and excess events at VLZA for standard parameters used in the creation of MAGIC Random Forests.

The values of $c(\alpha)$ for the parameters shown in Fig.37, where MC is compared to the excess signal, and the correspondent rejection levels are listed in table 2.

Table 2: Values for the Kolmogorov-Smirnov statistics applied to standard Random Forest parameters at VLZA.

Parameter	$c(\alpha)$	H_0 rejection level
$0.025 + 0.05 * \mathrm{floor}(\log_{10}(\mathrm{Size})/0.05)$	0.100	1.96
Width	0.046	1.99
Length	0.052	1.98
Impact parameter	0.079	1.97
Max shower height	0.072	1.97
$\sqrt{\mathrm{MHillasTimeFit}_1.\mathrm{fP1Grad}^2}$	0.123	1.94

The test shows that all standard parameters are generally still good to treat VLZA data.

3.4 HANDLING OF THE ESTIMATED ENERGY

The estimated energy values obtained either from look-up tables or from the stereo Random Forest approach, suffer from two main effects which have to be taken into account in this analysis, and that are independent of the chosen estimation method.

3.4.1 Corrections for atmospheric absorption

In order to take care of the atmosphere's big influence on VLZA data, the usual monitoring and treatment of data quality is not sufficient.

Like in the case of LIDAR corrections, even if the transmission value for a given observation run is acceptable from the point of view of the quality of data (see e.g. 2.1.2), one still has to correct for the estimated energy that the same shower would have had it not been absorbed.

As explained in 3.2.1, the possible correction provided by the LIDAR instrument at VLZAs is not sufficient to account for the bigger development distances traveled by the showers. The integral measurement given by the pyrometer (3.2.2) is equally unsuitable at such regimes, if not worse, because it can show worse data quality than it really is (3.2.2).

An alternative solution is borrowed from optical astronomy: measuring the optical attenuation. This technique has been developed and applied by members of the VLZA team. This method relies on an integral measurement, like in the case of the pyrometer, but results in a more direct estimation of the quantity at hand. This type of measurement is more trustworthy for two main reasons:

- it can be calibrated using an approach independent from the rest of the system;
- it does not require the operator/analyser to know the details of the atmospheric composition at the time of the data taking.

The instrument used for this purpose is a CCD camera, placed at the centre of the MAGIC-1 dish (see Fig.9). Fig.38 shows an example of how such a device operates and in particular what its FoV looks like. The camera can work using three filters in the colour configuration R/G/B, though the data used for this work used had only green filter measurements because the correspondent transmission window is closest to the Cherenkov signal aim to measure.

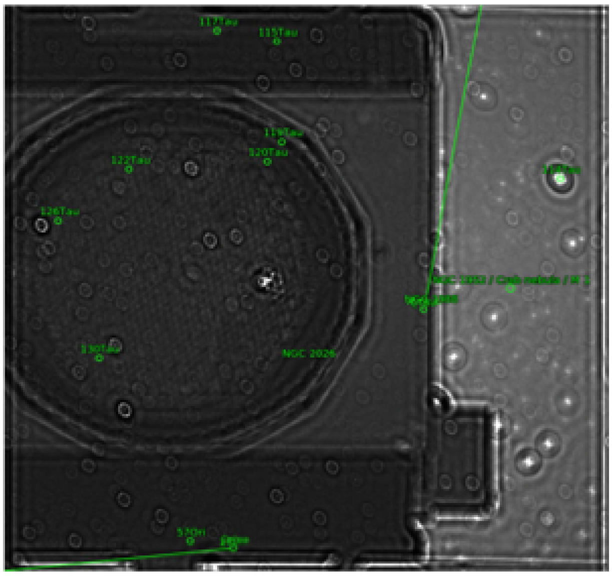

Figure 38: Screenshot showing the FoV of the SBig camera and the identification of he brightest stars from the semi-automatic script. Courtesy of Jurgen Besenrieder.

In the following I explain what is the methodological process underlying these measurements and how the energy correction is applied to the data.

Taking a known star in the FoV of the source observed by MAGIC-1 as a reference, two related quantities have to be considered: the (intrinsic) light intensity as measured outside the atmosphere, and the absorbed light intensity at the ground level. In the following these quantities will be denoted by, respectively, I_0 and I.

These observables can be linked directly to the associated magnitudes of the pointed star: M and m respectively. In this definition, while m can be effectively regarded as the *apparent* magnitude, M should not be confused with the usual *absolute* magnitude, for which the distance is 10 parsecs. In this case M refers to the star's magnitude just outside the atmosphere.

The relation between these two quantities is shown in (8) and sketched in Fig.39. It is useful because it reflects the effect of integral attenuation by the atmosphere the light crosses to reach the observer.

$$m = M - 2.5 \log\left(\frac{I}{I_0}\right). \tag{8}$$

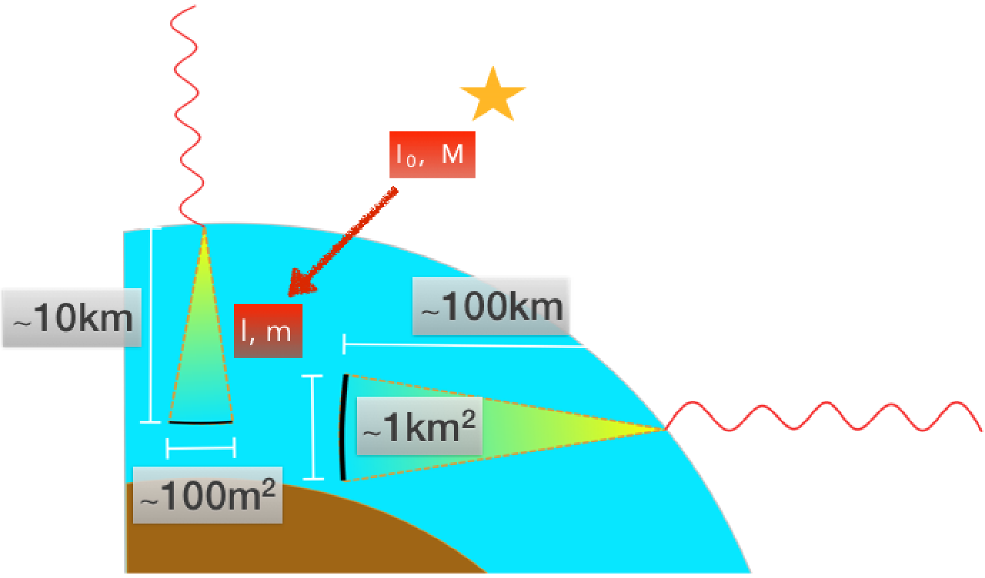

Figure 39: Cartoon illustrating the concept behind the idea of using optical attenuation measurement to monitor the atmosphere at Very Large Zenith angles. Order of magnitude values for shower development at different zenith angles is also reported

The atmosphere will of course have its own intrinsic properties, but this is of no immediate interest for VLZA observations.Indeed, with some approximation the atmosphere can be described with few parameters with no prior and precise knowledge of its local conditions.

Setting the reference frame at a particular position on the ground, we can limit ourselves to a bi-dimensional plane, spanned by a polar coordinate system described by the zenith angle (z) and the altitude (h). In this picture the density profile of the atmosphere will be completely described by these coordinates as $\rho = \rho(z, h)$.

At this point we need to introduce some sort of integral description of the properties of the material. As stated before, being this an integral measurement based on a known reference value - the star's magnitude as measured outside the atmosphere - we can encapsulate all the information about the chemical species and in a single entity.

The more convenient direction along which to define the integral measure is the LOS. Along this direction the *optical depth* describes the total amount of absorption suffered by the traveling radiation. The information about the effectiveness of the absorber is summarised in the *absortion coefficient* α.

What matters is that the optical depth can be written as a function of the absorption coefficient along the LOS,

$$\tau = \int_{x_0}^{x} \alpha\rho(z, h)dh, \tag{9}$$

where x_0 and x are the altitudes associated to the observer and to the edge of the atmosphere respectively.

Through τ we can link the ground-observed intensity of light to that at the top of the atmosphere,

$$I = I_0 e^{-\tau}. \tag{10}$$

Since the final observable are the magnitudes, substituting (10) in (8) allows us to write the measured quantity as a function of the integral properties of the damping medium. The approach through which equation (10) is treated is usually empirical. Numerical tables dependent on a set of approximations used to model the atmosphere are used in literature to estimate the optical depth.

The quantity of interest to us is the *attenuation* caused by the extinction effect of the atmosphere. The usual way to treat it is through the *airmass X*, which is defined as the path length that light has to travel through the atmosphere. Airmass is a function of the zenith angle, $X \equiv X(z)$.

Describing τ in terms of X, allows us to cast equation (8) as a linear relation between magnitudes and amount of material traversed by light along the LOS,

$$m = M - \beta X(z) \tag{11}$$

where β is a parameter factored out as a result of the mapping $\tau \to X$. This coefficient now encapsulates all the underlying assumptions about the atmosphere properties. The atmospheric absorption is then,

$$A \equiv m - M = -\beta X(z). \tag{12}$$

The linear relation between A and X is then calibrated using multiple images pointing at different zenith angles. This allows one to compute β and apply the corresponding estimated energy correction (2.2.3) event-wise.

Figure 40 shows an example between two nights in which the atmospheric conditions were quite different. The presence of inhomogeneous and anisotropic absorbing material causes the absorption vs. airmass relation to wobble around the linear relation implied by a purely geometrical density profile.

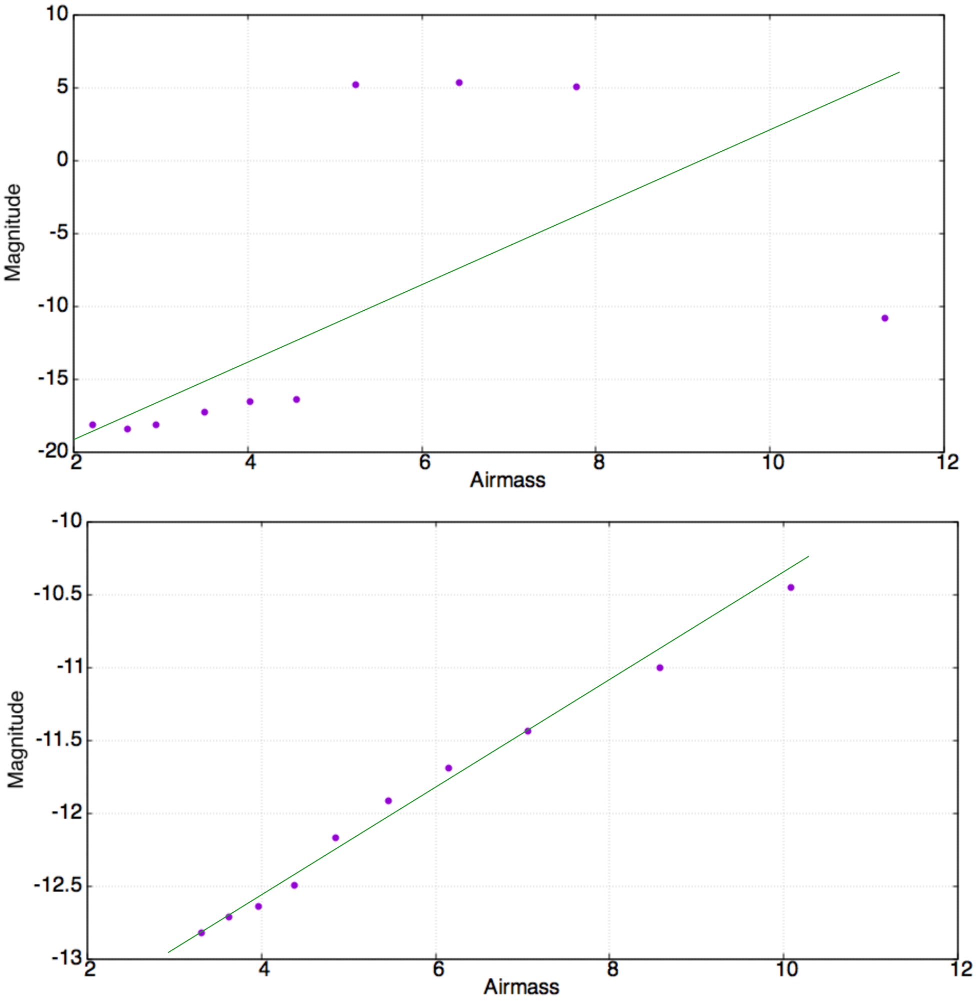

Figure 40: Example showing the comparison between a clear night along the LOS at VLZAs and a night with non-negligible absorption.

In order to apply the correction as $E_{est} \rightarrow E_{est}/\tau$ (which is the same final step of the LIDAR atmospheric corrections 2.1.2) we need to retrieve the correct values for τ. As mentioned before, τ is usually reported in numerical tables, but we also have the advantage of a reference system given by MC simulations: the informations on τ are embedded in the atmospheric model.

A limitation in the use of data from CCD images is caused by the current manual operations. This prevents a continuous record of data and for this reason in this work the applied corrections are applied event-wise for each night's absorption data separately.

Fig.41 shows the distribution of absorption values measured along ~1.5 years using the green filter. The overall integral quality of the atmosphere along the LOS was acceptable during the observation time. The average value corresponding to this set of correction is ~ 0.9.

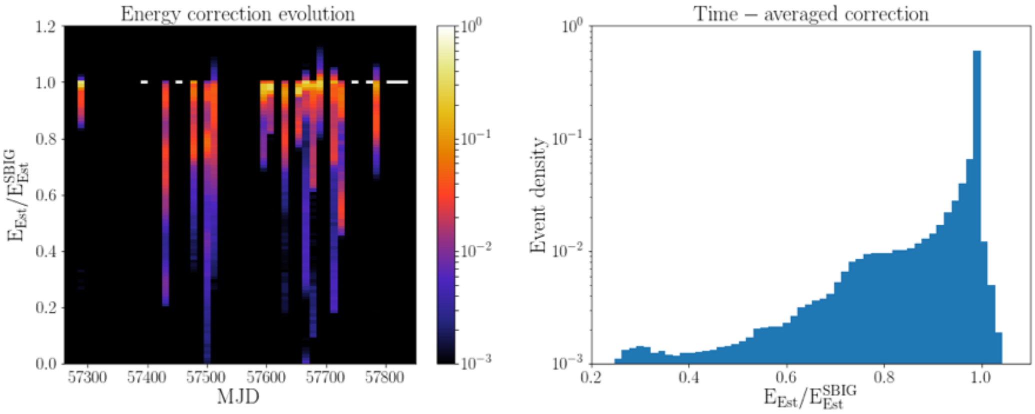

Figure 41: Left: time distribution of energy correction values from absorption measurements carried out with the green filter of the CCD camera, Right: distribution of the normalised number of events with a given energy correction. Courtesy of Dr. Ievgen Vovk.

3.4.2 Energy resolution and bias correction

As reported in [37], the approach through which the performance of energy estimation is assessed makes use of the migration matrix. The migration matrix describes how much the energy estimation process smears the events' estimeted energies with respect to the "true" energies given by the MC data.

During the study and optimisation of VLZA data analysis, both the LUT and stereo RF methods are used, even though the stereo RF energy estimation should work better (2.2.3).

In Fig.42 I report the migration matrices for both methods currently implemented at VLZA. The diagonal spread suggests that the stereo RF method is indeed better than the LUT, even though the latter refers to MC data taken at much higher ZA than usual.

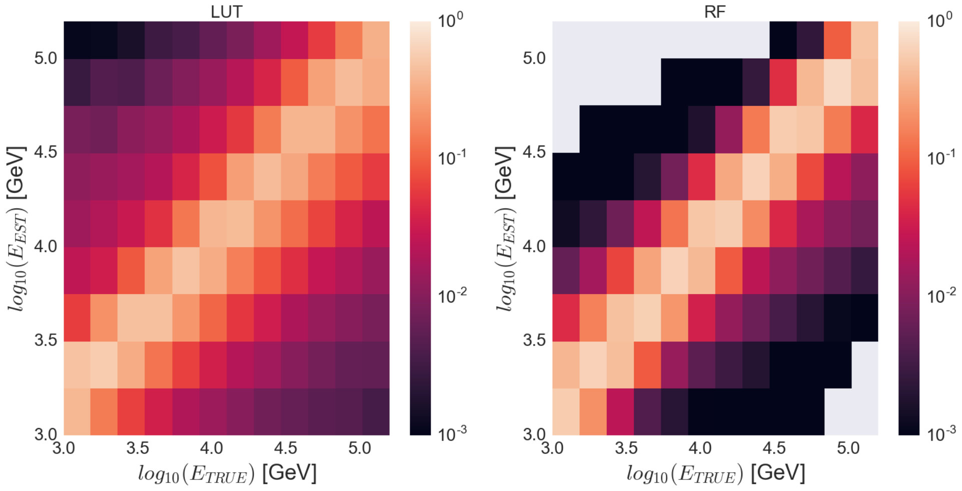

Figure 42: Migration matrices for both energy estimation methods applied to VLZA data. The number of events is in logarithmic scale. Blank bins represent no events.

To be more precise, from the migration matrices I extracted both the energy resolution and the bias. As for [37], the approach consists in calculating the relative difference between estimated and true energy,

$$\langle \frac{E_{est} - E_{true}}{E_{true}} \rangle, \tag{13}$$

where the denominator is the central value of each E_{true} bin, and the numerator has to be treated statistically. For each E_{true} bin, the quantity $\langle E_{est} - E_{true} \rangle$ is fitted by a Gaussian function. Then the bias and the energy resolution for the chosen energy estimation method will be the mean and the RMS of the fitted Gaussian.

Indeed, if the energy estimation produces too smeared a migration matrix, in each E_{true} bin the tails of E_{est} will spoil the RMS of the fit, resulting in a worse energy resolution - even if the bias is small.

Bias and energy resolution of VLZA data are reported in Fig.43, always using the subsample with more statistics as a reference in order to minimise fluctuations.

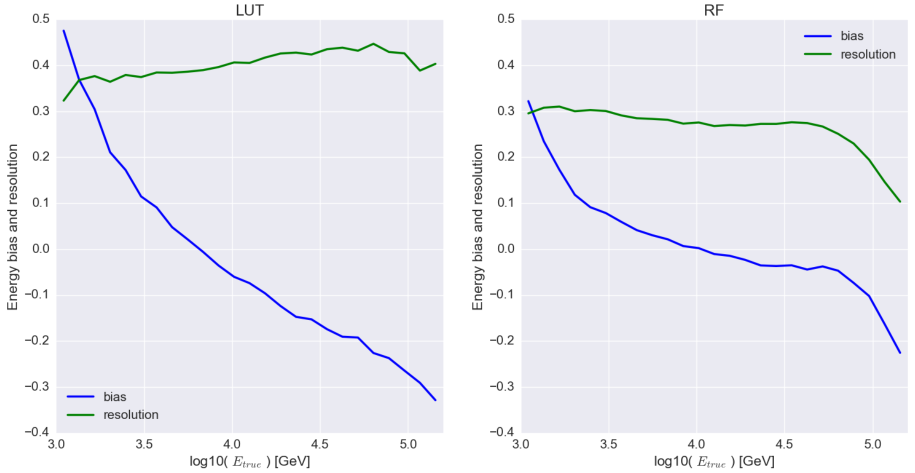

Figure 43: Bias and resolution of estimated energy for LUT and stereo RF applied on VLZA data.

As the figures show, this is also a crosscheck of Fig.42: the stereo RF method performs better at all energy scales, even though its power is not as good as in [37] where the ZA$<45°$.

While the energy resolution power cannot be changed after the events have been labeled with their estimated energy, something can still be done for the bias. The way I correct the bias is by adding the true energy central value to the average absolute difference between it and the estimated energy,

$$\left\langle \frac{E_{est} - E_{true}}{E_{true}} \right\rangle \rightarrow \frac{\langle E_{est} - E_{true} \rangle + E_{true}}{\langle E_{true} \rangle}. \tag{14}$$

This could be done by implementing the mapping for each true-energy bin, but I fit the bin-wise values with a second-order polynomial right after retrieving the bias and the resolution from the Gaussian fits. The result is given in Fig.44, where for reference I also report the line corresponding to perfect energy estimation (i.e., no bias).

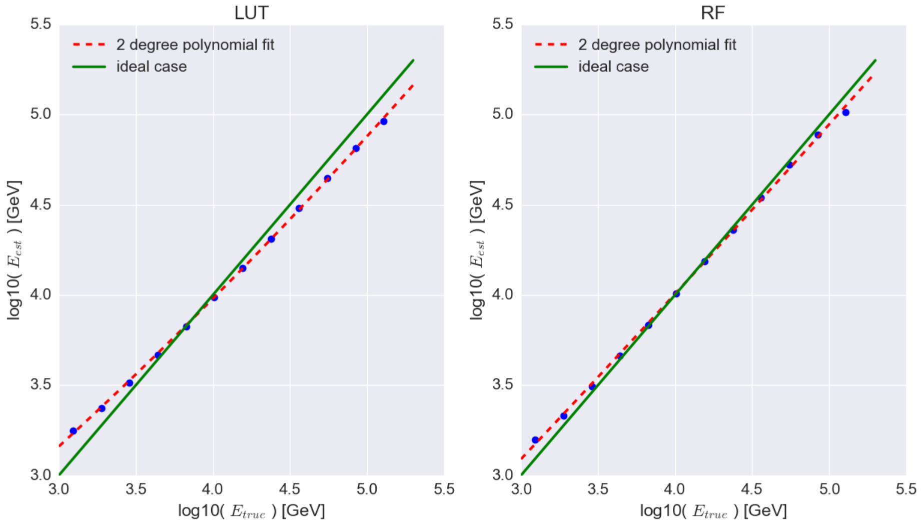

Figure 44: Polynomial fit for bias correction applied to both energy estimation methods. Blue points: 12 bins in true energy, Red dashed line: second-order polynomial fit, Green continuous line: case with no bias.

We can see also from here what the blue lines describe in Fig.43: the stereo RF methods suffers from less bias, also when observing at VLZA.

With the polynomial as a guide, it is possible to retrieve a value of E_{true} energy for each arbitrary value of E_{est}. This allows one to apply equation (14) to each event of the source at hand, using a value of E_{true} that refers to each E_{est}, already corrected for the atmospheric attenuation.

3.5 PRELIMINARY RESULTS AND CURRENT DEVELOPMENTS

The correction of E_{est} for atmospheric attenuation and bias with respect to the MC simulations is critical for the study of VLZA data. The application of such corrections highlights the dependence of VLZA data on this operation and the limitations caused by the simulated γ ray data when processed by methods such as the stereo RF. Fig.45 shows the result of the energy correction for these two effects from the point of view of the better-performing stereo RF method.

It can be seen that while the bias is more effective on multi-TeV events, the biggest effect is given by the atmospheric correction. This is a further proof of how important the treatment of the atmosphere is for IACT data in general, but more importantly so at VLZA.

Note how the limitations in maximum energy are also a factor in treating VLZA data. Indeed, Fig.45 shows that the RF estimated energy stops abruptly at the maximum MC energy (150 TeV, at the time of this work), thus suggesting that the flux continues further in energy. This is due to a built-in limit of the RF method, which cannot estimate values bigger than the biggest provided by the training data - the MC. It is then critical to improve MC simulations for IACTS to treat input energies $\gtrsim 100$ TeV.

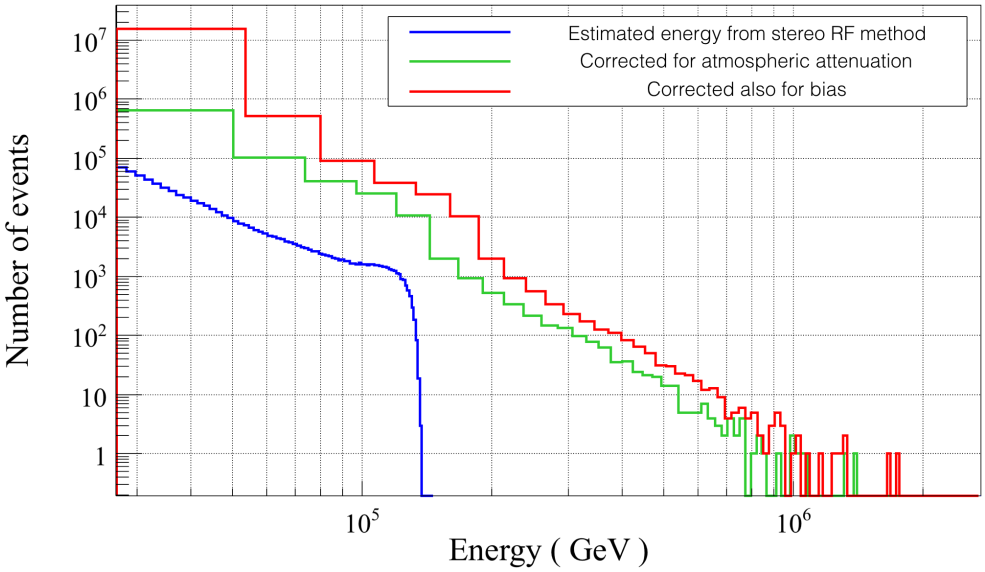

Figure 45: Correction of the energy for atmospheric absorption and bias using the estimated energy as retrieved by the stereo RF method.

When applying the techniques explained in this chapter to real data we can appreciate how VLZA really boost the effective collection area, with energies that on average reach ~100 TeV. Fig.46 refers to preliminary unfolded analysis of data already shown in this work.

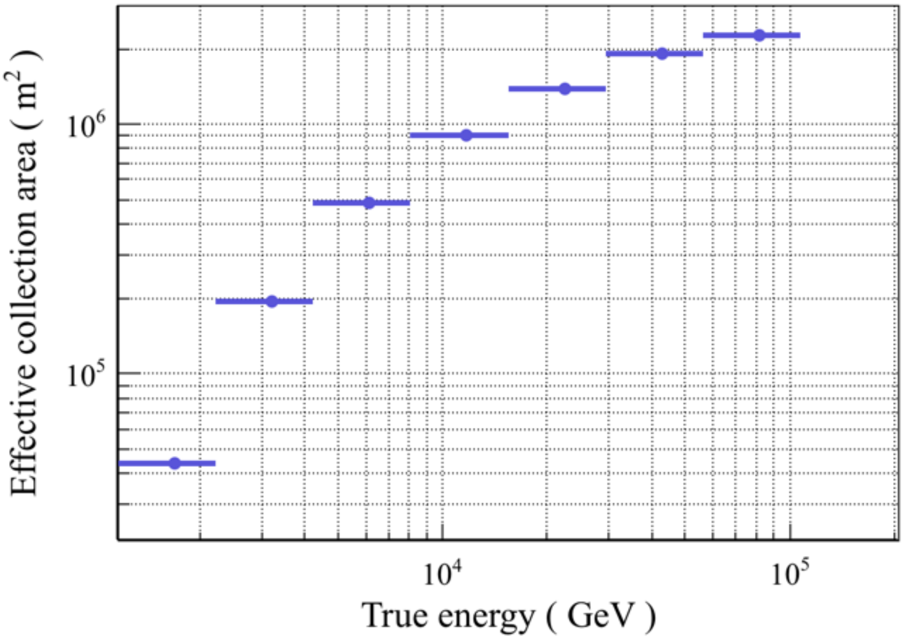

Figure 46: Effective collection area as a function of true energy for VLZA observations.

This result shows that with VLZA observations we can boost the collection area (with respect to conventional IACT operation) by at least one order of magnitude, i.e., from $\sim 10^5 \mathrm{m}^2$ to $\sim 10^6 \mathrm{m}^2$. These are indeed the main advantages of VLZA observations applied to MAGIC: we can collect gamma rays from a ~10 times bigger area, and at the same time our energy threshold is also ~10 times higher, allowing us to boost our sensitivity towards the highest energies. Fig.47 shows the energy threshold estimate corresponding to the collection area shown in Fig.46. This result is obtained by applying the following preliminary cuts for a high level analysis to the same MC data used to calculate the effective colletion area,

- $70^\circ < \mathrm{Zd} < 80^\circ$,
- hadronness < 0.3,
- size > 50 phe,
- power-law photon index ~ 3

Since the spectral index from the MC simulations is -1.6, the implementation of the source spectral index is modifed by a spectral weight, resulting in a MC spectral index of -1.4.

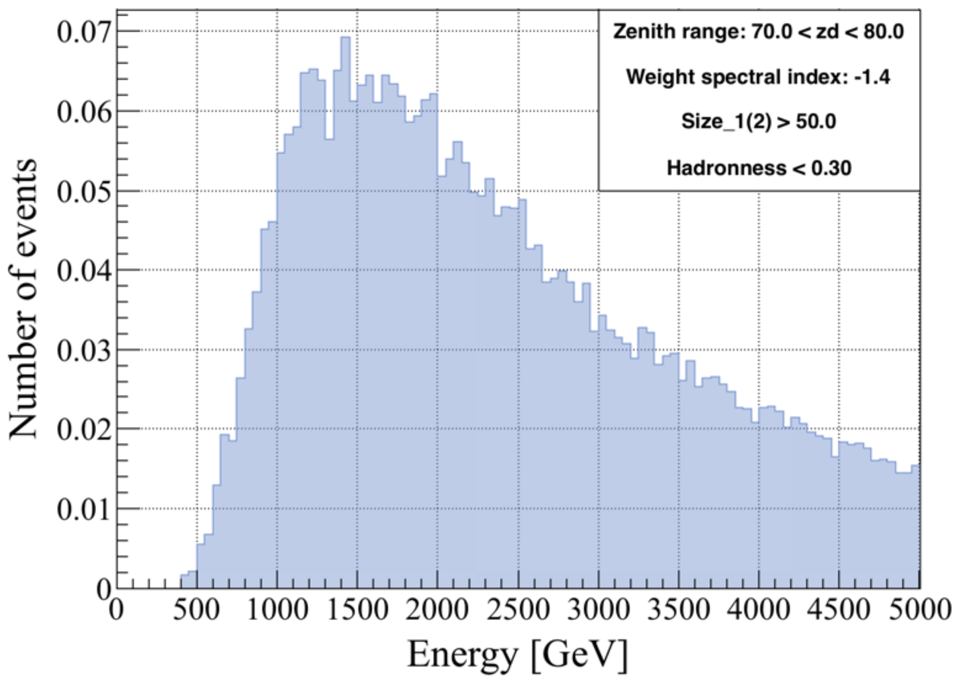

Figure 47: Normalized number distribution of simulated MC events as a function of energy, given preliminary cuts for a high-level analysis at VLZA. The energy threshold of the analysis corresponds to the peak of the distribution, here roughly at ~1.4 TeV.

These results demonstrate that VLZA observations have promising potential for applications with IACT facilities such as the MAGIC telescopes. We are reaching energies that had never been reached by instruments of this kind, with about a tenfold improvement in collection area.

A big limitation of these studies, however, will be the production of MC data, both general and specific for sources at VLZA. Current developments in the MAGIC collaboration have involved dedicated MC productions aimed at estimating some relevant systematics and at boosting the maximum energy available to the simulations.

My work focused on the optimisation of the standard analysis. The results shown here suggest that there is still room for improvement, especially in the exploration of additional parameters relevant for γ-hadron separation.

Important contributions from different members of the collaboration involve the application of modern machine learning techniques to γ-hadron separation and energy estimation: these techniques involve artificial neural networks and possibly also deep learning techniques in the future.

In the future it will be important to apply these new methods, which are already used by upcoming next-generation IACT facilities [38].

In addition, the MAGIC collaboration has purchased a spectrograph provided with a CCD camera for improved atmosphere calibration. In particular with this instrument it will be possible to get spectra and light curves from any source via measurement of optical fluxes. Current logistical and constructional operations are ongoing.

4 THE FIRST NEUTRINO-GAMMA ASSOCIATION

In 2017 a major breakthrough interested the astronomical community worldwide, and with it also the MAGIC collaboration.

Among the different activities carried out in MAGIC, the search for VHE emission from transient events is one of the most important. Different types of transient events are scheduled for observation thanks to external alerts mainly issued through the Gamma-ray Coordinates Network (GCN) [60]: from Gamma-ray Bursts [61] to Active Galactic Nuclei (AGNs) flares. In this chapter I report about a particular AGN flare, which I had the opportunity to analyse at VHE.

On September 22^{nd} 2017, MAGIC received an AMON [62] [63] [64] notice from the IceCube collaboration: a high-energy neutrino track event was detected [27]. This event was also communicated through GCN, and prompted observations from different experiments, observatories and satellites [27].

This work will focus on my contribution on the subject as a member of the MAGIC collaboration, and in particular on the data analysis of the source discovered in VHE γ-rays for the first time in this occasion - $\mathrm{TXS0506+056}$.

Among the internal proposals in MAGIC this event fell within the follow-ups of neutrino alerts from the IceCube experiment [65]. In events such as this, fast response from the interested telescopes is required. The observational limits of MAGIC constrain the operations starting after an external trigger alert:

- the Sun needs to have a zenith angle of more than 103°, in order to be considered below the astronomical horizon,
- in case of partial Moon, this needs to be offset by at least 30° from the alert coordinates; during stronger Moon no transient observation is scheduled,
- observation continues up to 50° zenith,
- the observation time for the transient event is nominally 3 hours, even though this limit can be modified depending on each situation.

The software meant to supervise the whole process and the performance during fast-movement has been recently described in [66]. In the case the later classified event $\mathrm{IceCube-170922A}$, such observational limits did not allow to observe the source within the first couple days due to excessive winds (cfr. 2).

The MAGIC telescopes scheduled a first observational slot after about 32 hours on the night of September 24th observing for 2 hours under non-optimal weather conditions. Afterwards followed 3 nights of bad weather conditions, preventing further observations.

At the time of the scheduling procedure and first operations, the location in the sky correspondent with the IceCube coordinates did not include any

VHE source. Four days after the IceCube alert, the collaboration operating the Large Area Telescope (LAT) instrument [29] onboard of the Fermi Gamma-ray Space Telescope reported the observation of enhanced γ-ray activity from a source in the initial error circle released by IceCube [67].

The angular offset from the best-fit neutrino direction was ~0.1 deg [27]. The γ-ray source observed by LAT was later identified as 3FGLJ0509.4 + 0541, an already known High Energy (HE) source [68]. In particular such source was known to be an AGN *blazar* [69], classified as a *BL-Lac* object with unknown redshift.

Motivated by the LAT detection, the MAGIC telescopes followed the source under mostly good weather conditions starting from September 28th. Fig. 48 shows the final best-fit position observed by the MAGIC telescopes in VHE γ rays.

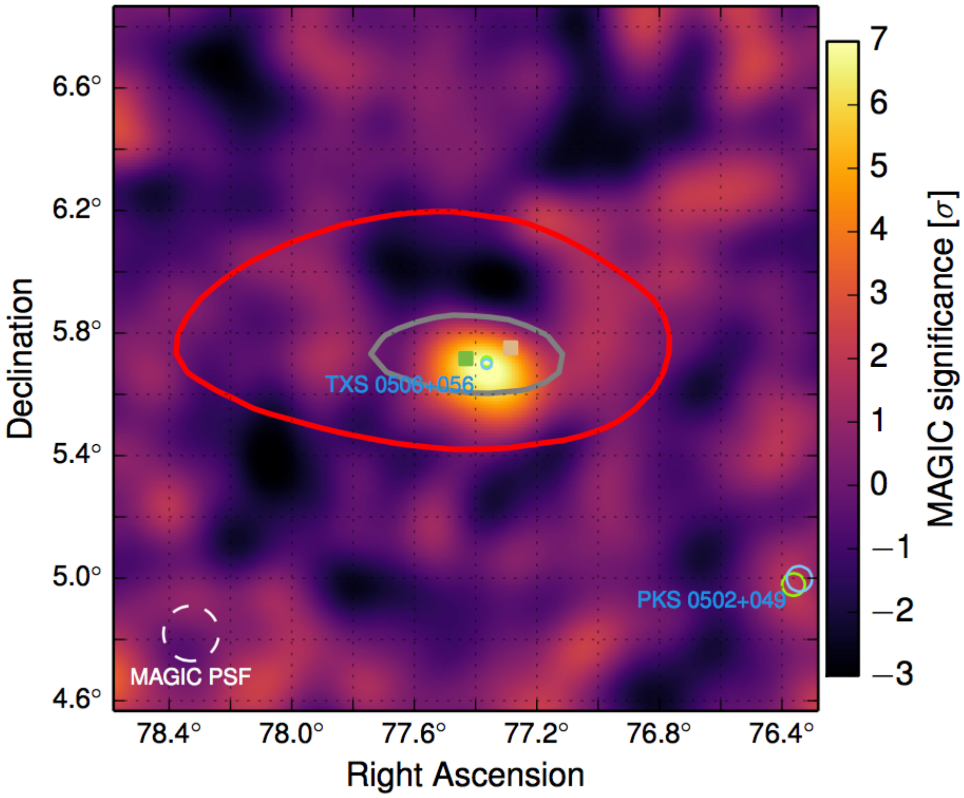

Figure 48: Sky position of IceCube-170922A in J2000 equatorial coordinates overlaying the signal significance as observed by MAGIC. Tan square: position reported in [70]; Green square: final best-fit position. Gray and red curves show the 50% and 90% neutrino containment regions, respectively, including statistical and systematic errors. [27].

The time interval corresponding to the analysis described in this chapter goes from September 24th to October 4th. This period, apart from the very first day of bad weather, coincides with the observational campaign leading the collaboration to the release of an ATEL communication [71] [72]. In this telegram MAGIC reported about a flare peaking around the two last days.

4.1 DATA QUALITY

The source has been observed within zenith angle in the approximate range of 22°– 52°, as shown in Fig.49.

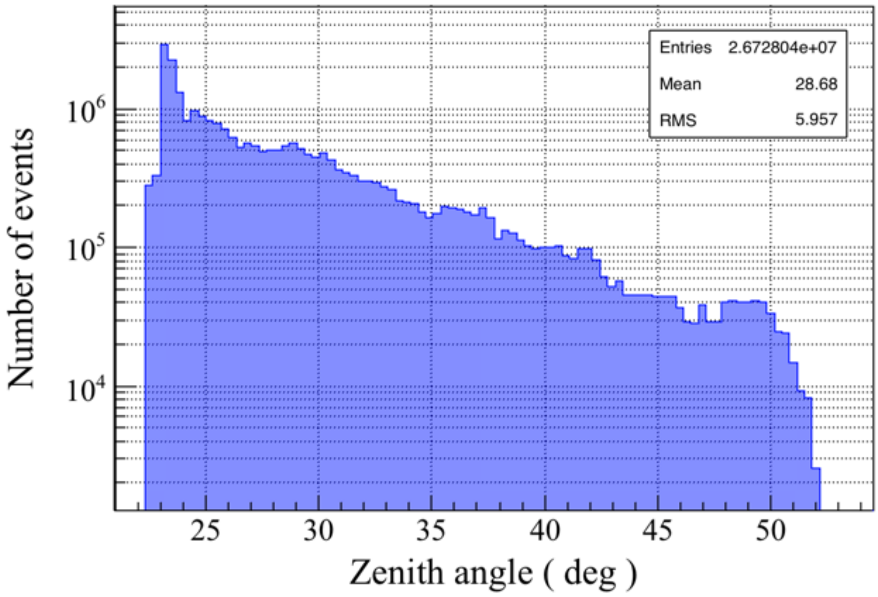

Figure 49: Event-wise distribution of zenith angle for all data of TXS0506 +056 shown in this work.

The first day of observation (September 24th) suffered from rather low transmission values due to bad weather conditions: the atmospheric transmission, measured by the LIDAR instrument, were equally distributed both over and under the threshold of 70%, resulting in only ~ 50% of the time surviving such quality cut. The remaining observational time was taken under much better conditions: all data survived to a 70% transmission cut at a distance of 9 km (crf. 2).

In Fig.50 I report the distribution of values for transmission at a distance of 9 km; such values refer to those already re-calibrated by the data quality software (2.2.1).

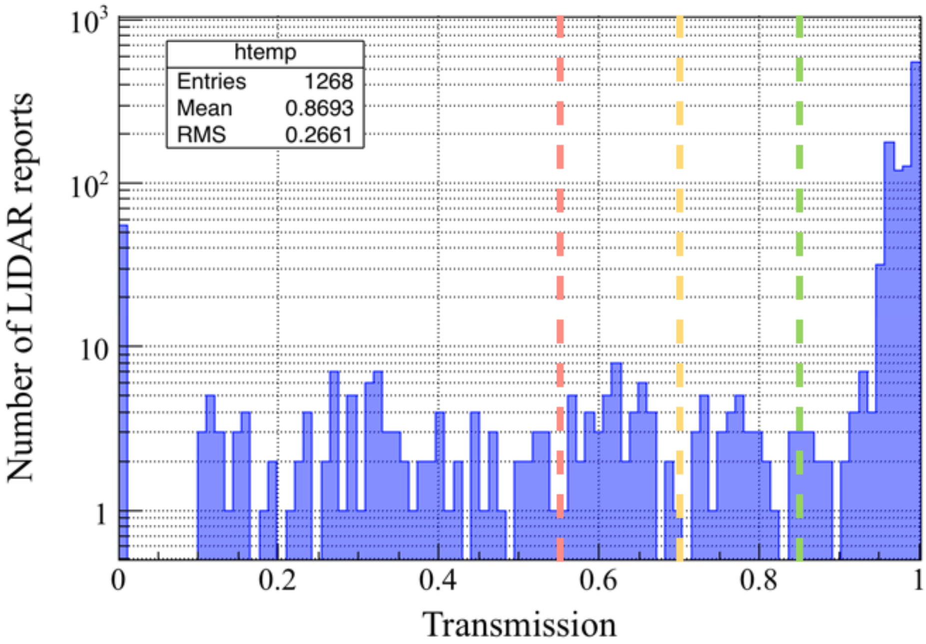

Figure 50: Distribution of reports from LIDAR transmission as measured at a distance of 9 km. Green, yellow, and red dashed lines show the transmission levels at 85%, 70% and 55% respectively.

Direct current levels have been almost always within the nominal limits of dark-compatible levels NSB < 2 (2.1.1) for about 92% of the time during the ATEL period. A minor quantity of data equivalent to 0.8% for which the levels increased up to 3.3μA. I treater this data separately, in order to check its compatibility within the standard analysis procedure.

Following the standard approach I checked on the percentage of survived pedestal events (crf. 2) registered by the electronics of MAGIC-1. I found a-priori values incompatible with dark-level analysis only in the last days. This quantity is shown in Fig. 51 where the nominal level for dark-compatible data equivalent to ~10% is also reported. As it can be seen, even though light from the dawn was starting to increase the NSB, such data could still be used, compatibly with dark analysis.

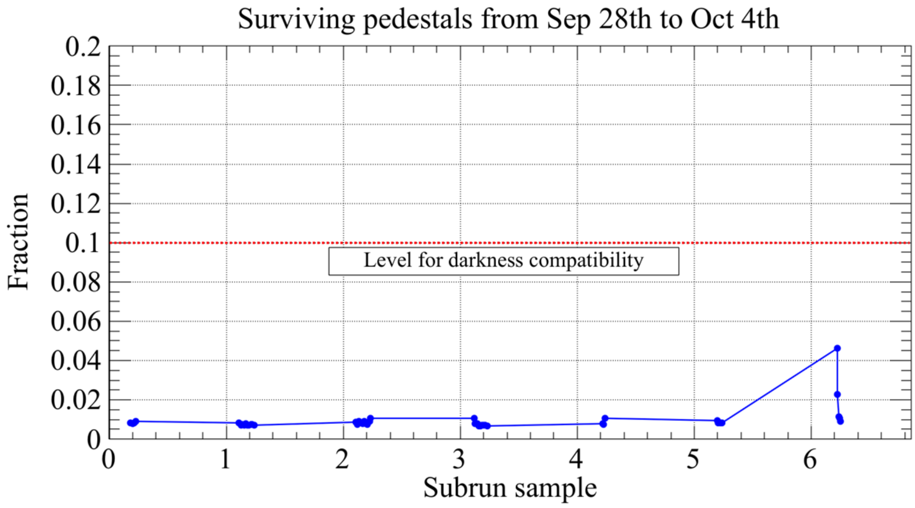

Figure 51: Fraction of surviving pedestals during the period of TXS0506+056 containing apparently high DC levels.

Taking into account the quality cuts here explained, ~ 13 hours survived the cleaning procedure and so I considered them as good data to be analysed.

4.2 RF AND TEST ON CRAB NEBULA DATA

During the analysis phase a challenging setback slowed down the analysis efforts.

A monitoring of Crab Nebula data is periodically carried out by members of the collaboration, on both photon and muon data runs. This is done in order to check periodically if the performances of the MAGIC telescopes are sufficiently in line with the ones declared as stable [37].

One of these checks revealed a lower flux and a not optimal spectral energy distribution with respect to previous standard performances. The effect was traced back to a gradual decrease of the mirrors' reflectivity later measured from the end of June till the beginning of November, as shown in Fig.52. A gradual drop in reflectivity is visible when looking at measurements of size (1.2.2) in muon events.

A mirror replacement was performed just at the end of the Atel period, taking advantage of the usual Moon break at the end of the month. Then, by the end of October the site was interested by rains, which contributed to low the dust amount in the local atmosphere.

Indeed, the cause was traced back to the accumulation of dust on the mirrors. This effect is known to affect slightly the telescopes each year, but usually not so much to require a major MC production such as in this case. This noticeable change in performance required different tests aimed at demonstrating how to modify the MC data accordingly.

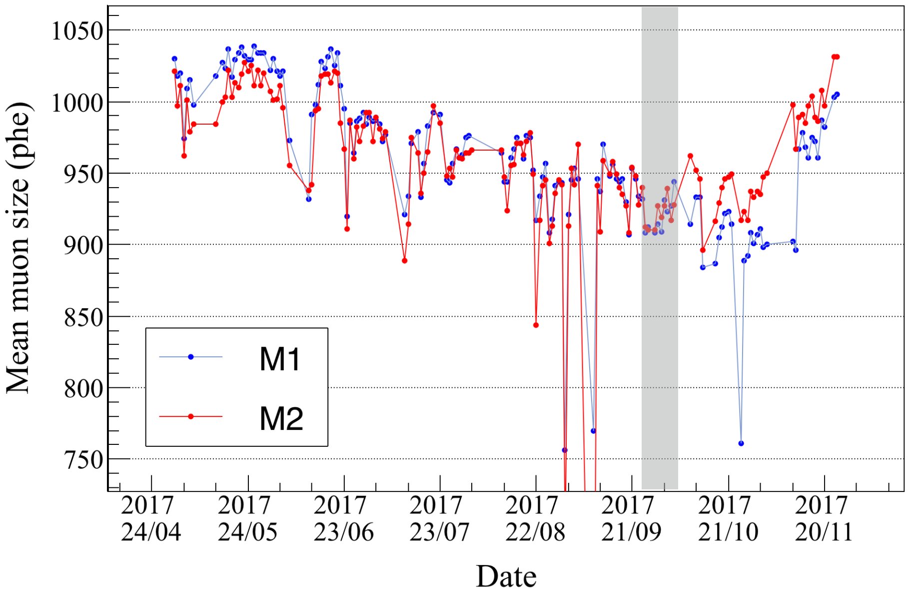

Figure 52: The decrease in mirrors' reflectivity during the period comprising the observations of TXS0506 +056 (grey shaded area). Courtesy of Dr. Julian Sitarek.

It was decided to modify the scaling on energy and size of the event at the level of flux estimation to mimic the degradation effect a-posteriori with the previous standard MC, in order to tune the parameters required for the next dedicated MC production.

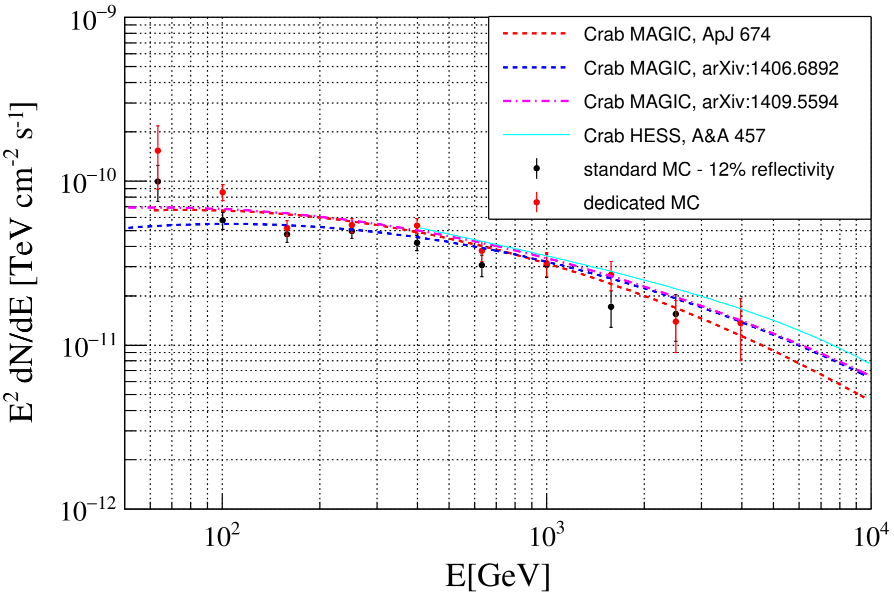

Figure 53: Tuning tests performed in order to estimate the impact of low mirror reflectivity on the MC data during the period coincident with the observations of TXS0506 +056. Courtesy of Dr. Julian Sitarek.

This tuning, of which Fig.53 shows an example, has been done over the same Crab Nebula test data later used for Fig.57. These tests have been fundamental to produce a tailored MC production, in which showers have been simulated again, taking into account the measured degradation in the mirrors' reflectivity. Such MC data have been used for the official results of this analysis and it will be available for any observation falling in the time period interested by the degradation.

Subsequently, I split the entire MC sample in 2 (approximately) equal parts, using the one which had few more events as training sample. I selected the data which simulates the hadronic component for the RF from sources which were never detected in γ-rays.

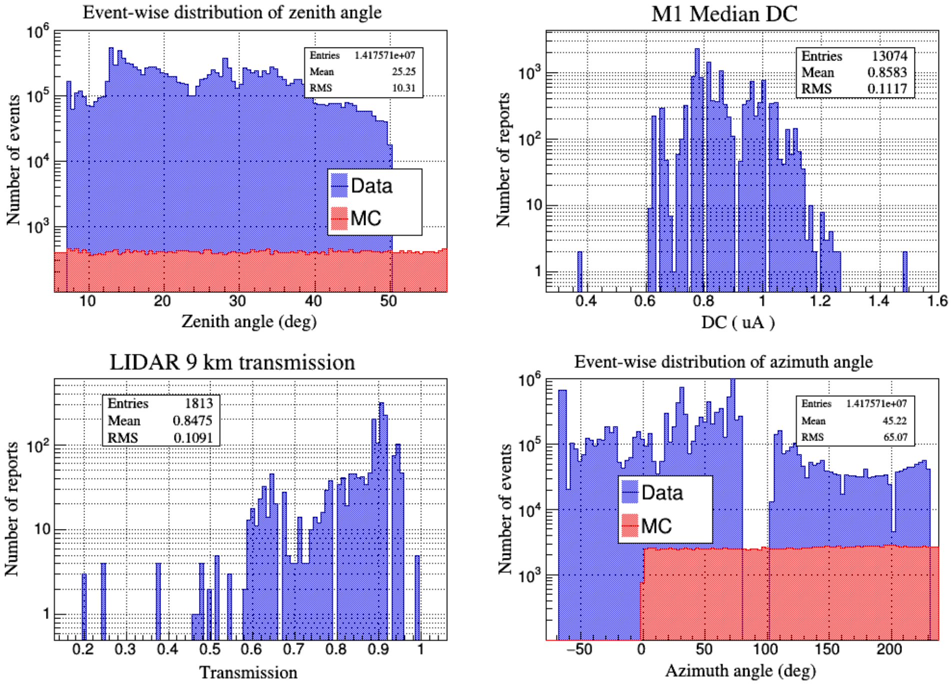

Figure 54: Summary of data quality for the OFF sample used to analyse TXS 0506 +056 before cleaning was applied.

Fig.54 shows the sample properties before any cleaning was applied. The data covered the entire range in zenith angle coincident with that of the real source to be analysed. Events were also more than sufficient with respect to the MC data representing the training γ rays. Direct current levels were consistent, since this data was recorded almost entirely in dark time.

I cleaned the background-like data in order to mimic as much as possible the real data from TXS0506+056. In particular, I applied a cleaning within default time slices of ~2 minutes each, while requiring that all data had a LIDAR transmission of more than 85% at 9 km. This value is higher than the one used for data because, since background-like data used for gamma/hadron separation cannot get any atmospheric correction, the training of the RF has to be performed using data during as much good weather conditions as possible. This is clear also from the point of view of the simulated γ rays: they are produced in a best-case scenario - except for approximations inherent in the atmospheric modelling.

After the cleaning process the coverages of both zenith and azimuth angles didn't suffer any loss that could prevent the use of this data, as can be seen in Fig.55 and Fig.56.

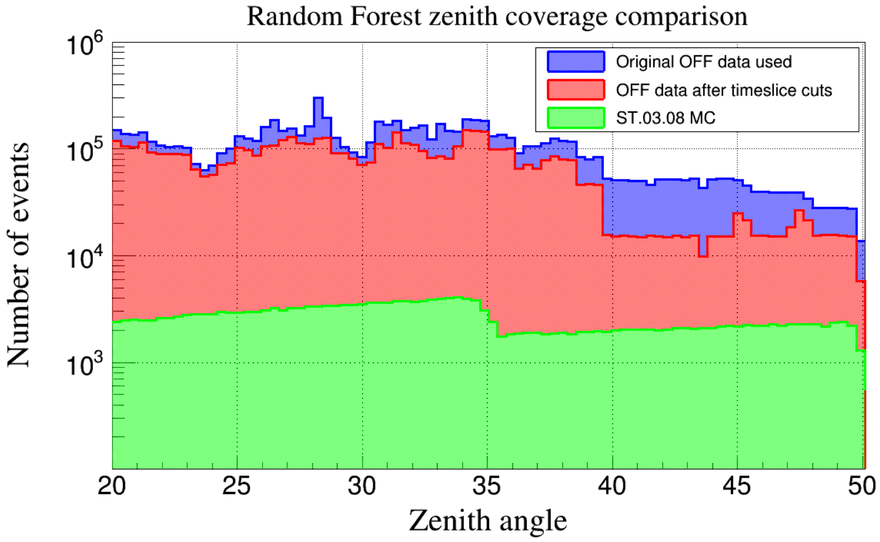

Figure 55: Comparison between the event-wise zenith-angle distributions of MC data and hadron data used to analyse TXS0506+056.

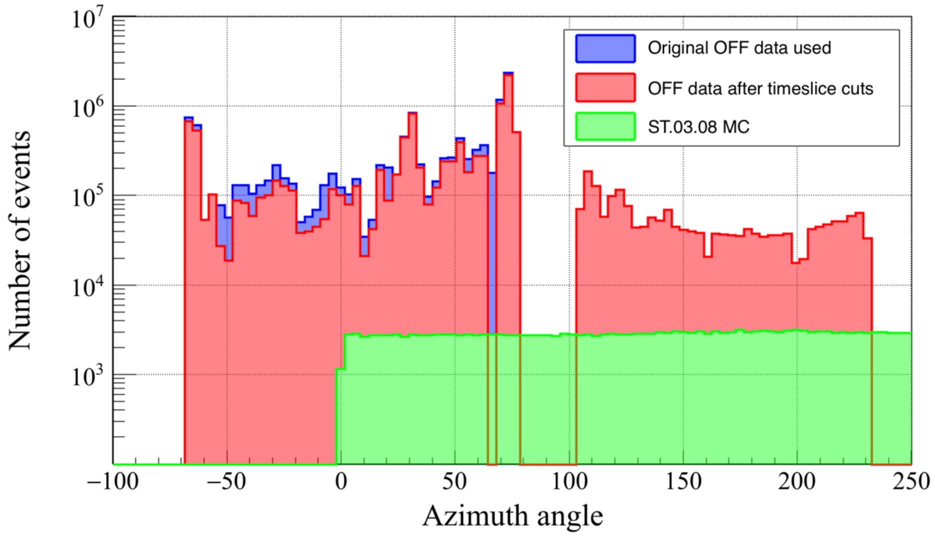

Figure 56: Comparison between the event-wise azimuth-angle distributions of MC data and hadron data used to analyse TXS0506+056.

In order to check if the generated RF was able to perform sufficiently for this source, I tested it on Crab Nebula data. With the aim of getting an outcome as reliable as possible from this check, I selected test data in the same period in which both the background-like data and the real source data were taken.

Given the unusually narrow time period to which this special MC production was referring to, I did not have enough data from the Crab Nebula covering the entire ZA range. However, as it can be seen in Fig.57, the distribution of ZA values, was uniform enough to build a RF with a solid zenith dependence, even though discontinuous.

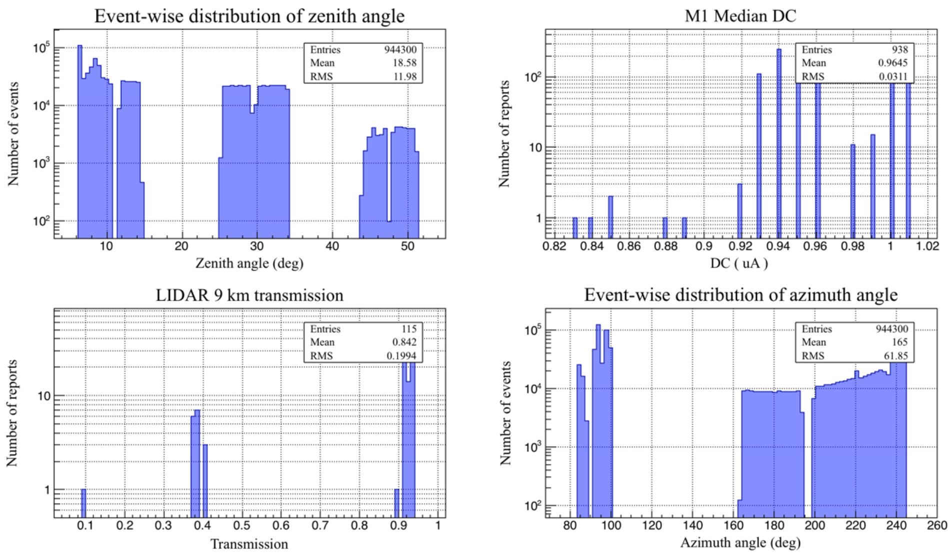

Figure 57: Data quality pre-cleaning of test Crab data used to judge the performance of the RF used for the analysis of for TXS0506+056.

I properly cleaned also this data in order to reflect exactly the observational conditions under which TXS0506+056 had been observed: DC levels compatible with dark-level analysis and a LIDAR transmission of at least 70% at 9 km, which allowed for LIDAR corrections.

In Fig.58 and 59 I show the resulting Crab Nebula SED and light curve respectively, while Fig.60 shows that with this RF the Crab Nebula could be detected at a level of ~ 41 sigma in less than 2 hours in the days affected by the mirror degradation using tailored MC data.

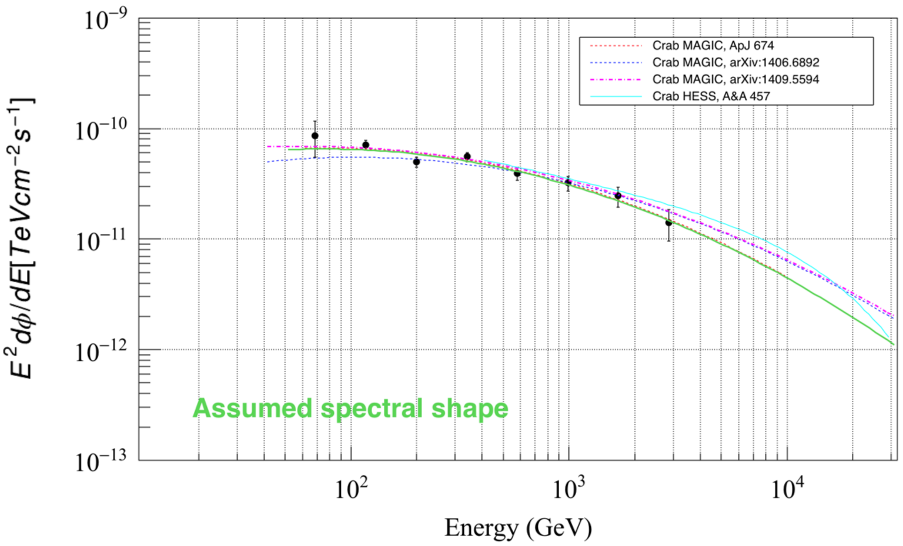

Figure 58: Spectral energy distribution of Crab Nebula data used for testing the RF in the analysis of TXS0506 +056.

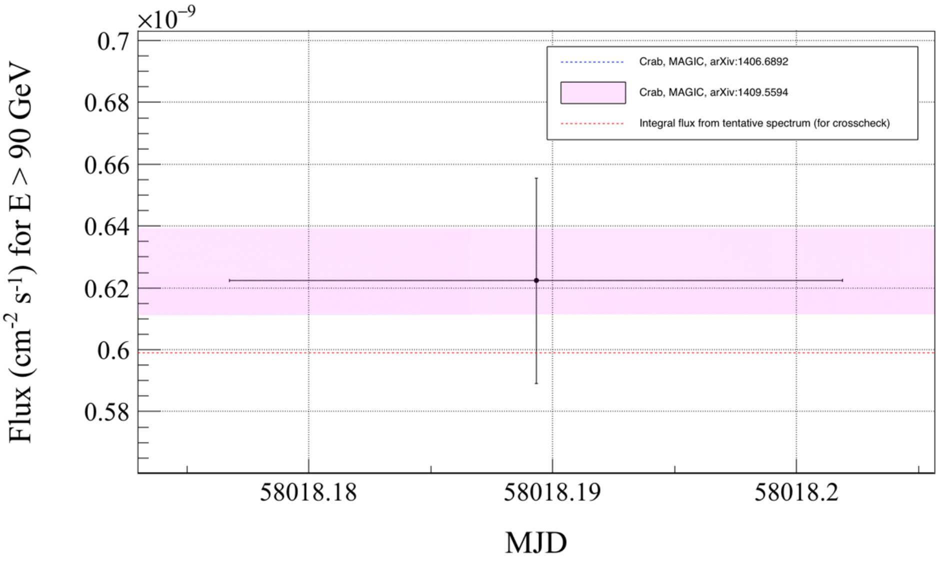

Figure 59: Single-bin light curve of the Crab Nebula during the period of the analysis of TXS0506 +056.

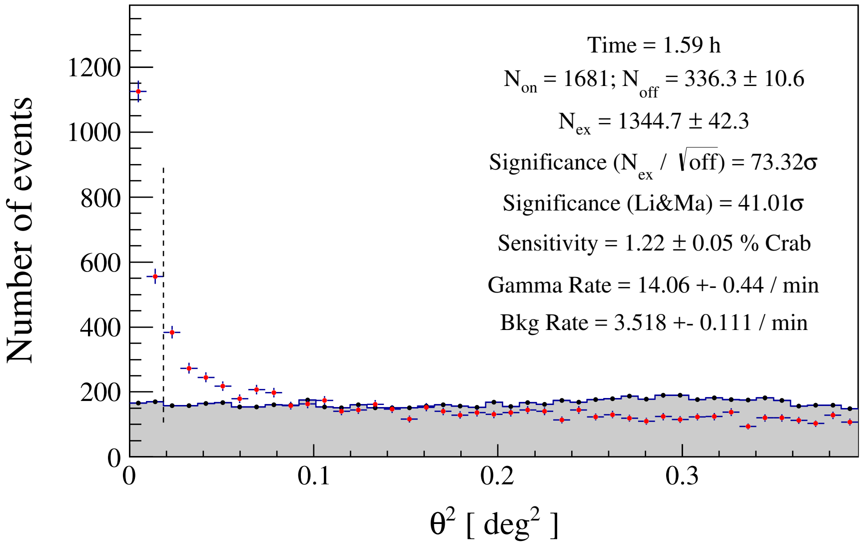

Figure 60: Detection significance at low energy (LE) of the test data from the Crab Nebula used for the production of the RF of TXS0506 +056.

4.2.1 Energy thresholds

In order to estimate the energy thresholds available for this analysis, I applied standard cuts for significance detection to the test MC data. This data is the same used to estimate the effective collection area, for which the higher level scientific results are obtained (2.2.4).

For standard analyses the following three high-level sets of cuts are defined:

- Low Energy : Hadronness < 0.28 and stereo SIZE > 60,
- Medium Range : Hadronness < 0.16 and stereo SIZE > 300,
- High Energy : Hadronness < 0.1 and stereo SIZE > 1000.

During the pre-trial phase the spectral index assumed for the source has been -3.0; I implemented this through a spectral weighting applied to the MC data, since in there the spectral index is fixed originally at -1.6.

This procedure resulted in the number distributions of MC events shown in figures 61, 62 and 63 as a function of energy. The energy thresholds correspond to the peak of each distribution for the three aforementioned sets of high-level cuts respectively.

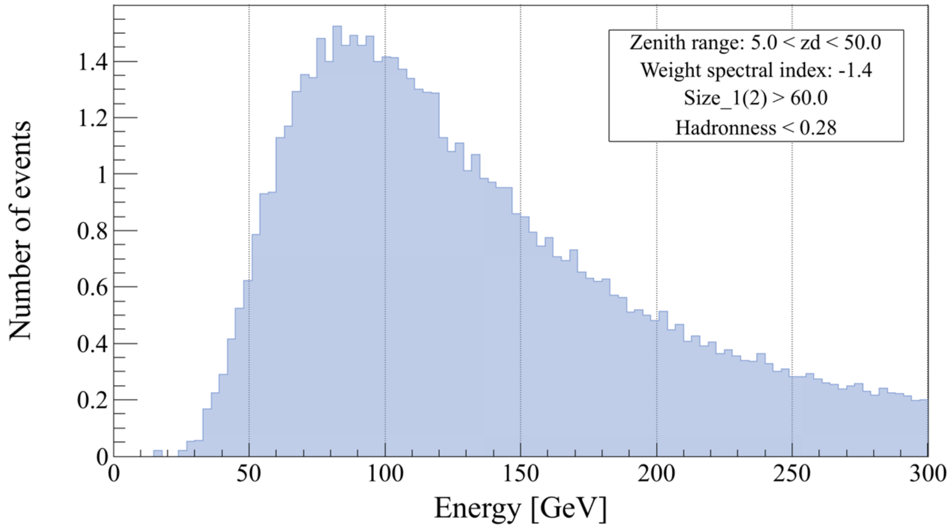

Figure 61: Normalized number distribution of simulated MC events as a function of energy for *Low energy range* cuts. Energy threshold is ~80 GeV.

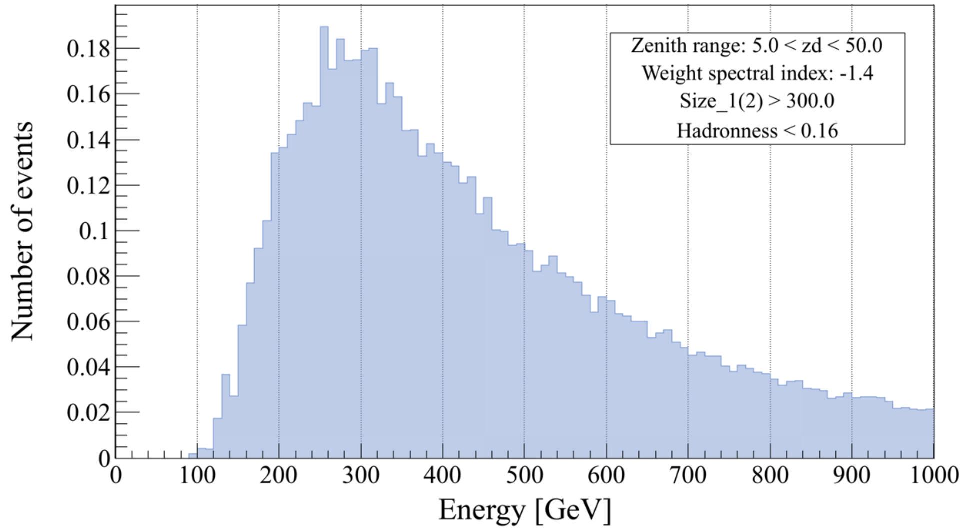

Figure 62: Normalized number distribution of simulated MC events as a function of energy for *Medium energy range* cuts. Energy threshold is ~250 GeV.

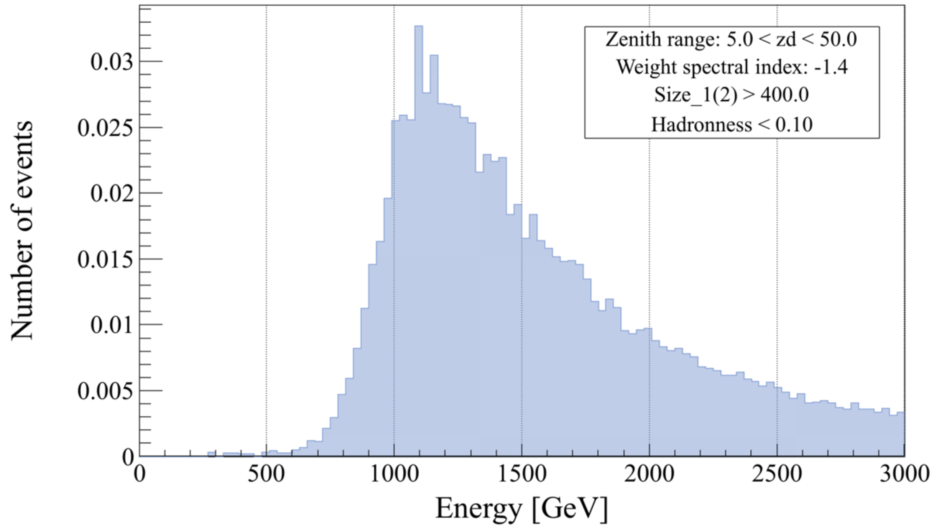

Figure 63: Normalized number distribution of simulated MC events as a function of energy for *High energy range* cuts. Energy threshold is ∼1.1 TeV.

For these estimations I kept the zenith range larger, in order to account for the full range provided by the simulations. The final nominal threshold has been chosen at $\sim$ 90 GeV between the two internal analyses.

4.3 ANALYSIS OF THE SIGNAL

In the following, I show the final detection significances estimated with the method by Li&Ma [73]. A day-wise summary is reported in table 3; in particular I selected data during non-optimal weather conditions as explained in section 2.1.2, whereas I did not cut data in good weather conditions - T>70% (i.e., all that data has been used).

Table 3: Summary of data from TXS0506 + 056; data quality tags are yellow for non-optimal weather conditions and green for good weather conditions

Day	Eff. time h	Zenith deg	M1 DC μA	LE significance Li&Ma σ	Data quality
24/09/2017	1.15	25 - 50	0.8 - 1.4	-1.30	🟨
28/09/2017	1.27	23 - 31	0.9 - 1.0	2.77	🟩
29/09/2017	2.91	21 - 50	0.9 - 1.0	0.85	🟩
30/09/2017	3.03	22 - 50	0.9 - 1.0	0.77	🟩
01/10/2017	2.87	21 - 47	0.9 - 1.0	3.58	🟩
02/10/2017	0.81	23 - 25	0.9 - 1.0	2.18	🟩
03/10/2017	1.30	22 - 26	0.8 - 1.2	2.97	🟩
04/10/2017	0.65	22 - 26	0.9 - 2.6	5.32	🟩

In Fig.66 and Fig.67 I show the distributions of the angular distances θ^2 between the reconstructed and nominal position of the source (i.e., the detection significance) for the entire ATEL period ([72]) and the final flare respectively. To estimate the background in the FoV, I chose 3 regions around an annulus centred at 0.4° from the source position (see 2.2.4), and I applied a normalisation between 0.2° and 0.25° over each region. The dashed vertical line in the plots indicates the optimal θ^2 cuts resulting from the automatic significance optimisation [37]:

- 0.0760 $\deg^2$ for the Atel period,
- 0.0182 $\deg^2$ for the flare on the last two days.

Figures 64 and 65 show the test statistics (TS) map and its distribution respectively. The source is clearly detected with the significance given by Fig.66 when integrating over the whole ATEL period.

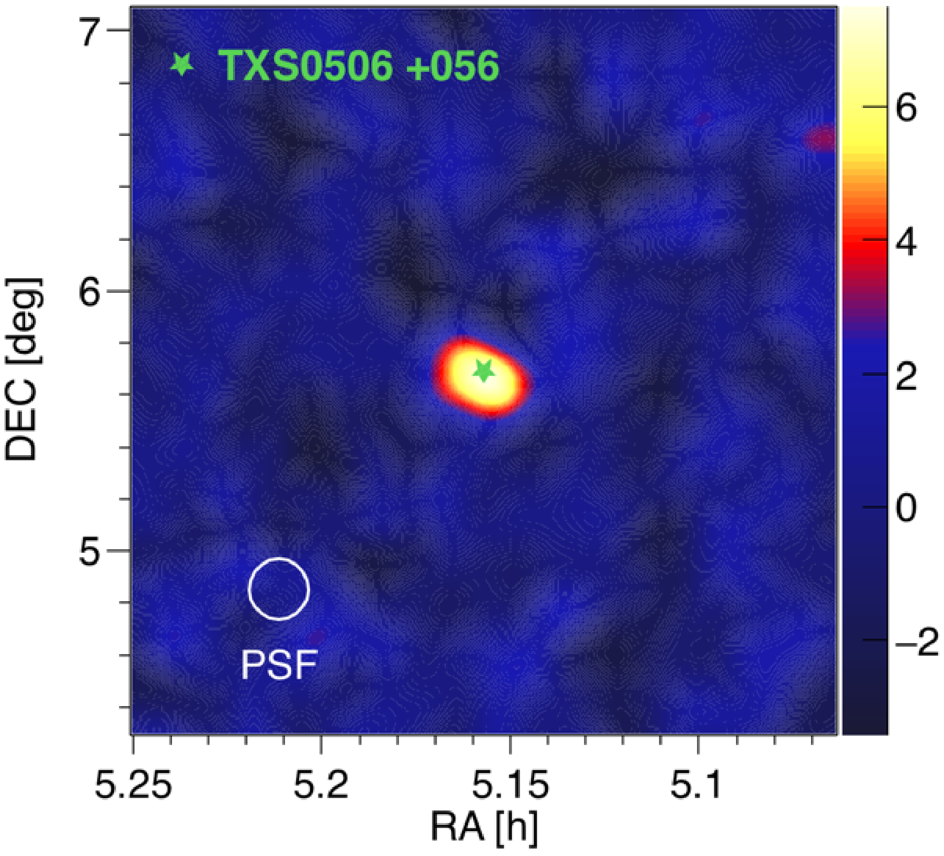

Figure 64: TS map correspondent to the ATEL period, from September 28th to October 4th.

The effective time (2.2.4) which takes into account the entire set of analysis cuts and the calculation of the lost dead time is approximately 13 hours.

I optimised the cuts for a low energy analysis:

- hadronness < 0.28,

- $\theta^2 < 0.02\,\text{deg}^2$,
- SIZE > 60 phe.

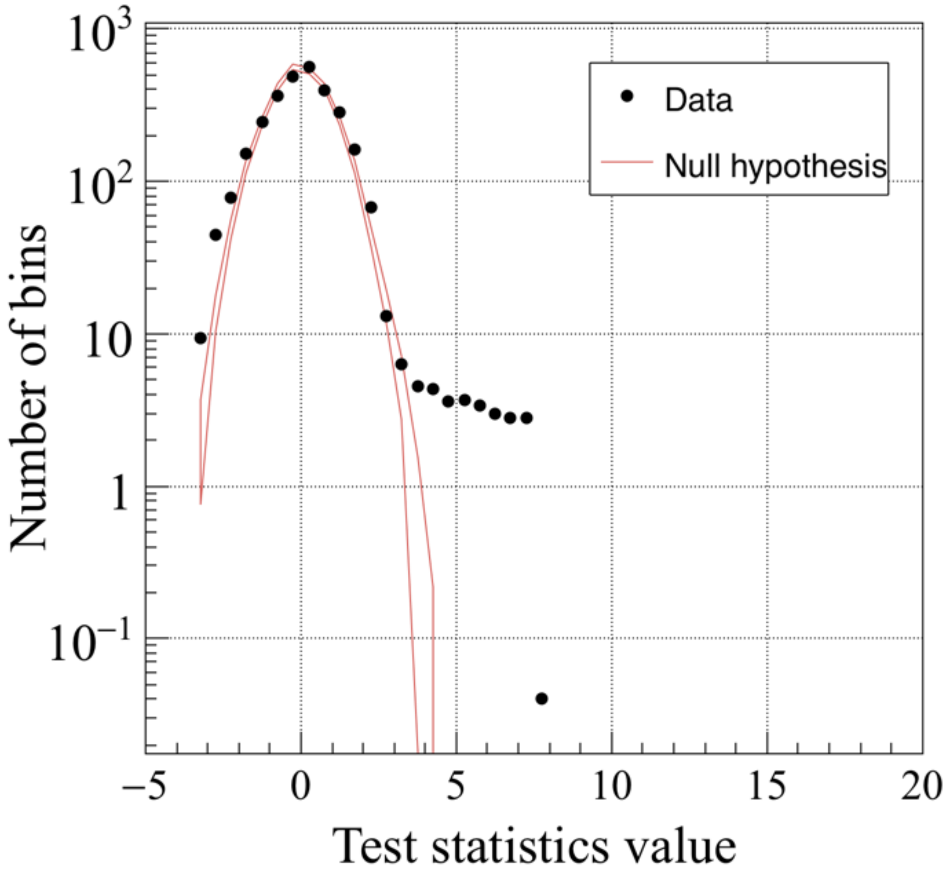

Figure 65: Histogram showing the comparison between the null hypothesis correspondent to no detection with the test statistics used by MAGIC.

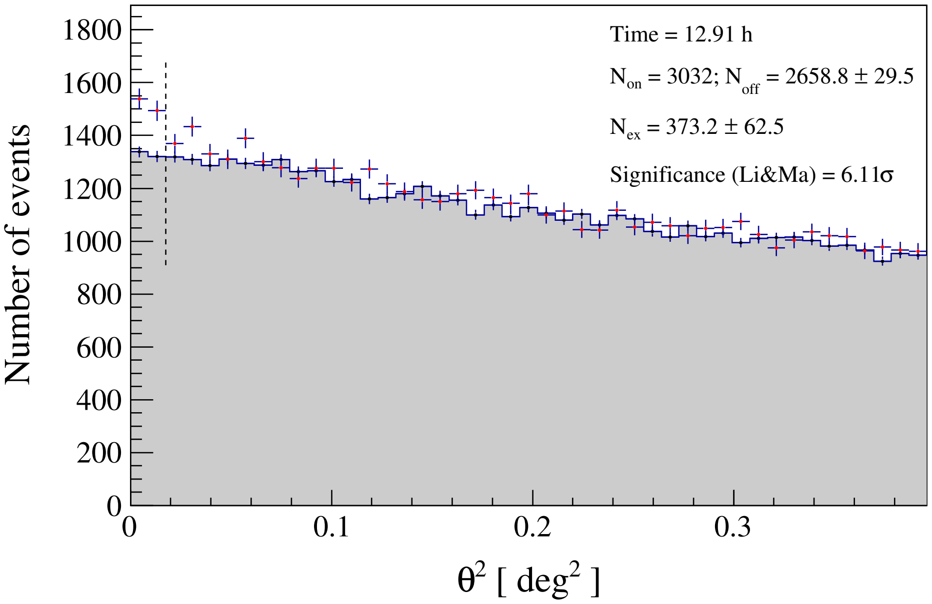

Figure 66: Detection significance correspondent to the ATEL period between September 28th and October 4th.

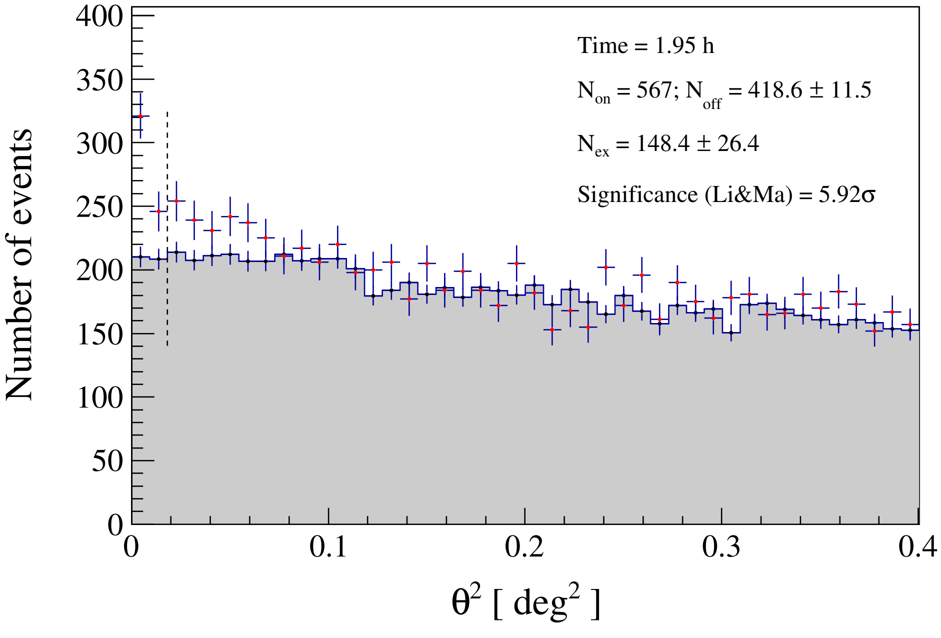

Figure 67: Detection significance correspondent to the to the flare detected between October 3rd and 4th.

4.4 LIGHT CURVES

In the following section I show the official light curves associated to this analysis. I produced each of them from a lower limit of 90 GeV, which has been chosen to be the common threshold energy between the two internal crosscheck analyses.

Fig.68 shows the time evolution of the energy flux above 90 GeV during the ATEL period. It comprises also the first day of observation in which the MAGIC telescopes followed-up the IceCube alert, but which wasn't included in the ATEL communication. The first flaring event appears to start already on October 2nd (~10 days after the neutrino alert) and lasts for the subsequent 2 days.

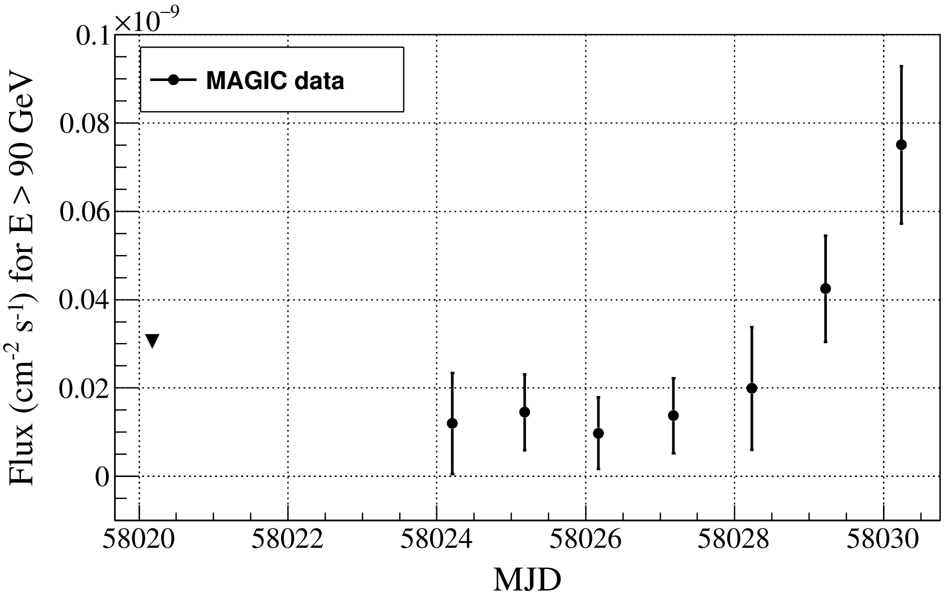

Figure 68: Light curve for ATEL period taking into account also the first day of observations. The upper limit on the first day is reported with 95% CL (2.2.4).

The mean flux in a single-bin configuration is $1.98e^{-11} \pm 3.99e^{-12}\mathrm{cm}^{-2}\mathrm{s}^{-1}$ with a fit probability of 1.35% using a constant flux prior. The fit result is shown in Fig.69.

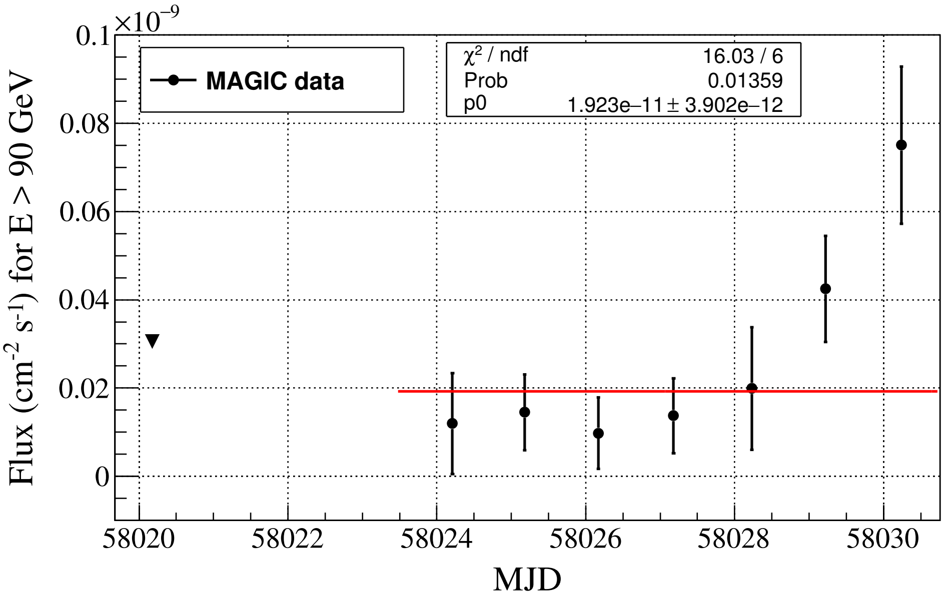

Figure 69: Check of the assumption for constant flux in TXS0506+056 data during the ATEL period.

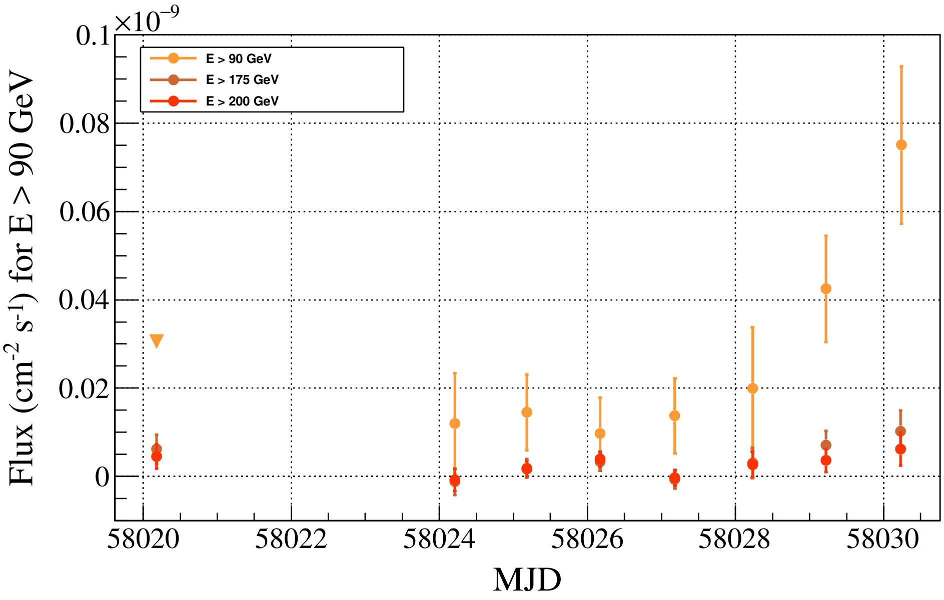

Figure 70: Comparison between the light curves of TXS0506+056 during the ATEL period. All upper limits ofr the first day are shown with 95% CL (2.2.4).

During the multi-collaboration effort, it was decided to provide further tests in order to account for the different thresholds implemented by the other IACT facilities [27] and check the compatibility of the results. Figure 70 shows the entire light curve using also higher-energy thresholds.

4.5 UNFOLDED SEDS

I report here the official final spectral energy distributions for TXS0506 +056 in the period defined by the MAGIC released ATEL [72]. Fig.71 shows the spectrum of TXS0506 +056, measured with data from the ATEL period, unfolded by means of the Tikhonov method [53].

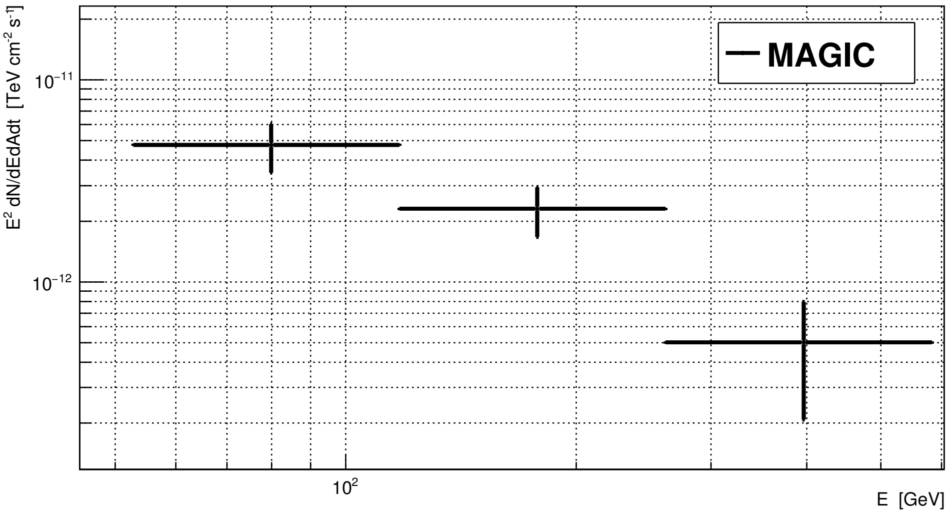

Figure 71: Spectral energy distribution of TXS0506 +056 in the period from September 24th to October 4th

Fig.72 shows the stability comparison between all the unfolding methods I applied to the spectral energy distribution (all such methods are the official ones used by the MAGIC collaboration - see 2.2.4 for more details).

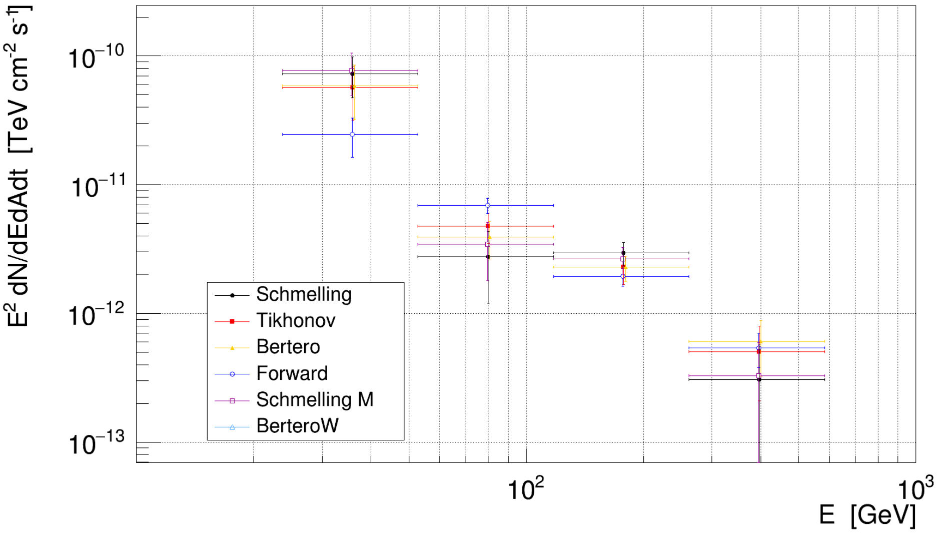

Figure 72: Comparison between all unfolding methods used to retrieve the spectral energy distribution of TXS 0506 +056 for the ATEL Period.

At the time of this analysis the redshift of the source was still unknown. This is a strong limitation for future studies which aim to model the physical processes responsible for the multi-frequency emission at the source - in particular the neutrino production - through spectral energy distributions. This was a sufficient motivation for estimating a possible redshift.

Given the prior spectral index assumed during the phase of flux estimation (Fig.73), it was decided to apply the forward folding method (2.2.4) along with different test redshift values. In each case the absorption caused by the Extragalactic Background Light (EBL) [74] was considered, in particular within the model given by [75]. This test allows to approximately spot unlikely values for the redshift when looking for unexpected features in the deabsoberd SED, such as flux pile-ups at higher energies (a more statistically precise method is described in [76]).

The test redshift values were chose to span a reasonable range on the basis of the source's nature and the VHE observational evidence. In particular, the γ-ray horizon correspondent to 100 GeV photons is estimated to be ~1 and indeed the most far object of this kind detected by the MAGIC telescopes at VHE reached a record redshift of ~ 0.9 [77].

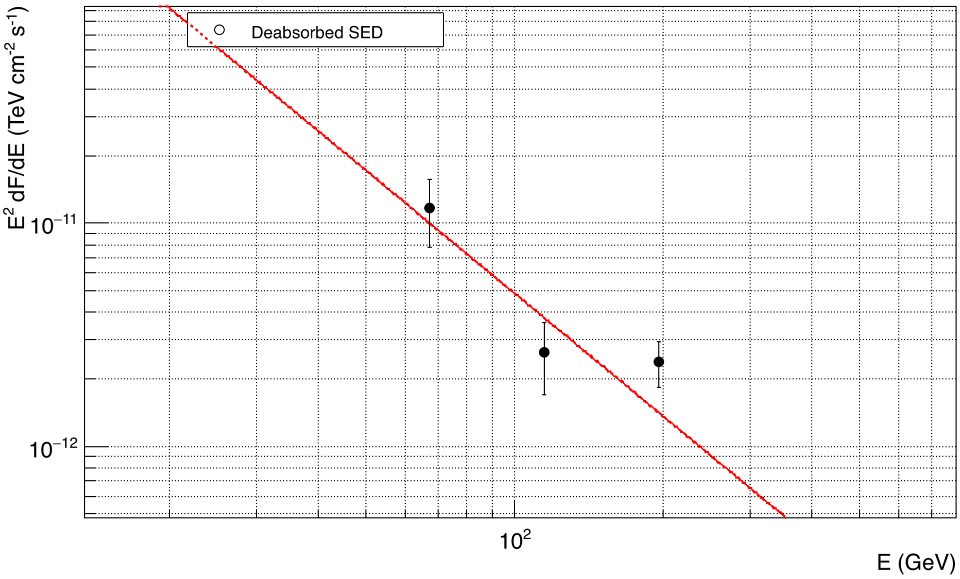

Figure 73: Forward folded spectral energy distribution of TXS 0506+056 during the ATEL period using no redshift.

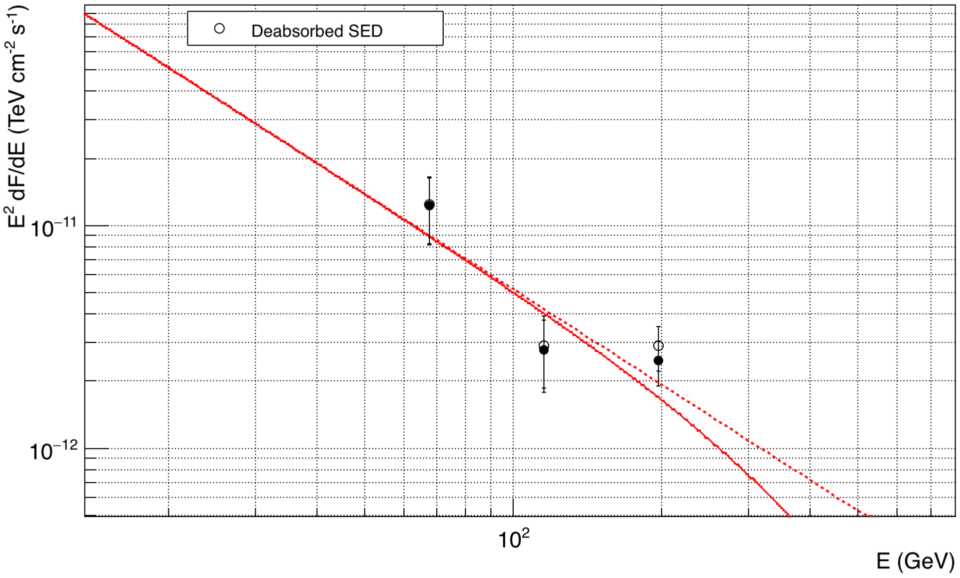

Figure 74: Forward folded spectral energy distribution of TXS 0506+056 during the ATEL period simulating a redshift of z = 0.15.

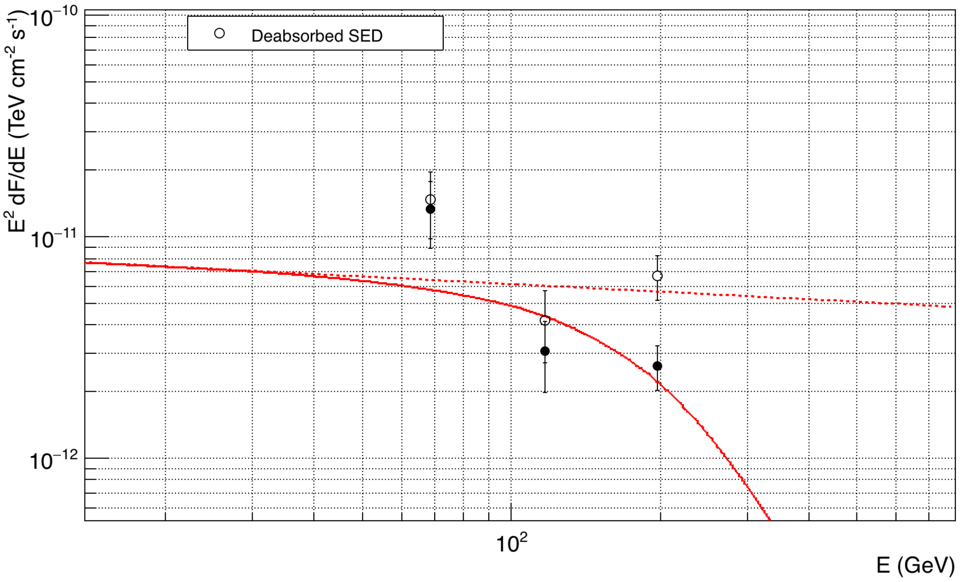

Figure 75: Forward folded spectral energy distribution of TXS 0506+056 during the ATEL period simulating a redshift of z = 0.52.

By the end of February 2018 the redshift of the source has been independently measured by means of optical spectroscopy, yielding a value of $z = 0.3365 \pm 0.0010$ [78]. It can be noted that such value is mid-way between the two used in this analysis: a comparison between this measure and figures 74 and 75 shows that the incompatibility given by the second value of 0.52 was rather justified a-posteriori as a too high assumed redshift.

5 CONCLUSIONS

This thesis described novel work in the analysis of VHE data with the MAGIC telescopes. In particular it focused on two new major developments to which I have participated during my PhD.

The first, currently under development, is concerned with the observation of sources at the lowest elevations ever reached by an IACT experiment. The aim of such observations is to probe γ-ray signals at energies $\geqslant$ 100 TeV, coming from Galactic sources. This will prove fundamental in probing, in a more stringent way, scenarios of the origin of Galactic cosmic rays, which in the last few years has seen supernova remnants as the most likely source. This work shows that Very Large Zenith Angle observations allow one to access energies up to about 100 TeV with collection areas of the order of at least 1 km^2 and current research is ongoing. In particular I have shown how, since its start, this technique required a quite different approach with respect to previous observations made by MAGIC.

The entire standard data analysis pipeline required modifications in its application, and currently new ideas - modern techniques of machine learning, additional instruments for atmospheric monitoring, improved dedicated MC simulations - are starting to grow. This thesis showed specifically how the standard analysis has been tackled, in order to prove its limitations at VLZAs and probe in which directions and how much it can be boosted to account for the stringent requirements given by VLZA observations.

The second original contribution described in this work concerns observations of the first VHE extragalactic source from which also a HE neutrino has been detected as spatially coincident. Such event triggered the onset of one of the biggest multi-wavelength - and, more importantly, multi-messenger - observation campaigns since the detection of gravitational waves and their connection with neutron star mergers. The extragalactic source responsible for the VHE and HE neutrino emission has been confirmed to be TXS 0506 +056, belonging to the BL Lac class of blazars, a type of AGN. From this source the IceCube collaboration measured a neutrino energy of almost 300 TeV, whereas the MAGIC telescopes detected the blazar up to few hundreds of GeV. The combined results of the first ever detection of γ-ray emission from the blazar TXS 0506 +056 and the spatially coincident neutrino detection at HE from the IceCube observatory corroborates the hypothesis that AGNs and in particular *blazars* can also be sources of high energy neutrinos - at least in active phases of their evolution.

An interpretation such as this is even more profound if taking into account the unified model of AGNs. Being TXS0506 +056 an object belonging to the BL Lac class, its VHE emission is relativistically boosted in the direction of the observer. A high energy neutrino event from this class in particular, ties up nicely with an AGN unified framework scenario, which can be an additional point supporting the idea that also other classes of AGNs could contribute to the overall extragalactic component of cosmic rays and HE neutrino diffuse background.

The subjects described in this thesis are of high interest to CTA, the next generation instrument.

An interesting comparison can be done over some of the characteristics of the future CTA-North site, currently under construction at La Palma. In the same energy range described by the data analysis shown in chapter 3, the new observatory should reach a collection area of about 1 km^2, whereas with the current technique of VLZA by the MAGIC telescopes we can already reach more then that. This result can be appreciated by comparing Fig.76 with Fig.46.

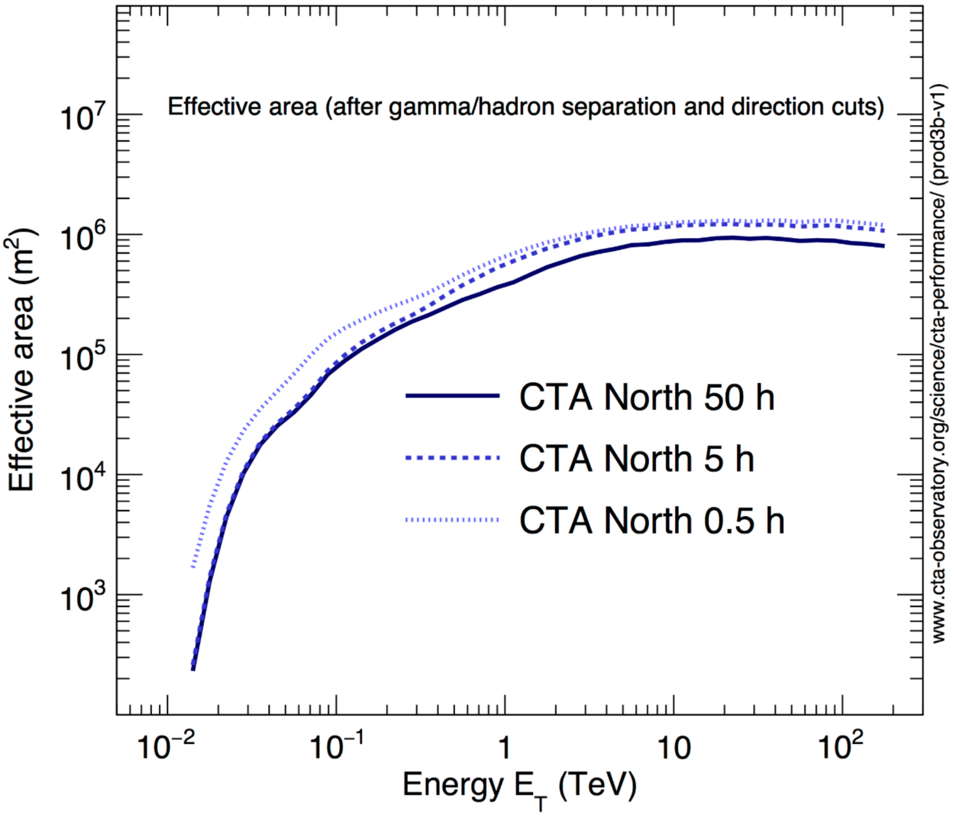

Figure 76: Effective collection area as a function of true energy for CTA-North for different amounts of integrating hours. Credits: CTA observatory.

The application of VLZA observations in the case of a telescope array could prove challenging from the point of view of how to manage multiple telescopes at such low elevations.

As mentioned in 3.3.1, the dependence of the gamma detection efficiency is not trivial at such high values of zenith. With a configuration involving multiple instruments relatively near to one another it will be necessary to invoke specific studies on how the array behaves at VLZA both in structural terms and from the point of view of performance.

Upcoming applications with few Large Size Telescopes (LSTs) telescopes could involve their use together with the MAGIC telescopes (the LSTs are being built at the MAGIC site). In that case CTA + VLZA observations could be implemented already, delivering observations of series of astrophysical sources beyond 100 TeV energy.

BIBLIOGRAPHY

1. Rossi, B. *Cosmic rays* (McGraw-Hill, 1964) (cit. on p. 16).
2. Hess, V. Über Beobachtungen der durchdringenden Strahlung bei sieben Freiballonfahrten. *Physikalische Zeitschrift* **13,** 1084–1091 (1912) (cit. on p. 16).
3. Pacini, D. La radiazione penetrante alla superficie ed in seno alle acque. *Il Nuovo Cimento* **3,** 93–100 (1912) (cit. on p. 16).
4. Blasi, P. The origin of galactic cosmic rays. *The Astronomy and Astrophysics Review* **21,** 70. ISSN: 0935-4956 (Nov. 2013) (cit. on pp. 17, 18).
5. Potgieter, M. S. Solar modulation of cosmic rays. *Living Reviews in Solar Physics* **10.** ISSN: 16144961. doi:`10.12942/lrsp-2013-3`. arXiv: `1306.4421 [physics.space-ph]` (2013) (cit. on pp. 18, 19).
6. Tibolla, O. & Drury, L. Prolegomena. *Nuclear Physics B - Proceedings Supplements* **256-257,** 1–8. ISSN: 09205632 (Nov. 2014) (cit. on p. 18).
7. Weinstein, A. Pulsar Wind Nebulae and Cosmic Rays: A Bedtime Story. *Nuclear Physics B - Proceedings Supplements* **256-257,** 136–148. ISSN: 09205632 (Nov. 2014) (cit. on p. 18).
8. The HESS collaboration. Acceleration of petaelectronvolt protons in the Galactic Centre. *Nature* **531,** 476–479. ISSN: 0028-0836 (Mar. 2016) (cit. on p. 18).
9. Kafexhiu, E., Aharonian, F., Taylor, A. M. & Vila, G. S. Parametrization of gamma-ray production cross sections for <math display="inline"> <mi>p</mi> <mi>p</mi> </math> interactions in a broad proton energy range from the kinematic threshold to PeV energies. *Physical Review D* **90,** 123014. ISSN: 1550-7998 (Dec. 2014) (cit. on p. 18).
10. Ahnen, M. L. *et al.* A cut-off in the TeV gamma-ray spectrum of the SNR Cassiopeia A. *Monthly Notices of the Royal Astronomical Society* **472,** 2956–2962. ISSN: 0035-8711 (Dec. 2017) (cit. on p. 19).
11. Letessier-Selvon, A. & Stanev, T. Ultrahigh energy cosmic rays. *Reviews of Modern Physics* **83,** 907–942. ISSN: 00346861 (2011) (cit. on pp. 19, 21).
12. Gaisser, T. K. *Cosmic rays and particles* ISBN: 0521339316 (Cambridge University Press, 1990) (cit. on pp. 19, 21, 33).
13. Aab, A. *et al.* The Pierre Auger Cosmic Ray Observatory. *Nuclear Instruments and Methods in Physics Research, Section A: Accelerators, Spectrometers, Detectors and Associated Equipment* **798,** 172–213. ISSN: 01689002 (2015) (cit. on pp. 19, 21).
14. The Pierre Auger Collaboration *et al.* Indication of anisotropy in arrival directions of ultra-high-energy cosmic rays through comparison to the flux pattern of extragalactic gamma-ray sources. **29.** ISSN: 2041-8213. doi:`10.3847/2041-8213/aaa66d`. arXiv: `1801.06160`. `http://arxiv.org/abs/1801.06160` (2018) (cit. on p. 19).

15. Kotera, K. & Olinto, A. V. The Astrophysics of Ultrahigh Energy Cosmic Rays. ISSN: 0066-4146. doi:`10.1146/annurev-astro-081710-102620`. arXiv: `1101.4256`. `http://arxiv.org/abs/1101.4256%7B%5C%%7D0Ahttp://dx.doi.org/10.1146/annurev-astro-081710-102620` (2011) (cit. on pp. 19, 20).

16. Albert, J. *et al.* Very-High-Energy Gamma Rays from a Distant Quasar: How Transparent Is the Universe? *Science* **320,** 1752–1754. ISSN: 0036-8075 (June 2008) (cit. on p. 19).

17. collaboration, I. Evidence for High-Energy Extraterrestrial Neutrinos at the IceCube Detector. *Science* **342.** ISSN: 0036-8075. doi:`10.1126/science.1242856`. `http://www.sciencemag.org/cgi/doi/10.1126/science.1242856` (Nov. 2013) (cit. on p. 19).

18. Abbott, B. P. *et al.* Observation of Gravitational Waves from a Binary Black Hole Merger. *Physical Review Letters* **116,** 061102. ISSN: 0031-9007 (Feb. 2016) (cit. on p. 20).

19. Abbott, B. P. *et al.* Multi-messenger Observations of a Binary Neutron Star Merger. *The Astrophysical Journal Letters* **848,** L12. ISSN: 2041-8205 (2017) (cit. on p. 20).

20. Abbott, B. P. *et al.* GW170817: Observation of Gravitational Waves from a Binary Neutron Star Inspiral. *Physical Review Letters* **119,** 30–33. ISSN: 10797114 (2017) (cit. on p. 20).

21. Caprini, C. & Figueroa, D. G. Cosmological Backgrounds of Gravitational Waves. arXiv: `1801.04268`. `http://arxiv.org/abs/1801.04268` (Jan. 2018) (cit. on p. 20).

22. Peterson, B. M. *An Introduction to Active Galactic Nuclei* (Cambridge, New York Cambridge University Press, 1997) (cit. on p. 20).

23. Boldt, E. & Ghosh, P. Cosmic rays from remnants of quasars? *Monthly Notices of the Royal Astronomical Society* **307,** 491–494. ISSN: 00358711 (1999) (cit. on p. 20).

24. IceCube Collaboration *et al.* Observation and Characterization of a Cosmic Muon Neutrino Flux from the Northern Hemisphere using six years of IceCube data. **3.** ISSN: 1538-4357. doi:`10.3847/0004-637X/833/1/3`. arXiv: `1607.08006`. `http://arxiv.org/abs/1607.08006%7B%5C%%7D0Ahttp://dx.doi.org/10.3847/0004-637X/833/1/3` (2016) (cit. on p. 20).

25. Loeb, A. & Waxman, E. The cumulative background of high energy neutrinos from starburst galaxies. *Journal of Cosmology and Astroparticle Physics* **2006,** 003–003. ISSN: 1475-7516 (May 2006) (cit. on p. 20).

26. Fox, D. B. & Kashiyama, K. SUB-PeV NEUTRINOS FROM TeV UNIDENTIFIED SOURCES IN THE GALAXY. **74,** 4–9 (2013) (cit. on p. 20).

27. IceCube *et al.* Multiwavelength observations of a flaring blazar coincident with an IceCube high-energy neutrino. *Accepted on Science* (2018) (cit. on pp. 20, 83, 84, 100).

28. Klebesadel, R. W., Strong, I. B. & Olson, R. A. Observations of Gamma-Ray Bursts of Cosmic Origin. *The Astrophysical Journal* **182,** L85. ISSN: 0004-637X (1973) (cit. on p. 21).

29. Atwood, F. C. W. B. The Large Area Telescope on the Fermi Gamma-ray Space Telescope Mission. *The Astrophysical Journal* **697,** 1071–1102 (2009) (cit. on pp. 21, 84).

30. Weekes, T. C. *et al.* Observation of TeV gamma rays from the Crab nebula using the atmospheric Cerenkov imaging technique. *The Astrophysical Journal* **342,** 379. ISSN: 0004-637X (1989) (cit. on p. 21).

31. Rossi, B. & Greisen, K. Cosmic-Ray Theory. *Reviews of Modern Physics* **13,** 240–309. ISSN: 0034-6861 (Oct. 1941) (cit. on p. 21).

32. Abeysekara, A. U. *et al.* Sensitivity of the high altitude water Cherenkov detector to sources of multi-TeV gamma rays. *Astroparticle Physics* **50-52,** 26–32. ISSN: 09276505 (2013) (cit. on p. 21).

33. Hinton, J. & Hofmann, W. Teraelectronvolt Astronomy. *Annual Review of Astronomy and Astrophysics* **47,** 523–565. ISSN: 0066-4146 (2009) (cit. on pp. 22–24).

34. Heitler, W. *The Quantum Theory of Radiation* 3rd (1954) (cit. on p. 22).

35. Bethe, H. & Heitler, W. *On the Stopping of Fast Particles and on the Creation of Positive Electrons* 1934. doi:`10.1098/rspa.1934.0140` (cit. on p. 22).

36. Hillas, A. M. *Cherenkov Light Images of EAS produced by Primary Gamma Rays and By Buclui* in *19th International Cosmic Ray Conference* **3** (La Jolla, Aug. 1985), 445 (cit. on pp. 24, 27).

37. Aleksić, J. *et al.* The major upgrade of the MAGIC telescopes, Part II: A performance study using observations of the Crab Nebula. *Astroparticle Physics* **72,** 76–94. ISSN: 09276505 (2015) (cit. on pp. 28, 31, 36, 39, 56, 76–78, 87, 96).

38. Acero, F. *et al.* Cherenkov Telescope Array Contributions to the 35th International Cosmic Ray Conference (ICRC2017). arXiv: `1709.03483`. `http://arxiv.org/abs/1709.03483` (Sept. 2017) (cit. on pp. 29, 82).

39. Konopelko, A. *et al.* Effectiveness of TeV γ-ray observations at large zenith angles with a stereoscopic system of imaging atmospheric Čerenkov telescopes. *Journal of Physics G: Nuclear and Particle Physics* **25,** 1989–2000. ISSN: 09543899 (1999) (cit. on p. 30).

40. The HESS Collaboration. *H.E.S.S. specifications* doi:`https://www.mpi-hd.mpg.de/hfm/HESS/pages/about/telescopes/` (cit. on p. 31).

41. VERITAS Collaboration. *VERITAS Specifications* 2018. `https://veritas.sao.arizona.edu/about-veritas-mainmenu-81/veritas-specifications-mainmenu-111` (cit. on p. 31).

42. Aleksić, J. *et al.* The major upgrade of the MAGIC telescopes, Part I: The hardware improvements and the commissioning of the system. *Astroparticle Physics* **72,** 61–75. ISSN: 09276505 (2016) (cit. on pp. 31, 44, 45).

43. Doro, M. *et al.* The reflective surface of the MAGIC telescope. *Nuclear Instruments and Methods in Physics Research, Section A: Accelerators, Spectrometers, Detectors and Associated Equipment* **595,** 200–203. ISSN: 01689002 (2008) (cit. on p. 32).

44. Dazzi, F. *A new stereoscopic 'Sum-Trigger-II' for the MAGIC Telescopes* PhD thesis (Università degli Studi di Udine, 2012) (cit. on p. 32).

45. Aleksić, J. *et al.* Measurement of the Crab Nebula spectrum over three decades in energy with the MAGIC telescopes. *Journal of High Energy Astrophysics* **5-6,** 30–38. ISSN: 22144048 (Mar. 2015) (cit. on p. 32).

46. Pareschi, G. *et al. Glass mirrors by cold slumping to cover 100 m 2 of the MAGIC II Cherenkov telescope reflecting surface* in (eds Atad-Ettedgui, E. & Lemke, D.) (July 2008), 70180W. doi:`10.1117/12.790404`. `http://proceedings.spiedigitallibrary.org/proceeding.aspx?doi=10.1117/12.790404` (cit. on p. 32).

47. Colin, P. *et al.* Probing the CR positron/electron ratio at few hundreds GeV through Moon shadow observation with the MAGIC telescopes. **6,** 194–197 (2011) (cit. on p. 32).

48. Fruck, C. & Gaug, M. Atmospheric monitoring in MAGIC and data corrections. *EPJ Web of Conferences* **89,** 02003. ISSN: 2100-014X (2015) (cit. on pp. 33, 34).

49. Fruck, C. *et al. A novel LIDAR-based Atmospheric Calibration Method for Improving the Data Analysis of MAGIC* in *33RD INTERNATIONAL COSMIC RAY CONFERENCE* (2013) (cit. on p. 34).

50. Albert, J. *et al.* Implementation of the Random Forest method for the Imaging Atmospheric Cherenkov Telescope MAGIC. *Nuclear Instruments and Methods in Physics Research, Section A: Accelerators, Spectrometers, Detectors and Associated Equipment* **588,** 424–432. ISSN: 01689002 (2008) (cit. on p. 38).

51. Fomin, V. P. *et al.* New methods of atmospheric Cherenkov imaging for gamma-ray astronomy. I. The False Source method. *Astroparticle Physics* **2,** 137–150 (1994) (cit. on p. 41).

52. Rolke, W. a., López, A. M. & Conrad, J. Limits and confidence intervals in the presence of nuisance parameters. *Nuclear Instruments and Methods in Physics Research Section A: Accelerators, Spectrometers, Detectors and Associated Equipment* **551,** 493–503. ISSN: 01689002 (2005) (cit. on p. 43).

53. Tikhonov, A. N. & Arsenin, V. I. Solutions of ill-posed problems (1977) (cit. on pp. 43, 101).

54. Bertero, M. Linear inverse and ill-posed problems. *Advances in Electronics and Electron Physics* **75** (ed Hawkes, P.) 1–120 (1989) (cit. on p. 43).

55. Schmelling, M. The method of reduced cross-entropy A general approach to unfold probability distributions. *Nuclear Inst. and Methods in Physics Research, A* **340,** 400–412. ISSN: 01689002 (1994) (cit. on p. 43).

56. Betorz, J. *Search for Correlations of Atmospheric Transmission obtained from the MAGIC LIDAR and the Pyrometer and Characterization of ASICs for the CTA* PhD thesis (Universitat Auto'noma de Barcelona, 2015) (cit. on p. 48).

57. Fuchs, M. *Untersuchung der atmosphärischen Transmission mittels Pyroskop und Lidar zur Gamma-Astronomie mit dem MAGIC Cherenkov Teleskop auf La Palma* PhD thesis (Werner-Heisenberg Institut f\ddot{u}r Physik, 2008) (cit. on p. 48).

58. Ahnen, M. *et al.* Performance of the MAGIC telescopes under moonlight. *Astroparticle Physics* **94,** 29–41. ISSN: 09276505 (Sept. 2017) (cit. on pp. 54, 57).

59. Kolmogorov, A. *Grundbegriffe der Wahrscheinlichkeitsrechnung* (1933) (cit. on p. 69).

60. NASA. *The GCN/TAN system* (cit. on p. 83).

61. Carosi, A. *et al. Recent follow-up observations of GRBs in the very high energy band with the MAGIC telescopes* in *The 34th International Cosmic Ray Conference* (The Hague, 2015) (cit. on p. 83).

62. Smith, M. W. *et al.* The Astrophysical Multimessenger Observatory Network (AMON). *Astroparticle Physics* **45,** 56–70. ISSN: 09276505 (2013) (cit. on p. 83).

63. *GCN/AMON NOTICE ICECUBE EHE 170922* `https://gcn.gsfc.nasa.gov/notices%7B%5C_%7Damon/50579430%7B%5C_%7D130033.amon` (cit. on p. 83).

64. Blaufuss, E. & Kopper, C. *IceCube-170922A* 2017 (cit. on p. 83).

65. Aartsen, M. G. *et al.* The IceCube Neutrino Observatory: Instrumentation and online systems. *Journal of Instrumentation* **12.** ISSN: 17480221. doi:`10.1088/1748-0221/12/03/P03012`. arXiv: `1612.05093` (2017) (cit. on p. 83).

66. Berti, A. *Study of astrophysical transients with the MAGIC telescopes* PhD thesis (Trieste, 2017) (cit. on p. 83).

67. Tanaka, Y. T., Buson, S. & Kocevski, D. *Fermi-LAT detection of increased gamma-ray activity of TXS 0506+056, located inside the IceCube-170922A error region* 2017 (cit. on p. 84).

68. Acero, F. *et al.* Fermi Large Area Telescope Third Catalog. *The Astrophysical Journal Supplement Series* **218,** 23. ISSN: 1538-4365 (2015) (cit. on p. 84).

69. Padovani, P. *et al.* Active Galactic Nuclei: what's in a name? ISSN: 0935-4956. doi:`10.1007/s00159-017-0102-9`. arXiv: `1707.07134`. `http://arxiv.org/abs/1707.07134%7B%5C%%7D0Ahttp://dx.doi.org/10.1007/s00159-017-0102-9` (2017) (cit. on p. 84).

70. collaboration, I. *Circular Service 21916* 2017 (cit. on p. 84).

71. Rutledge, R. E. The Astronomer's Telegram: A Web-based Short-Notice Publication System for the Professional Astronomical Community. *Publications of the Astronomical Society of the Pacific* **110,** 754–756. ISSN: 0004-6280 (June 1998) (cit. on p. 84).

72. Mirzoyan, R. & MAGIC. First-time detection of VHE gamma rays by MAGIC from a direction consistent with the recent EHE neutrino event IceCube-170922A. *The Astronomer's Telegram* (2017) (cit. on pp. 84, 96, 101).

73. Li, T.-P. & Ma, Y.-Q. Analysis methods for results in gamma-ray astronomy. *The Astrophysical Journal* **272,** 317. ISSN: 0004-637X (1983) (cit. on p. 95).

74. Gould, R. J. & Schréder, G. Opacity of the Universe to High-Energy Photons. *Physical Review Letters* **16,** 252–254. ISSN: 0031-9007 (Feb. 1966) (cit. on p. 102).
75. Domínguez, a. *et al.* Extragalactic background light inferred from AEGIS galaxy-SED-type fractions. *Monthly Notices of the Royal Astronomical Society* **410,** 2556–2578. ISSN: 00358711 (2011) (cit. on p. 102).
76. Prandini, E., Mariotti, M. & Tavecchio, F. *Constraining blazars distances with combined GeV and TeV data* in *Fermi Symposium proceedings* (2011) (cit. on p. 102).
77. Ahnen, M. L. *et al.* Detection of very high energy gamma-ray emission from the gravitationally lensed blazar QSO B0218+357 with the MAGIC telescopes. *Astronomy & Astrophysics* **595,** A98. ISSN: 0004-6361 (Nov. 2016) (cit. on p. 102).
78. Paiano, S., Falomo, R., Treves, A. & Scarpa, R. The Redshift of the BL Lac Object TXS 0506+056. *The Astrophysical Journal* **854,** L32. ISSN: 2041-8213 (Feb. 2018) (cit. on p. 103).